2015

Special Topics in Solid State Diffusion: I. Grain Boundary Variability II. Fluid in Deformable Solid

Mahyar Mohebi-Moghadam
Lehigh University

SPECIAL TOPICS IN

SOLID STATE DIFFUSION:

I. GRAIN BOUNDARY VARIABILITY

II. FLUID IN DEFORMABLE SOLID

By

MAHYAR MOHEBI-MOGHADAM

Presented to the Graduate and Research Committee of

Lehigh University

in Candidacy for the Degree of

Doctor of Philosophy

in

Materials Science & Engineering

Lehigh University

January 2015

Approved and recommended for acceptance as a dissertation in partial fulfillment of the requirements for the degree of Doctor of Philosophy.

_____

Date

_____

Dissertation Director

_____

Accepted Date

Committee Members:

_____

Name of Committee Chair

_____

Name of Committee Member

_____

Name of Committee Member

_____

Name of Committee Member

Acknowledgment:

Ostensibly, this dissertation represents the consummation of my PhD work. In reality, it represents thirty four years of patient and thoughtful support from family, friends and all my teachers and mentors. In this regard, I would like to acknowledge all who contributed to this journey for such a long time. In particular, I must express my profound appreciation to Professor Jeffrey M. Rickman who, in the last four years, emerged as a trusted guide and mentor for this work and all of which I endeavor to undertake in the future. He has been the best advisor I could have imagined not only because of his extended knowledge but also due to his great personality that makes him a role model in my future professional career. To members of my committee, Professor Martin P. Harmer, Professor Helen M. Chan and Professor Edmund Webb III, I have extended special appreciation for their dependable, serious and accurate guidance, input and support during the accomplishment of this work. I am also grateful for the administrative support provided by MSE staff, including Janie Carlin, Anne Marie Lobley, Lisa Arechiga and Katrina Kraft.

In the course of this work, my quest for information introduced me to Professor Gregory S. Rohrer from Carnegie Mellon University. I appreciate his generosity for letting us using his research data in our work. My sincere gratitude also goes to Professor Mohammad-Reza Aboutalebi and Professor S. Hossein Seyedein from Iran University of Science & Technology, for providing me the numerical solver for the finite difference code.

I would like to express my acknowledgment to Sherman Fairchild Center for Solid State Studies for their precious fellowship in 2013-2014 which induced a momentum to continue forward through my research. The computational resource for this project flowed generously from Minnesota Supercomputing Institute (MSI) and I would like to thank them for this invaluable assistance as well.

I specially appreciate American Chemical Society (ACS)-Petroleum Research Fund and Office of Naval Research (ONR) for financially sponsoring my researches and providing this wonderful opportunity to pursue my PhD.

Finally, I must express my deepest gratitude and warmest appreciation to my parents, Mehdi Mohebi-Moghadam and Jila Shapouri and to my sister, Mahsa Mohebi-Moghadam for tireless support and unconditional love offered in the forms that only a family can provide and to my lovely wife, Shokouh Pourarian for her endless enthusiasm, inspiration and love. She was the one who encouraged me for PhD study and paved the road for applying abroad. She has made huge sacrifices in this journey, particularly during this last couple months which I was staying focused on dissertation while she has been carrying our first baby. This dissertation is entirely dedicated to her.

Mahyar Mohebi-Moghadam,

December 2014

Lehigh University, Bethlehem, PA

Table of Contents

ABSTRACT

In the first part of this study, we investigate the impact of grain-boundary variability on mass transport behavior in a polycrystal. More specifically, we perform both numerical and analytical studies of steady-state diffusion in prototypical microstructures in which there is either a discrete spectrum of grain-boundary activation energies or else a complex distribution of grain-boundary character, and hence a continuous spectrum of boundary activation energies. An effective diffusivity is calculated for these structures using simplified multi-state models and, in some cases, employing experimentally obtained grain-boundary energy data in conjunction with the Borisov assumption. For some condition, we find marked deviations from Arrhenius behavior, and we are able to quantify these deviations analytically.

The second part of this work is devoted to fluid imbibition via diffusion in deformable solid which results in solid stresses that may, in turn, alter subsequent fluid uptake. To examine this interplay between diffusional and elastic fields, we employ a hybrid Monte Carlo–molecular dynamics scheme to model the coupling of a fluid reservoir to a deformable solid, and then simulate the resulting fluid permeation into the solid. By monitoring the instantaneous structure factor and solid dimensions, we are able to determine the compositional strain associated with imbibition, and the diffusion coefficient in the Fickian regime is obtained from the time dependence of the fluid uptake. Finally, for large, mobile fluid atoms, a non-Fickian regime is highlighted and possible mechanisms for this behavior are identified.

LIST OF ABBREVIATIONS

List of Abbreviations for Grain Boundary Variability

Grain Boundary	GB
Lattice	L
Isolated Grain Boundary	IGB
Grain Boundary Diffusivity	D_{GB}
Lattice Diffusivity	D_L
Grain Boundary Width	δ
Grain Size	d
Diffusion Characteristic Length for GB	L_{GB}
Diffusion Characteristic Length for Lattice	L_L
Effective Medium Theory	EMT
Triple Junction	TJ
Mass Flux	J
Finite Element	FE
Finite Difference	FD
Tri-Diagonal Matrix Algorithm	TDMA
Probability Distribution	P
Partition Function	Z
Temperature	T
Time	t
Concentration	C
Activation Energy for Diffusion	Q
Activation Energy Density of States	N(Q)
GB Volume Fraction	f_i
Lattice Volume Fraction	f_L
GB Energy	γ
Lattice Activation Energy	Q_L
GB Activation Energy	Q_{GB}
Effective Diffusivity	D_{eff}
Effective Activation Energy	Q_{eff}
centroidal Voronoi tessellation	CVT
Diffusion Pre-factor	D_0
Transition Temperature	T_t
Kronecker delta	δ_{ij}

List of Abbreviations for Fluid in Deformable Solid

Metal Organic Framework	MOF
Mass Uptake	M
Mass Flux	J
Chemical Potential	μ
Internal Energy	U
Molecular Dynamics	MD
Monte-Carlo	MC
Density Functional Theory	DFT
Boltzmann's Constant	k_B
Probability Distribution	P
Partition Function	Z
Depth of the potential well	ε
Distance at which the inter-particle potential is zero	σ
Distance between two particles	r
Dimensionality of the system	d
Particle Mass	m
Particle Velocity	v
Pressure	P
Bulk Modules	B
Inter atomic force	f_{ij}
Number of particles	N
Volume	V
Temperature	T
Time	t
Concentration	C
Grand Canonical Monte-Carlo	GCMC
Compositional Strain Tensor	ϵ_{ij}^{c}
Kronecker delta	δ_{ij}
Stress Tensor	σ_{ij}
Elastic Constant Tensor	C_{ijkl}
Young's modulus	E
Poisson's ratio	ν
Compositional Strain Parameter	η
Face Centered Cubic	FCC
de Broglie wavelength	Λ
Molecular Dynamics Step	MDS
Instantaneous Structure Factor	$S(\vec{k}, t)$
Partial Radial Distribution Function	$g_{sf}(r)$

1.

INTRODUCTION

1.1 Diffusive processes in materials science and engineering

Solid-state diffusion is defined as an atomic migration from one point to another through the solid. At a macroscopic level, a concentration gradient provides the driving force for this phenomenon. However, at atomic scale, diffusion can be explained in terms of the thermal motion of atoms and molecules.

Diffusion plays a crucial role in many materials science and engineering phenomena. For example, it controls the kinetic behavior of many processes, including: nucleation, re-crystallization, grain growth, segregation and precipitation. It is also important in understanding electrical conductivity of ionic crystals, the corrosion in metallic systems and, at elevated temperatures, oxidation and creep (e.g., in turbine blades). However,

many room temperature processes involve diffusion as well. Examples here include the permeation of fluid through membranes and catalytic reactions. Moreover, most of the time, diffusion is not a lone process, as it occurs concomitantly with chemical reactions, phase transformations, plastic deformation, crack initiation and fracture. Given its ubiquitous nature, diffusion studies yield a great deal of information about the physics of crystals and provide a key understanding of the complex and varied behavior of solids.

In this dissertation we consider diffusive processes in two separate scenarios at different length scales and materials systems. In the first scenario, we investigate the impact of grain-boundary variability on mass transport behavior in a polycrystal. More specifically, we perform both numerical and analytical studies of steady-state diffusion in prototypical microstructures for a variety of grain boundary diffusivities. This study all takes place at the macroscopic scale, and both numerical and analytical model are developed under a continuum assumption.

In the second scenario mostly we consider fluid imbibition via diffusion in a deformable solid that results in solid stresses that may, in turn, alter subsequent fluid uptake. To examine this interplay between diffusional and elastic fields, we employed a hybrid Monte Carlo–molecular dynamics scheme to model the coupling of a fluid reservoir to a deformable solid, and then simulate the resulting fluid permeation into the solid. This chapter is divided into two sections that provide background information for both selected topics.

1.2 Variable diffusivity in polycrystalline grain boundaries

Grain boundary (GB) diffusion plays a key role in many processes occurring in materials science at elevated temperatures, such as Coble creep, sintering, diffusion-induced GB migration, different discontinuous reactions, recrystallization and grain growth [1].

Since 1927 that for the first time the idea of fast diffusion along grain boundary was proposed [2], there have been many studies seeking to clarify the particular role of grain boundaries in polycrystal diffusion. The first direct evidence of GB diffusion was obtained in the early 1950s using autoradiography [3]. Fig. 1-1 shows a classic example of the GB contribution to diffusion in a polycrystal [4]. As it is evident from the figure, at low temperature, the polycrystalline sample shows higher effective diffusivity that indicates the presence of high- diffusivity paths along grain boundaries.

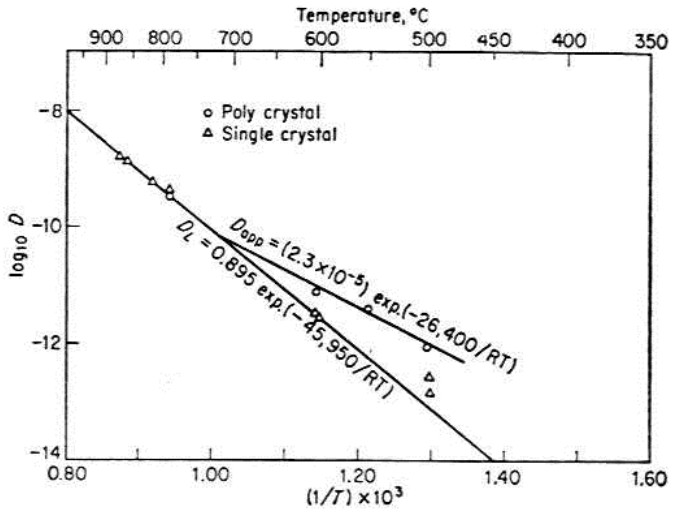

Figure 1-1 Illustration of diffusion fast path through GB's by comparing effective diffusivity of silver in single crystal and polycrystal. [5]

These efforts were followed by two major achievements in the study of GB diffusion. The first milestone was the advent of the famous Fisher model of GB diffusion in 1951 [6], followed by the development of the radiotracer serial sectioning technique. Fisher introduced the idea of an Isolated Grain Boundary (IGB) embedded between two semi-infinite low diffusivity regions as a framework for GB diffusion analysis. He solved the non-steady-state diffusion problem analytically and found that the logarithm of average concentration in the boundary varies linearly with penetration depth [6].

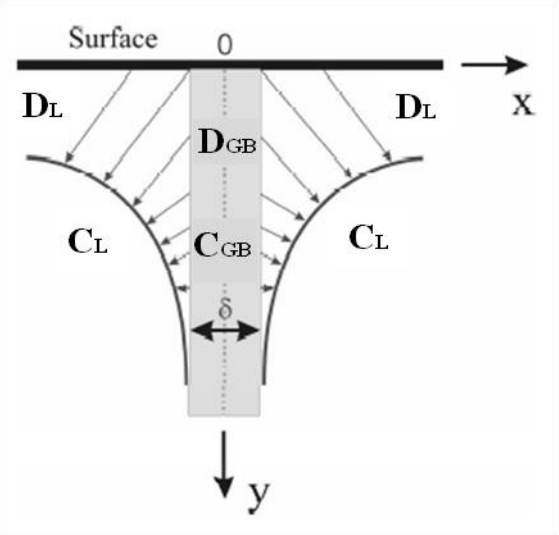

Figure 1-2 Schematic of an isolated grain boundary model [7]

Although Fisher's finding was applicable to the analysis of experimental data, the large number of approximations employed led to questions about its validity. In 1954 Whipple obtained the exact solution for an isolated grain boundary in contact with constant source [8], and Suzuoka solved the problem for an instantaneous source in 1961[9]. Both solutions were exact, but mathematically more complex than Fisher's treatment.

As mentioned above, around the same time, other researchers developed new models that applied to more realistic situations. For example, Levine and MacCallum [10] considered a polycrystalline body and assumed that both lattice and boundary diffusion mechanisms could be dominant in different penetration regimes. Their result showed that the logarithm of the average concentration varies as the 6/5 power of penetration depth, which was more accurate than Fisher's prediction. Their findings and the complementary analysis by Claire [11] paved the route for applying analytical solutions in serial sectioning experiments to measure GB diffusivity.

All aforementioned studies were associated with self-diffusion. However, the effects of impurity segregation were also investigated, first by Bokshtain in 1958 and then by Gibbs in 1966. Based on their work, the effect of segregation could be incorporated into the analysis by using a segregation factor in an expression for the GB width [2].

In 1961 Harrison proposed a kinetic classification for non-steady state diffusion in a polycrystalline microstructure. This classification is given in terms of a comparison between the diffusion characteristic length in the lattice ($\sqrt{D_L t}$) and that along the grain boundaries ($\sqrt{D_{GB} t}$) and microstructure parameters such as grain size (d) and grain boundary width (δ) [12]. As described in Fig. 1-3, in the type A regime, the diffusion length of the lattice is comparable to the diffusion length of grain boundary. This is the case for nano-crystalline materials, very long diffusion anneals, high volume diffusion coefficients or temperatures close to the melting point. If the temperature is lower or the annealing period is shorter or the grain size is larger than in the previous case, then diffusion is dominated by the so called B regime. In the type B regime, lattice and grain

boundary diffusion are both important, but concentration fields from adjacent grain boundaries do not overlap into the crystalline grain. In the type C regime, diffusional behavior of the polycrystal is almost dominated by grain boundary diffusion, and so lattice diffusion can be neglected due to low temperature or short annealing time [1,12&13].

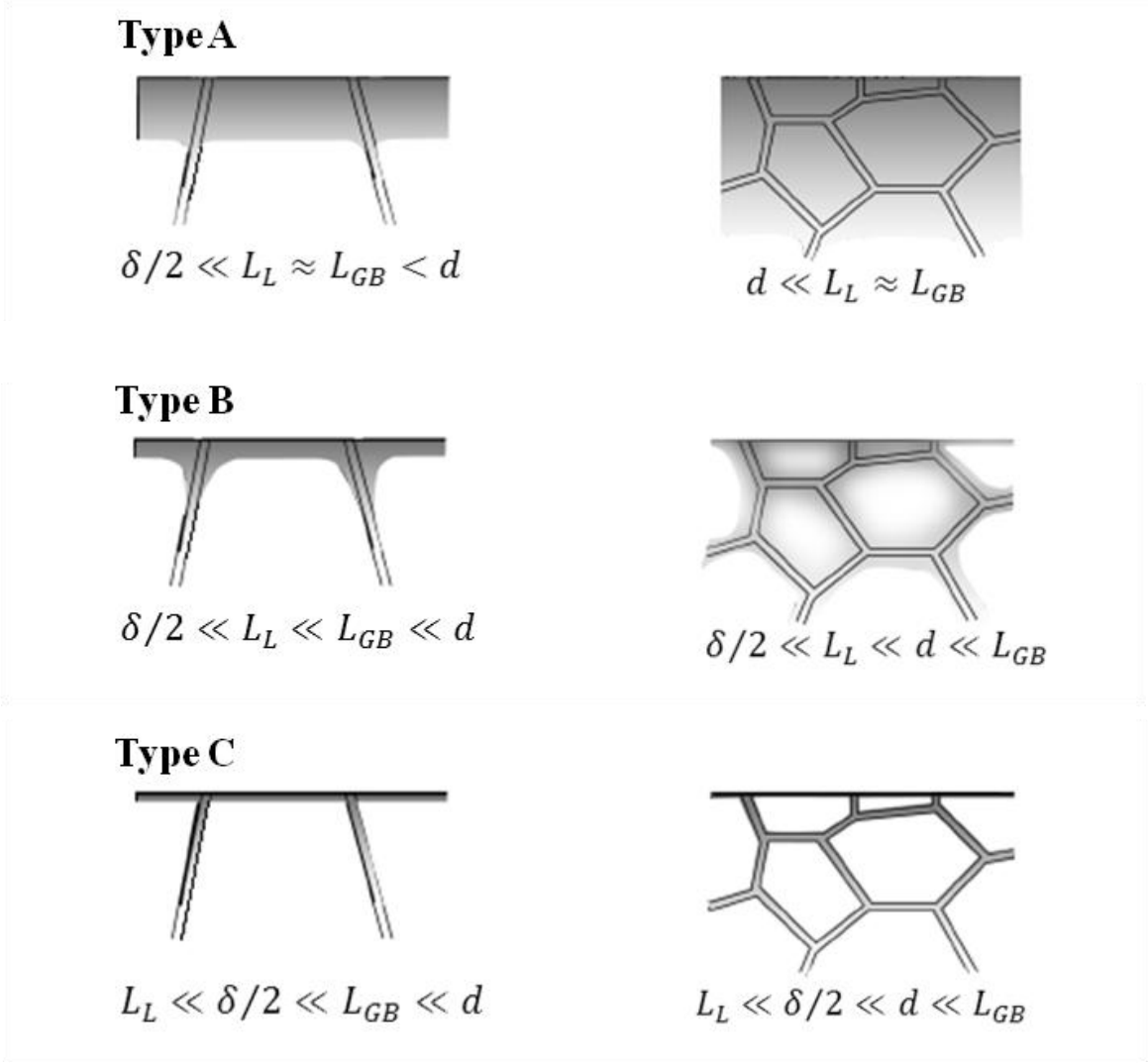

Figure 1-3 Schematic illustration of type A, B and C diffusion kinetics according to Harrison's classification. Where δ is the grain boundary width, d is the grain size; L_L is the diffusion characteristic length in the lattice and L_{GB} is the diffusion characteristic length in the grain boundary. [13]

Although these studies produced important results in the field, subsequent investigations have continued to advance the field. For instance, in 1976 Gilmer and Farrell applied the single high-diffusivity plane model to a thin film system. They found that the thin film boundary conditions led to corrections in the classical analysis [14]. In the 1990's, with increasing computing power, more sophisticated models were developed. For example, Mishin and Herzig [1] reviewed the results of atomistic simulations of GB diffusion. These studies were done by employing either molecular dynamics or kinetic Monte Carlo simulation and revealed some interesting information about diffusion coefficients and mechanisms. At the same time, Swiler and Holm, introduced the first numerical continuum model of mass transport for a polycrystalline structure. In particular, they used a finite- difference scheme to simulate transient and steady-state mass transport through a 2D microstructure and examined the effect of average grain size and GB topology [15]. In 1999 another paper, inspired by Fisher's work, was published that considered diffusion along the short circuit paths inside a grain, such as dislocations, sub-grain boundaries and interface planes. In their model, the lattice was treated as a stochastic mixture of defect-free crystalline regions and short-circuits paths [16].

Some authors have studies systems in which diffusion and chemical reactions both occur. One such study proposed a mathematical model for surface and GB kinetics and also obtained an analytical solution for the evolution of impurity concentration [17]. In 2005, the impact of a complex microstructure on polycrystalline diffusion was investigated by using both numerical and analytical methods. In this study, the diffusion equation was numerically integrated using the finite-difference method to obtain the

concentration profile for a diffusant in a simplified microstructural representation and then applied to a Voronoi model of a microstructure. The diffusive behavior is quantified by obtaining uptake curves as a function of time for different ratios of grain boundary to lattice diffusivity. In addition, approximate analytical equations describing diffusant uptake in polycrystalline microstructural models were developed [18].

Beyond studies focused on the mechanisms of GB diffusion, other workers have studied the impact of GB connectivity on the effective diffusion response of a polycrystalline microstructure. Such studies naturally involve percolation theory and Effective Medium Theory (EMT).

For example, studies of GB networks began in 1989 with the calculation of the percolation threshold for randomly assembled 2D and 3D grain-boundary networks. In 2003, Schuh et al. calculated percolation thresholds for several networks that were constrained based on crystallographic principles. They discovered that triple-junction (TJ) distributions were connected with correlated percolation [19]. In a later study, Chen and Schuh determined the domain of validity for EMT and percolation theory for a 2D honeycomb network of grain boundaries having different diffusivity contrasts. For simplicity, the lattice diffusivity was not taken into account [20]. Asymmetric effective medium equations and power-law scaling relationships were employed to evaluate the effective diffusivity for a general isotropic polycrystal. They also examined the grain size and temperature dependence of polycrystalline diffusion in terms of the apparent grain size exponent and activation energy to assess dominant diffusion processes and construct generalized diffusion mechanism maps [21].

In formulating these models, one usually assumes that all boundaries have identical diffusivities and hence, the same activation energies for diffusion. In reality, however, grain boundary character is inherently variable [22], and therefore there is a spectrum of diffusivities associated with mass transport in a polycrystal that needs to be considered.

1.3 Fluid uptake in deformable solid structures

The behavior of a solid matrix under fluid infiltration is of significance for designing new materials in various applications ranging from analytical separations to drug delivery. Several diffusion models have been developed for modeling mass transport processes. Among them is a model proposed by Fick that is commonly used because of its simplicity and mathematical tractability. This is also known as Case I or Fickian diffusion.

$$J = -D\frac{\partial C}{\partial x} \qquad (1\text{-}1)$$

$$\frac{\partial C}{\partial t} = -\frac{\partial J}{\partial x} \qquad (1\text{-}2)$$

Fick's first law (Eq. 1-1) assumes that the flux (J) passing through a unit area of material is proportional to concentration (C) gradient measured normal to the material, where the constant of proportionality is known as a diffusion coefficient (D). Fick's second law (Eq. 1-2) describes the concentration change over the time as a change in flux with respect to position [23]. Although Fickian diffusion theories have been thoroughly developed, many matrix-diffusant systems do not follow such a simplified description. In fact, Fickian diffusion is rarely seen for transport of liquid through a deformable solid systems, such as glassy polymers, metal-organic frameworks (MOF), zeolitic materials, etc. For a compliant matrix, the distortion that attends fluid uptake can lead, for example, to swelling in polymeric systems and concomitant non-Fickian diffusive behavior [24-26].

Considering Fick's second law, the mass uptake (M) can initially be represented by $M = Kt^n$, where t is the time and K and n are constants. The Fickian diffusion regime then corresponds to $n = 1/2$ and the slope in uptake curve (Fig.1-4 a), is also related to diffusion coefficient (D). Case II is associated by $n = 1$ and an anomalous diffusion regime is characterized by $1/2 < n < 1$, as shown in Fig.1-4 b,c [23,27].

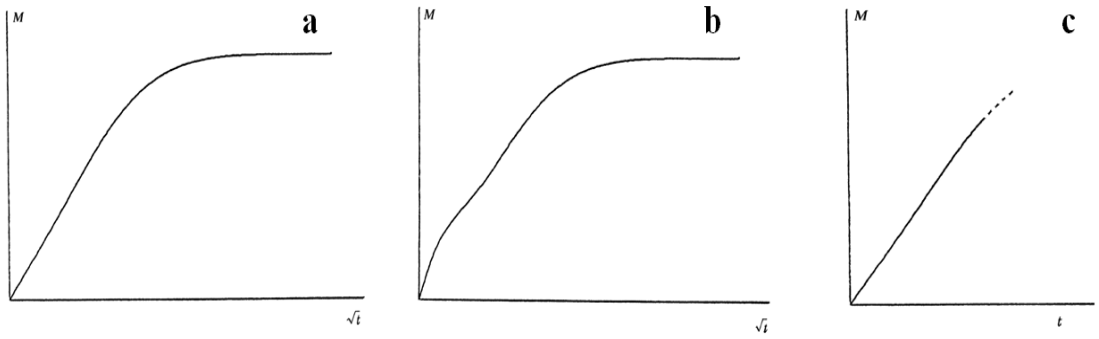

Figure 1-4 Mass uptake for different diffusion regimes; a) Fickian, b) Anomalous, c) Case II. [27]

Deviations from Fickian behavior are identified as non-Fickian diffusion regimes (Fig. 1-4 b,c). This type of behavior is usually caused by local deformation inside the matrix due to the presence of diffusant molecules that introduces a new stress field through the entire system. This local deformation, which is also called compositional strain, can affect the diffusional behavior and elastic properties of the solid [27].

Initial attempts to incorporate stress into Fick's diffusion equation date back to the work of Hartley in 1949 [28]. One plausible mechanism to describe this phenomenon is to add a stress gradient term to the normal Fickian flux. The stress in turn evolves in response to the concentration of the diffusant [29-31]. The Fickian flux in near-equilibrium transport theory is usually derived from $J \propto -C\partial\mu/\partial x$, where μ is the

chemical potential of the diffusant and is defined as $\partial U/\partial C$, where U is the system's internal energy. For ideal thermodynamic behavior $\mu(C) \propto \log C$, which results linear diffusion. Pressure on the diffusant from the material stress will increase the system's internal energy and so increase the chemical potential $\mu = \mu_0(C) + \alpha\sigma$, where σ is the material stress and α is some constant. Then the flux is given by $J = -D(C)\partial C/\partial x - E(C)\partial\sigma/\partial x$. [32]

The theoretical framework described above, is the common way to address the role of stress in fluid uptake through the solid. However, the process by which small molecules penetrate a deformable solid is very complex, and so far no mathematical model has been able to provide a complete explanation of this phenomenon. In these processes, a crucial role is played by adsorption and transport of the guest molecules. During the last decades, molecular simulation has become a powerful tool to investigate these phenomena at an atomistic length and timescale. While molecular simulations of equilibrium adsorption have reached a state where the predicted quantities (adsorption isotherms, isosteric heats) are in reasonable agreement with experiments for all but the most complex guest–host systems, this is still not the case for transport properties [33].

Several approaches exist for modeling fluid uptake in such systems. For example, Gelb and Hopkins [34] used molecular dynamics simulation to study the dynamics of fluid flow into empty cylindrical pores in which the pore-wall atoms were immobile. Ahadian *et al.* subsequently simulated imbibition of a simple fluid into a nanochannel using atomistic simulation to investigate the wall-fluid interaction [35]. More recently, Joly [36] employed molecular dynamics (MD) simulation to examine water uptake by a

carbon nanotube, and Stukan *et al.* [37] also used MD to investigate the role of nanopore roughness on fluid imbibition.

Given the inherent computational demands of simulating fluid imbibition at the atomic scale, most such simulations of this process take the matrix atoms to be immobile. This assumption is often justified, especially for fluid atoms having small radii, in situations where elastic energy considerations are relatively unimportant [33]. However, the modeling of elastic deformation that attends fluid uptakes necessitates the incorporation of matrix stresses via the inclusion of matrix-atom coordinates.

2.

SIMULATION METHODS

2.1 Simulation in materials science and engineering

Computational modeling has been employed in science and engineering for many years, but recent development in computer technology have led to significant increases in computational power and, hence, greater capabilities. Moreover, the relatively easy access to high- performance computing resources has led to the application of computational methods that between theory and experiment. The role of these methods is twofold. On one hand, computational methods can be used to examine current available theories, enabling materials properties predictions. On the other hand, disagreements between simulation and experiment indicate that the underlying theory may need revision. This back and forth between theory and experiment thereby generates unique insights into the problem under study. If the simulation results agree with experimental

findings, the underlying theory is validated and may be employed in the discovery and design of new materials. Hence, finding more accurate simulation methods is a win-win proposition that can serve both theorists and the experimental community.[38,39]

There are several simulation methods that are appropriate for different length and time scales. Fig. 2.1 describes this broad range of methodologies in a schematic manner.

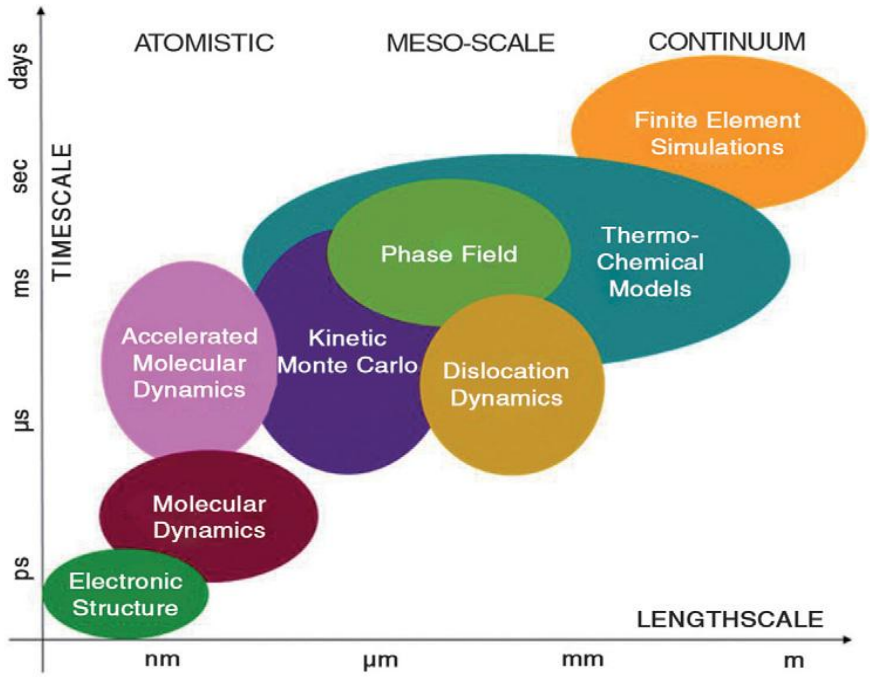

Figure 2-1 Multi-scale methods used for materials model development and computer simulations.[40]

From continuum mechanics all the way down to quantum mechanics, different methods can predicts variable materials properties depending on the length and time scales involved. In the continuum approach, finite-element (FE) and finite-difference (FD) simulations mostly deal with bulk properties and are appropriate for describing heat and mass transport, mechanical properties and so on. (We note that these methodologies can sometime be employed in the mesoscale regime as well.) At smaller length scales,

mesoscale methods are used to describe microstructural evolution that occurs, for example, during solidification, crystallization and grain growth. At the atomic scale, atomistic simulation is appropriate, and molecular dynamics (MD) and Monte Carlo (MC) simulations are the most important methods at this scale. These methods are established based on a Hamiltonian and therefore involve canonical quantities, such as atomic positions and, in the case of MD, momenta. Finally, in the quantum-mechanical domain, ab-initio and density-functional theory (DFT) are appropriate. The ultimate goal of these methods is to be able to predict the electronic structure of the materials in different situations. These methods are extremely computational intensive, involving only a couple of hundred atoms, but they are helpful in revealing basic information about electronic structure. This type of information is useful for designing new materials and also could be used as initial information for input into higher-level simulations, such as MD and MC. Obviously each simulation method has its own limitations and drawbacks that should be taken into account when choosing one for a particular problem. In following sections, we describe three different methods that we have used in this research in some detail.

2.2 Finite Difference Simulation

The finite-difference method is particularly useful for the continuum modeling of materials. In particular, this method enables the approximate solution of differential equations that describe physical processes such as mass diffusion, heat transfer and fluid flow, as well as the electrostatic field resulting from charge distributions in space. All techniques we are going to develop in this section are immediately available for application in these different areas. The main idea of this method is to find a mathematical description of the problem of interest based on flux laws and conservation principles, and then try to solve the appropriate differential equation by employing numerical method. These numerical methods are classified by their method of discretization. Since in our research we are used Control-Volume based Finite Difference, in following discussion we examine this method in some detail for diffusion problems [41].

2.2.1 Control Volume Formulation

In this method, the calculation domain is divided into a non-overlapping control-volumes and the differential equation is integrated over each of them. Every control volume has a grid point inside it, and its piecewise profile expresses the variation of concentration (in a case of diffusion) between the grid points. The result a discretized equation containing the value of concentration (C) for all grid points. We start from two-dimensional steady-state diffusion equation given by

$$\frac{\partial}{\partial x}\left(D\frac{\partial C}{\partial x}\right)+\frac{\partial}{\partial y}\left(D\frac{\partial C}{\partial y}\right)+S=0 \qquad (2\text{-}1)$$

where D is the diffusion coefficient and S is a source term. Fig. 2-2 shows schematic of a l control volume with grid point P and its neighbors : East, West, North and South.

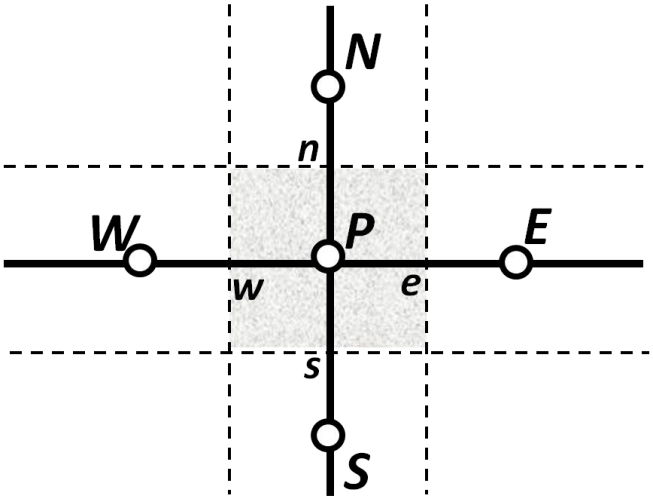

Figure 2-2 Schematic of a control volume with its associated grid points and faces

To integrate the governing equation over the control volume we have;

$$\int \left[\frac{\partial}{\partial x}\left(D\frac{\partial C}{\partial x}\right)+\frac{\partial}{\partial y}\left(D\frac{\partial C}{\partial y}\right)+S\right].dA=0 \qquad (2\text{-}2)$$

Where A is the area.

$$\int_s^n \int_w^e \left[\frac{\partial}{\partial x}\left(D\frac{\partial C}{\partial x}\right)+\frac{\partial}{\partial y}\left(D\frac{\partial C}{\partial y}\right)+S\right].dx.dy=0 \qquad (2\text{-}3)$$

$$\int_s^n \int_w^e \left[\frac{\partial}{\partial x}\left(D\frac{\partial C}{\partial x}\right)\right].dx.dy+\int_s^n \int_w^e \left[\frac{\partial}{\partial y}\left(D\frac{\partial C}{\partial y}\right)\right].dx.dy+$$

$$\int_s^n \int_w^e S\,.dx.dy=0 \qquad (2\text{-}4)$$

In a case that source term depends on concentration (diffusion-reaction problem), we can express this dependency in a linear form as $S_C + S_p C_P$. Where S_p is a rate coefficient and S_C is a constant.

$$\int_s^n \int_w^e \left[\frac{\partial}{\partial x}\left(D\frac{\partial C}{\partial x}\right)\right].dx.dy + \int_s^n \int_w^e \left[\frac{\partial}{\partial y}\left(D\frac{\partial C}{\partial y}\right)\right].dx.dy + \int_s^n \int_w^e (S_C +$$

$$SpCP).dx.dy=0 \qquad (2\text{-}5)$$

Using central difference scheme and taking first integrals led to;

$$\int_s^n \left[\left(D\frac{\partial C}{\partial x}\right)_e - \left(D\frac{\partial C}{\partial x}\right)_w\right].dy + \int_w^e \left[\left(D\frac{\partial C}{\partial y}\right)_n - \left(D\frac{\partial C}{\partial y}\right)_s\right].dx +$$

$$sn(SC+SpCP)\Delta xdy=0 \qquad (2\text{-}5)$$

Considering Δy and Δx as control volume sides we will get;

$$\left[\left(D\frac{\partial C}{\partial x}\right)_e - \left(D\frac{\partial C}{\partial x}\right)_w\right]\Delta y + \left[\left(D\frac{\partial C}{\partial y}\right)_n - \left(D\frac{\partial C}{\partial y}\right)_s\right]\Delta x + (S_C +$$

$$S_p C_P)\Delta x \Delta y = 0 \qquad (2\text{-}6)$$

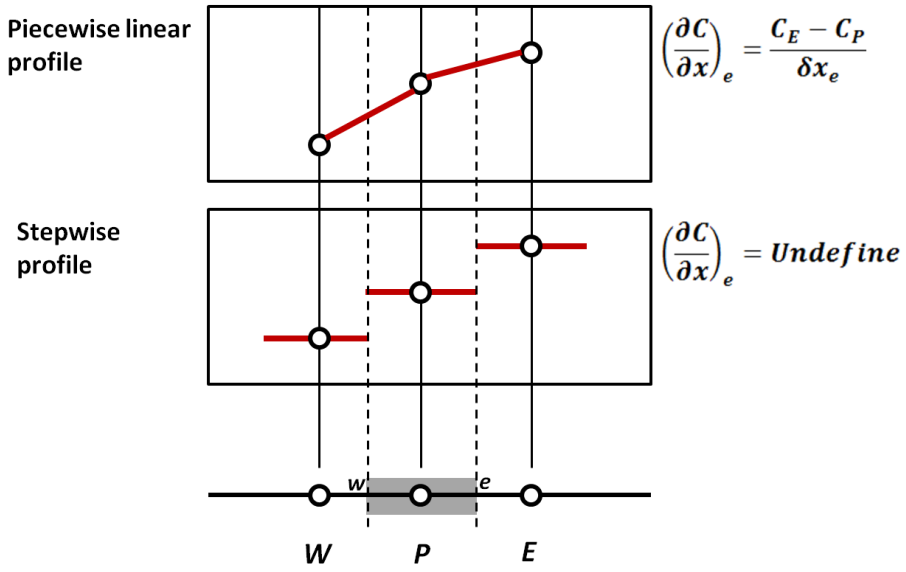

Figure 2-3 Piecewise linear vs. stepwise profile assumptions [41]

At this point, we need to evaluate gradient terms based on proper assumption to finalize our discretization. Fig.2-3 shows two different assumptions for profiling concentration between the points. As it is obvious, we are using piecewise linear profile for our discretization.

$$\left[D_e \frac{C_E - C_P}{\delta x_e} - D_w \frac{C_P - C_W}{\delta x_w}\right] \Delta y + \left[D_n \frac{C_N - C_P}{\delta y_n} - D_w \frac{C_P - C_S}{\delta y_s}\right] \Delta x + (S_C + S_p C_P) \Delta A$$

(2-7)

$$=> \left[\frac{D_e}{\delta x_e} C_E - \frac{D_e}{\delta x_e} C_P - \frac{D_w}{\delta x_w} C_P + \frac{D_w}{\delta x_w} C_W\right] \Delta y + \left[\frac{D_n}{\delta y_n} C_N - \frac{D_n}{\delta y_n} C_P - \frac{D_s}{\delta y_s} C_P +\right.$$

$$Ds\delta ysCS\Delta x + SC\Delta A + SPCP\Delta A = 0 \qquad (2\text{-}8)$$

Factoring and reordering above equation conducts us to;

$$\left(\frac{\Delta y D_e}{\delta x_e}\right) C_E + \left(\frac{\Delta y D_w}{\delta x_w}\right) C_W + \left(\frac{\Delta x D_n}{\delta y_n}\right) C_N + \left(\frac{\Delta x D_s}{\delta y_s}\right) C_S - \left(\frac{\Delta y D_e}{\delta x_e} + \frac{\Delta y D_w}{\delta x_w} + \frac{\Delta x D_n}{\delta y_n} + \frac{\Delta x D_s}{\delta y_s} -\right.$$

$$SP\Delta ACP + SC\Delta A = 0 \qquad (2\text{-}9)$$

By replacing all parenthesis with a_E, a_W, a_N, a_S and a_P respectively and put b = $S_C \Delta A$ we will get;

$$a_E C_E + a_W C_W + a_N C_N + a_S C_S - a_P C_P + b = 0 \qquad (2\text{-}10)$$

In this order the final equation for evaluation of concentration at point ***P*** based on its neighbors would be;

$$a_P C_P = a_E C_E + a_W C_W + a_N C_N + a_S C_S + b \qquad (2\text{-}11)$$

Or

$$a_P C_P = \sum a_{nb} C_{nb} + b \qquad (2\text{-}12)$$

To have final evaluation of concentration field in entire computational domain, equation 2-12, should be written for all grid points and all neighbor coefficients should be

determined. Solving this large set of equations is only possible by applying numerical methods based on boundary conditions. There are different numerical methods to solve such problems, all of them employing iterative methods and following same principles as follows:

1. Guess or estimate for initial value of concentration at all grid points.
2. Calculate tentative values of the coefficients from initial concentrations
3. Solve the nominally linear set of algebraic equation to get new ***C'***s
4. With new ***C'***s as a better guess, return to step **2** and repeat the process until further iterations cease to produce any significant change in ***C'***s (as a criteria for convergence).

In our model we applied the Tri-Diagonal Matrix Algorithm (TDMA), which is based on the principles outlined above. More detailed information about this algorithm can be found at [41,42].

The aforementioned model is capable of modeling diffusion phenomena in a steady-state condition. However, by changing the governing equations, one can transform the procedure to model non-steady state diffusion. As our focus here is on the steady-state regime, we refer the reader to the references for a discussion of the methodology for the non-steady-state regime. [41]

2.3 Monte-Carlo Simulation

The Monte Carlo method was developed at Los Alamos National Laboratory, where for the first time it was proposed by Ulam and von Neumann as a means for evaluating a multivariable integral to describe the diffusion of neutrons in fissionable materials. In 1947 Metropolis coined the name of "Monte Carlo" due to extensive use of random numbers in this method and since then it has been developed to model various phenomena in different fields. The typical problem that can be addressed by MC is a system with a known Hamiltonian at given temperature that obeys Boltzmann statistics.[43]

In statistical mechanics, the Boltzmann distribution is defined as a probability distribution (P) over various possible states of a system, with the form

$$P(\text{state}) \propto e^{-U/k_B T} \qquad (2\text{-}13)$$

where U is state potential energy, and $k_B T$ is the product of Boltzmann's constant and thermodynamic temperature, which is called as $1/\beta$ in statistical mechanics. This distribution applied to systems having fixed composition that are in thermal equilibrium. In other words, it describes the average distribution of weakly interacting particles over various energy states in thermal equilibrium and is applicable when the temperature is high enough (above Debye temperature) or the particle density is low enough to render quantum effects negligible. The Boltzmann distribution can be employed to obtain the mean value of some macroscopic variable, say A, by taking an integral over all the phase space using the expression

$$\langle A \rangle = \frac{\int dr^N A(r^N) exp[-\beta U(r^N)]}{\int dr^N exp[-\beta U(r^N)]} \qquad (2\text{-}14)$$

In the equation above, r^N stands for the coordinates of all N particles. The denominator is the partition function (Z), which plays a key role in statistical mechanics and reveals information about all available energy states in the system, is given by

$$Z = \int dr^N exp[-\beta U(r^N)] \qquad (2\text{-}15)$$

It is very difficult, in general, to determine the partition function for a given system. However, what we wish to know is the ratio of two integrals, as in Eq. (2-14). Metropolis et al. showed that it is possible to devise an efficient Monte Carlo scheme to sample such a ratio, by biasing the state's selection itself, and weighting each state equally. In this manner, the calculation wastes less time exploring configurations that don't contribute to the average. [38]

2.3.1 Metropolis Algorithm

To illustrate the implementation of the Metropolis method, consider atoms confined to a simulation cell, as shown in Fig. 2-3. Each particle could be considered as a single atom or molecule. Interactions between the atoms can be described in terms of an interaction potential that depends on the nature of the bonding in the system. For simplicity, we are going to use the Lennard-Jones potential, which is usually used to approximate the interaction between a pair of neutral atoms or molecules, and is given by

$$U(r) = 4\varepsilon \left[\left(\frac{\sigma}{r}\right)^{12} - \left(\frac{\sigma}{r}\right)^{6} \right] \qquad (2\text{-}16)$$

where ε is the depth of the potential well, σ is the finite distance at which the inter-particle potential is zero and r is the distance between two particles.

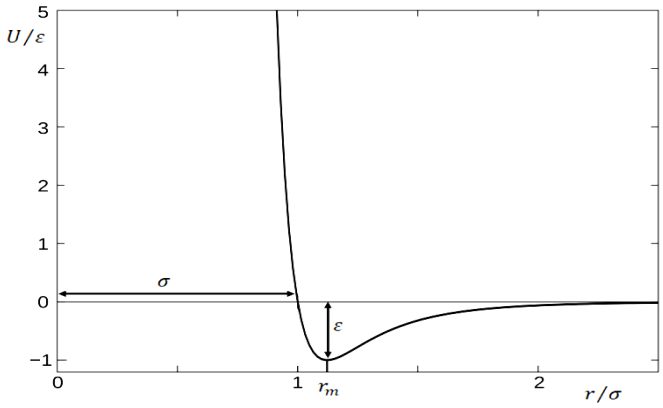

Figure 2-4 Schematic plot for Lennard-Jones potential.

As shown in Fig. 2-2, r_m is the distance at which the potential reaches its minimum value ($-\varepsilon$). This distance represents the equilibrium bound distance between two given particles, and one can easily determine that $r_m = 2^{1/6}\sigma$ by direct differentiation. These parameters can be fitted to reproduce experimental data or accurate first-principles calculations. Due to its computational simplicity, the Lennard-Jones potential is used extensively in computer simulations, even though more accurate potentials exist.[39,44]

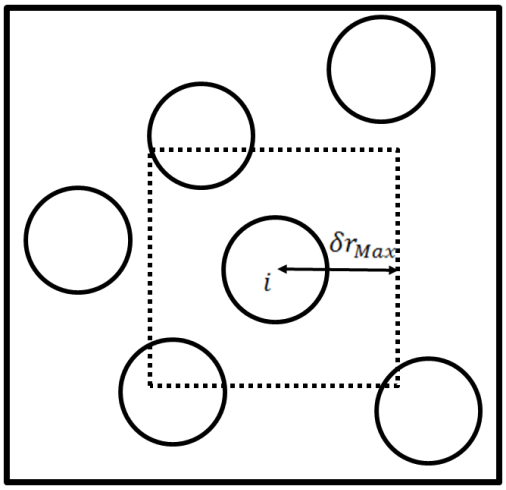

Figure 2-5 Schematic of initial configuration for implementing Metroplois algorithm[1]

Fig. 2-5 shows schematic of system configuration at state *m*. Using the Metropolis method, the system can transit from current state (*m*) into any one of its neighboring states *n* with equal probability. A MC move begins by randomly picking particle *i* and giving it a random displacement along each coordinate direction, with a maximum displacement in each direction of r_{Max} . In other words, the particle displacement is confined to a square (cube in 3D) with a side length of $2\delta r_{Max}$. Once this move is made, the energy difference between old and new configurations is calculating using the interatomic potential.

The energy calculation is the most computationally expensive part of this type of modeling, since it has to be done for every pair of particle in the system. There are, however, some shortcuts that can reduce this calculation time. First of all, there is no need to calculate the energy of entire system after every single move. Once the total energy is calculated at the beginning of the simulation, subsequent calculations involve only the energy difference between two consecutive moves. Thus, for a pair potential, we need only calculate the interaction energy between particle *i* and the rest of the system before and after an attempted atomic displacement. This is possible because an attempted MC move involves just one particle, so only the change in the configuration of particle *i* must be considered. The second trick is that, even for particle i, we don't need to consider all of the other particles. The only relevant particles are the ones that are close neighbors. The reason for this is that, as is clearly shown in Fig. 2-4, the interaction energy between two particles vanishes after certain distance. Thus, there is no need to calculate the interaction energy for particles by more than the cut-off radius. This cut-off

radius is determined for each system based on its particular potential. In Lennard-Jones potential it is usually assumed that $r_c = 2.5\sigma$.

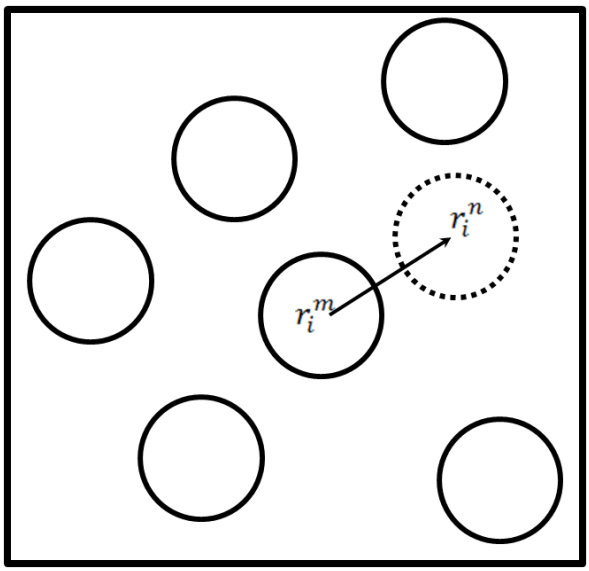

Figure 2-6 System transition from state *m* into the state *n* through one MC move. [38]

Another issue that should be addressed is the size of the system. The ultimate goal of MC simulation and other atomistic modeling is to reveal some information about bulk properties of the system. However, even by using most powerful supercomputer in the world, we cannot model more than couple millions particles, which is still tiny amount in comparison with Avogadro's number (6.02×10^{23}) for one mole of material. Another problem is that, for system with small number of particles, a large fraction of particles may be near a surface and will therefore not experience a bulk environment.

To avoid all these shortcomings in modeling bulk properties, it is necessary to construct boundary conditions that mimic the presence of bulk surrounding the system. This is usually achieved by applying periodic boundary conditions. In this method, the entire system is considered as a unit cell and is repeating periodically in space. With this

construction, all particles inside the original unit cell see an infinite bulk around themselves. Considering the cut-off radius for interaction, each particle needs to probe the square area of $2r_c \times 2r_c$ around itself for energy calculation. The calculation of interparticle distances using this approach is explained in detail in [38,39].

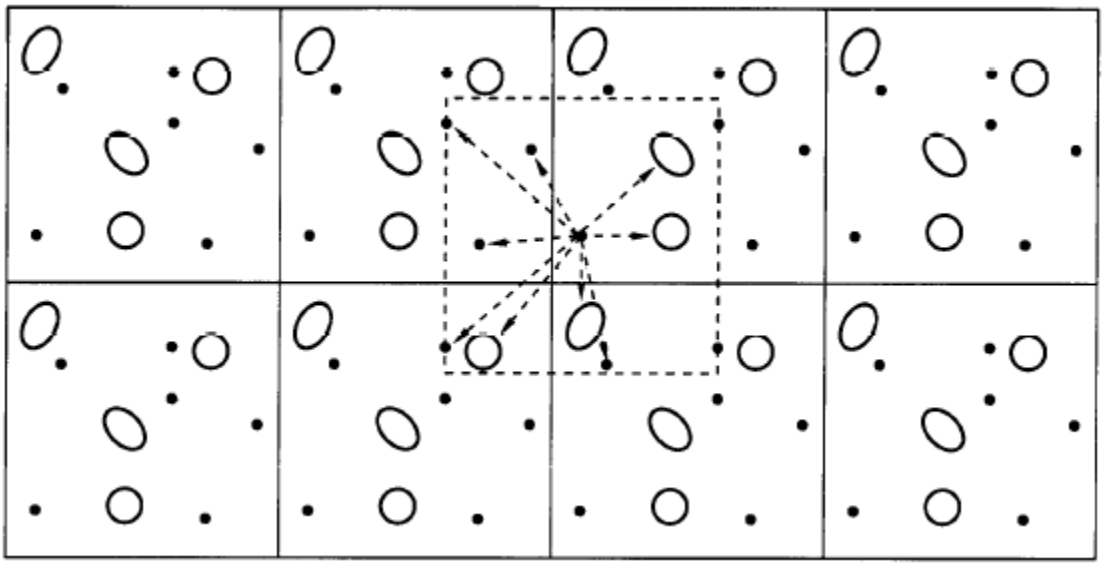

Figure 2-7 Schematic representation of periodic boundary condition [39]

As mentioned above, by calculating the distance for all particles within the cut-off radius, the energy difference (δU_{nm}) for each move can be obtained from

$$\delta U_{nm} = \sum_{j=1}^{N} U\left(r_{ij}^{n}\right) - \sum_{j=1}^{N} U\left(r_{ij}^{m}\right) \qquad (2\text{-}17)$$

Based on Metropolis method, the value of δU_{nm} is used to decide whether or not to accept a trial move. To explain this in more detail, it is good to again consider partition function and its ability to generate a computable ratio to determine the probability of having our system in state *m*, namely

$$P_m = \frac{\exp\left[-\beta U(r^m)\right]}{\int dr^N exp[-\beta U(r^N)]} \qquad (2\text{-}18)$$

The probability ratio between new and old states is therefore given by

$$\frac{P_n}{P_m} = \frac{Z^{-1}\exp\left[-\beta U(r^n)\right]}{Z^{-1}\exp\left[-\beta U(r^m)\right]} = \exp\left[-\beta\, \delta U_{nm}\right] \qquad (2\text{-}19)$$

There are two possibilities here. If $\delta U_{nm} \leq 0$ the new state has an equal or lower energy relative to the old state. In that case the move always is being accepted.

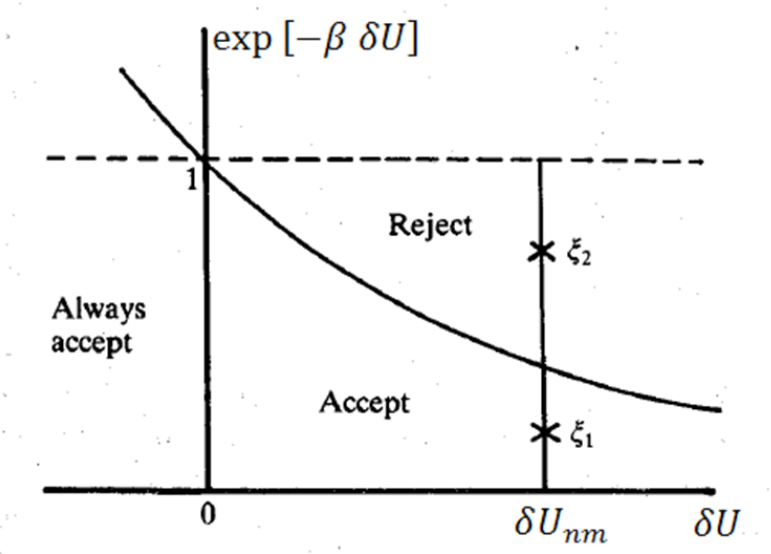

Figure 2-8 Acceptance criteria for MC move [38]

However, if $\delta U_{nm} > 0$, the move is accepted with a probability proportional to $\exp\left[-\beta\, \delta U_{nm}\right]$. This is accomplished in practice by selecting a random number ξ that is generated uniformly in the range of [0,1). If this random number is less than $\exp\left[-\beta\, \delta U_{nm}\right]$ the move is accepted. Otherwise, the move is rejected. This procedure is illustrated schematically in fig. 2-8. A good rule of thumb is that the acceptance/rejection ratio is about 50%. Adjusting this ratio can be done by changing δr_{Max}, which determines the size of a trial move. If this parameter is too small, a majority of moves will be accepted as little change has been made to the system

configuration in a trial move move. If, however, δr_{Max} is large, the rejection rate may be too high given possible particle overlaps. It is also necessary to all particles have a chance to attempt a displacement. Finally, a MC time step is defined such that each particle in the system has an opportunity to move at least once. [38,39]

2.4 Molecular Dynamics Simulation

Molecular dynamics simulation is another method for computing the thermodynamic and transport properties of many-body system. In this approach, the motion of particles (atoms or molecules) obeys the laws of Newtonian physics. This assumption can cover wide range of materials with reasonable accuracy. Only for modeling the translational and rotational motion of light atoms and molecules (e.g., He, H2, D2) or vibrational motion with a frequency $hv > k_B T$ is it necessary to consider quantum effects. MD simulation is in many aspects similar to real experiment. We first initialize our system and evolve the system by solving Newton's equations of motion for the entire system until equilibrium is obtained. At this point one can compute equilibrium averages. What MD simulation provides us are the positions and momenta of the particles at each time step that have been obtained by following the dynamics of the system. The equilibrium averages can be calculated from this raw data. For example, applying the equipartition theorem to all degrees of freedom in the system leads to the average kinetic energy relation

$$\langle \frac{1}{2} m v^2 \rangle = \frac{1}{2} k_B T \qquad (2\text{-}20)$$

where m and v are particle mass and velocity, respectively. Using the above relation in the simulation, we can determine temperature of the system as

$$T(t) = \sum_{i=1}^{N} \frac{m_i v_i^2(t)}{k_B N_f} \qquad (2\text{-}21)$$

Here, we measure total kinetic energy of the system and divide that by the number of degrees of freedom (N_f) to acquire temperature at each time step. One can also calculate

the pressure. For pairwise additive interaction one can evaluate pressure based on the virial theorem as follows,

$$P = \rho k_B T + \frac{1}{dV}\langle \sum_{i<j} f(r_{ij}).r_{ij} \rangle \qquad (2\text{-}22)$$

where d is a dimensionality of the system, < > denote an equilibrium average and $f(r_{ij})$ is the force between particles i and j at a distance r_{ij}.[39]

2.4.1 MD Algorithm

The steps in a molecular dynamics program can be summarized as follows.

- System setup
- System Initialization
- Force calculation
- Integration of Newton's equation of motion
- Quantity measurements

To start simulation we must determine the size of the system under consideration (i.e., the dimensions of the simulation cell), the number of particle in the cell and the interaction potential. To initialize the system, each particle is assigned a position and velocity. It is common to use a crystal lattice for the spatial assignment, while the velocities may be assigned according to a probability distribution. For example, the Maxwell distribution function can be used to generate initial velocity components in all three directions using Eq. 2-21 to obtain a target temperature.

The force calculation is the most time consuming part of the MD program as one must calculate the force on all of the particles. In the simplest case, if we consider a pair potential, we must account for the contribution from all of a particle's neighbors. For particles *i* and *j*, the distance, *r*, is calculated from

$$r = \sqrt{\left(x_j - x_i\right)^2 + \left(y_j - y_i\right)^2 + \left(z_j - z_i\right)^2} \qquad (2\text{-}23)$$

If we only consider the interaction from the nearest image of another particle then, for a system with N particles, we must evaluate $N \times (N-1)/2$ pair distances. However, we already know that we can reduce this number by the methods mentioned at MC section, such as doing force calculations just for $r \leq r_c$. In classical mechanics, the force $\vec{f}(\vec{r}) = -\partial U(\vec{r})/\partial \vec{r}$, and so for the *x* component of force we have that

$$f_x(r) = -\frac{\partial U(r)}{\partial x} = -\left(\frac{x}{r}\right)\frac{\partial U(r)}{\partial r} \qquad (2\text{-}24)$$

Thus, for the Lennard-Jones potential, one finds that

$$f_x(r) = \frac{48x}{r^2}\left(\frac{1}{r^{12}} - 0.5\frac{1}{r^6}\right) \qquad (2\text{-}25)$$

Similar calculations can be done on for the other directions for each pair of particles and the results added together to evaluate the force on particle *i*. Since $f_{ij}(r) = -f_{ji}(r)$ one can also reduce the number of calculations that must be done.

After computing all of the required forces, one can integrate Newton's equations of motion to predict the next configuration of the system. One way to do this is by using the Verlet algorithm this is widely used in MD simulations. This method is based on Taylor expansions for $r(t + \Delta t)$ and $r(t - \Delta t)$, where Δt is the integration time step. Upon summing these two expansions one obtains

$$r(t+\Delta t) = 2r(t) - r(t-\Delta t) + \frac{f(t)}{m}\Delta t^2 \qquad (2\text{-}26)$$

To update the velocities, we need to evaluate force again for the new configuration. One can then calculate the new velocity from the relation

$$v(t+\Delta t) = v(t) + \frac{f(t+\Delta t)+f(t)}{2m}\Delta t \qquad (2\text{-}27)$$

Once the particle positions and velocities are calculated, one can generate the next configuration for the system. The system trajectory in phase space is generated by repetitively calculating forces and updating particle positions and momenta. Fig. 2-9 shows a flowchart for MD simulation program.

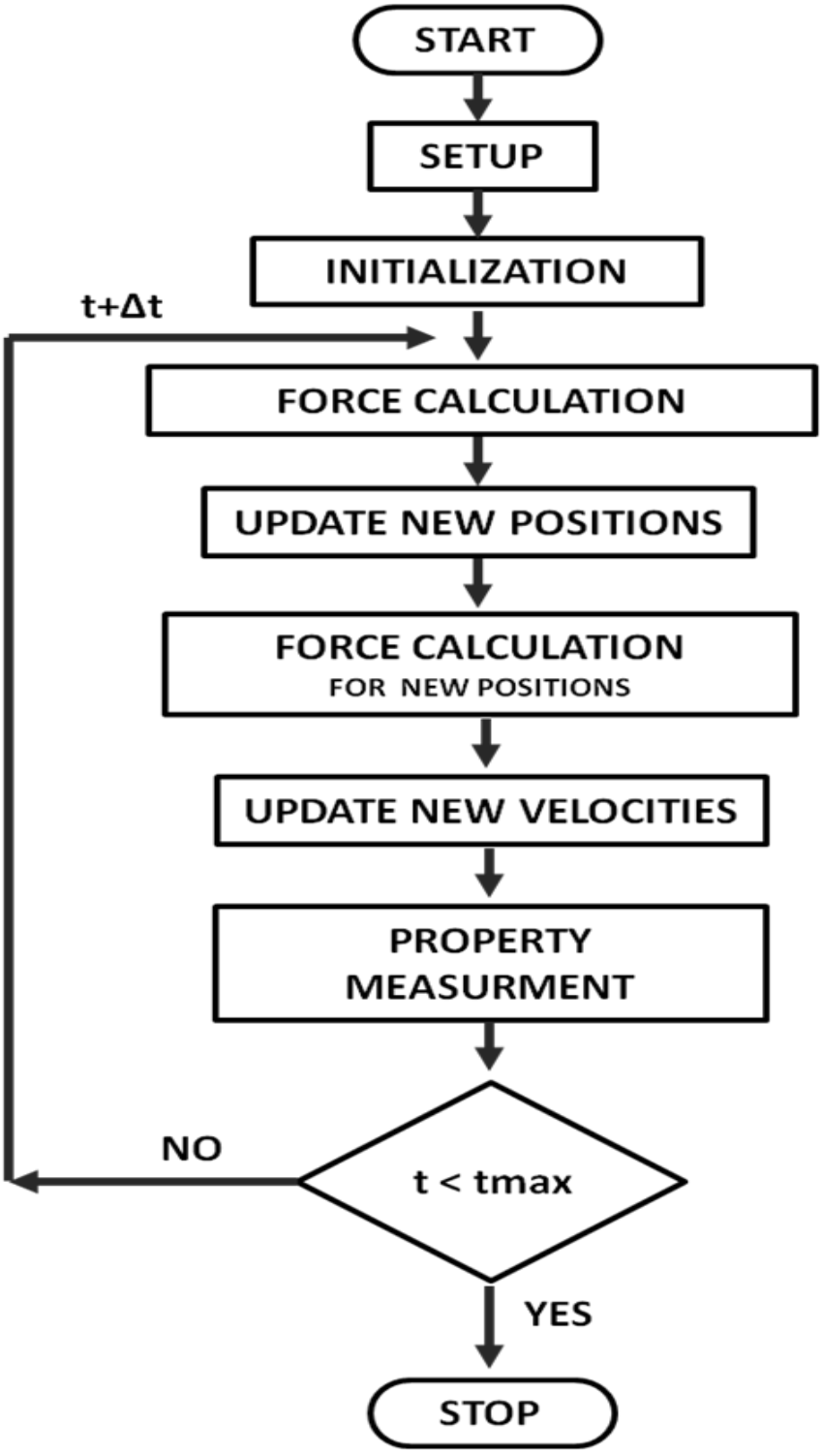

Figure 2-9 Flowchart of Molecular Dynamics program

In a conventional MD simulation, as described above, the total energy of the system and its total linear momentum are conserved during the run and are therefore constants of motion. These two criteria are commonly used to ensure the accuracy of a program (i.e., to verify that the integration of Newton's equation of motion is correct). In the language of statistical mechanics, a system having constant N,V,E (number of particles, volume, and total energy) is called the micro-canonical ensemble. By contrast, a conventional MC simulation is based on the canonical (constant N,V,T) ensemble. There are other ensembles, such as the grand-canonical ensemble (μ,V,T) which applies at constant chemical potential, μ, or the isobaric-isothermal ensemble which applies at pressure and temperature constant. The use of these ensembles provides flexibility in computing different properties via statistical averaging. The detailed implementation of these ensembles in a computer simulation is described in more detail elsewhere [38,39].

3.

VARIABLE GRAIN BOUNDARY DIFFUSIVITY IN POLYCRYSTALLINE MICROSTRUCTURE

3.1 Background

Most models of grain-boundary (GB) diffusion in polycrystals assume, for tractability, that all boundaries have identical diffusivities and, hence, the same activation energies for diffusion. For all but the simplest of microstructures the reality is, of course, much more complex. In particular GB character is inherently variable [45], and therefore there is a spectrum of diffusivities associated with the boundaries that comprise polycrystal. Moreover, there is accumulating evidence that layering transitions (i.e., complexion) [46, 47] can occur at grain-boundaries as a function of temperature or pressure, thereby altering boundary structure and chemistry and, therefore, boundary kinetics. The interplay among these factors in systems with interconnected GB networks

makes the determination of the effective diffusion response for polycrystals non-trivial in many cases. In particular, the effective activation energy may be a function of temperature and will be dictated by a complicated microstructural average.

A number of simplified models of polycrystalline mass transport in idealized geometries have been formulated and quantitative results have been obtained in certain diffusive regimes. For example, Whipple and Suzuoka considered an isolated, isotropic grain-boundary (GB) region with a high diffusivity surrounded by a lower diffusivity bulk region and were able to obtain approximate, analytical solutions to the diffusion equation [8, 9]. The solutions can be applied to the description of polycrystalline diffusion in the case of well-separated boundaries (i.e., large grain size) and small lattice diffusion lengths (i.e., type-B diffusion kinetics) [48]. More recently, this analysis has been generalized to the case of thin films by Gilmer and Farrell [14, 49]. Moreover, Fisher [6] also employed an idealized representation of an isolated grain boundary to obtain the concentration profile in the boundary when there is a constant surface source, neglecting volume diffusion from that source. As the aforementioned models are based on structureless boundaries, other workers [50] have extended these treatments by incorporating more realistic descriptions of low-angle boundary structure in diffusive models that comprise arrays of dislocations. In addition, others have sought to include microstructural features of a polycrystal in their analysis [10], and to formulate numerical models of non-steady state diffusion in idealized polycrystals [18].

In recent years, some investigators have begun to examine the role of GB variability in the context of diffusion in polycrystalline media. For example, Schuh and coworkers [19] have modeled diffusion on a heterogeneous GB network comprising boundaries with

two distinct diffusivities and assessed the accuracy of effective medium approximations in determining an effective diffusivity. More recently, using a similar approach, Li and Holland [52] examined the interplay between network topology and boundary character, as described by two distinct GB diffusion coefficients. While this work provides an important connection between boundary structure and measurable kinetic properties, it is also desirable to link the effective diffusivity to realistic GB character distributions and to examine the temperature dependence of the activation energy for diffusion to identify diffusive regimes and to quantify deviations from Arrhenius behavior.

3.2 Objectives

In this work we assess the impact of GB variability on mass transport behavior in two models of a polycrystal by employing both numerical and analytical methods to extract an effective diffusivity from a steady-state diffusion profile. We consider both idealized cases in which the spectrum of GB diffusivities is discrete and the case in which there is a continuous spectrum of diffusivities. In this latter case, we link the distribution of boundary diffusivities to experimentally obtained GB character data and determine the effective diffusivity for two prototypical microstructures. The dependence of the corresponding effective activation energies on temperature is also calculated and compared to standard Arrhenius behavior. Finally, we examine the impact of GB phase transition known as a complexion transition on diffusion in a polycrystal.

3.3 Simulation Methodology

Steady-state GB diffusion in a two-dimensional system having a polycrystalline microstructure is modeled here by employing a control-volume based, finite-difference method to solve numerically for the concentration field, $c\ (\vec{r})$, as a function of position, $(\vec{r})$. For this inhomogeneous system in a cell of size $\ell \times \ell$, one can regard the diffusivity, $D\ (\vec{r})$, can also be regarded as a function of $\vec{r}$. The determination of an effective diffusivity, D_{eff} , for the system begins with the assignment of diffusivities and initial concentrations $c\ (x, y)$, to both lattice and GB sites of a square lattice, along with the imposition of the Dirichlet boundary conditions $c\ (x, 0) = 1$ and $c\ (x, \ell) = 0$ and the Neumann conditions $\partial c(0, y)/\partial x = \partial c(\ell, y)/\partial x = 0$ (see Fig. 3-1).

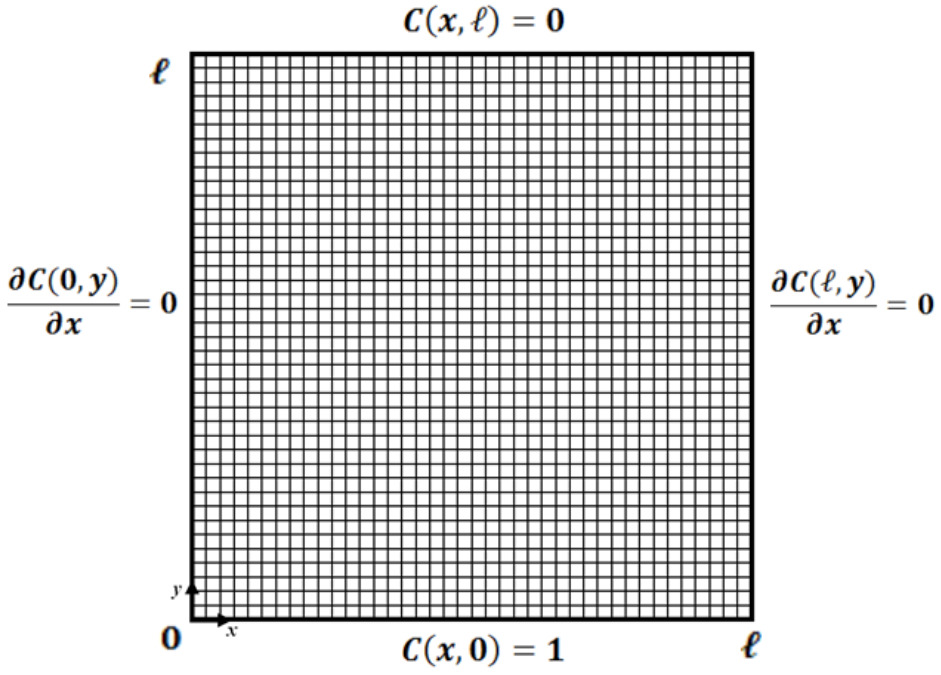

3-1 A schematic of the simulation cell showing the location of the applied boundary conditions.

Standard central-difference methods [42] are then used to discretize the differential equation

$$\vec{\nabla}.\left[D\ (\vec{r})\vec{\nabla}c\ (\vec{r})\right] = 0 \qquad (3\text{-}1)$$

and a tridiagonal matrix algorithm is employed to obtain a numerical solution [41]. Verification of numerical solution is explained in appendix A.

After convergence to the steady-state concentration profile $c_{ss}\ (\vec{r})$, the corresponding flux vector $\vec{J}\ (\vec{r}) = -D\ (\vec{r})\vec{\nabla}c_{ss}\ (\vec{r})$, is calculated for every control volume. D_{eff} is then obtained by first performing

$$D_{eff} = \ell\langle\vec{J}\ (\vec{r})\rangle.\hat{y} \qquad (3\text{-}2)$$

where the angle brackets denote an average over the area of the system [53].

We will consider here two prototypical microstructures, namely a series of parallel boundaries and a polycrystal comprising Voronoi grains. These two characteristic structures are shown in Fig.'s 3-2a and 3-2b, respectively. The former structure is consistent with parallel transport and will be discussed in Sec. IV. The microstructure shown in Fig. 3-2b was generated from a centroidal Voronoi tessellation (CVT) algorithm comprising 100 generators [54].

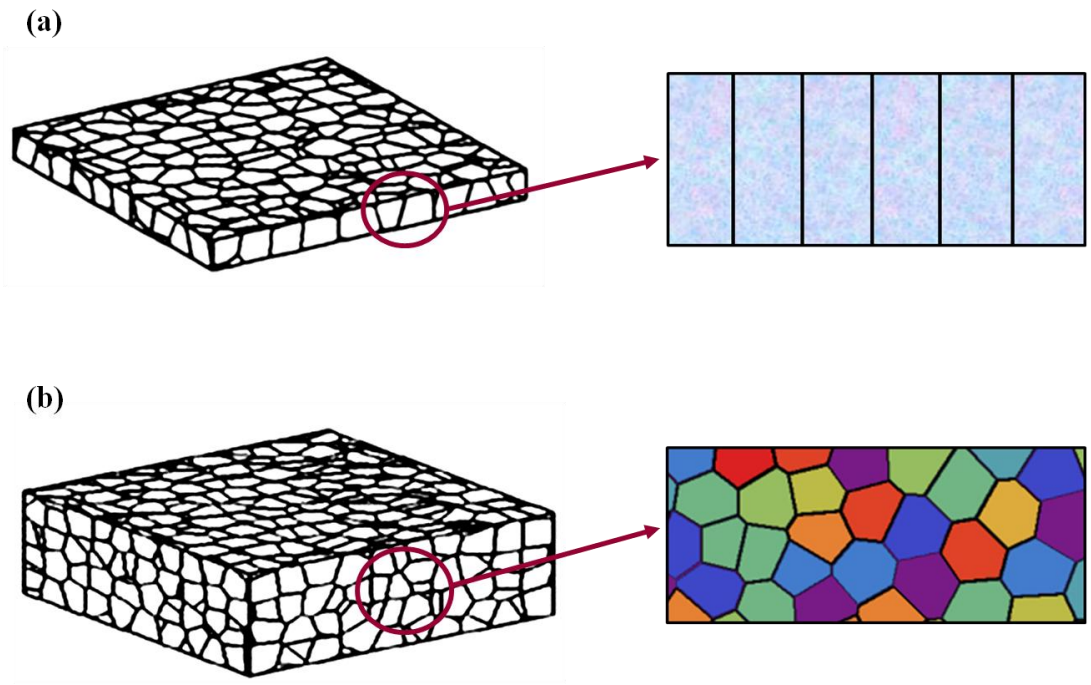

3-2 Two prototypical microstructures used to calculated an effective diffusivity, D_{eff} [55]. a.) A parallel arrangement of grain boundaries (shown in black). In general, each boundary has a different diffusivity and b.) a Voronoi microstructure resulting from randomly distributed generators.

By contrast with the standard Voronoi tessellation based on randomly distributed generators, the CVT is constructed from generators that are the mass centroids of the resulting grains. Consequently, the CVT algorithm leads to a more uniform distribution of nearly-equiaxed grains. In our discretized representation, the grain boundaries of this microstructure are matched with a group of lattice sites such that neighboring control volumes share at least one side. Moreover, grain boundaries are assigned widths of at most three control volumes. To obtain statistically meaningful results, $D_{eff}(T)$ at a temperature T is averaged over approximately 50 independent microstructures, each having the same number of generators. Finally, the corresponding effective activation energy is obtained by differentiation from the relation $Q_{eff}\,(T) = -k_B\,\partial\, ln\,(D_{eff}\,)/\,\partial\,(1/T\,)$.

3.4 Polycrystalline Mass Transport

As indicated above, mass transport in polycrystals is a complex phenomenon owing to several factors, including the variability of GB activation energies and the connectivity of the GB network. The interplay between these factors determines the effective diffusivity of the system and its dependence on temperature, stress, etc. In this section we first outline two descriptions of boundary kinetics in terms of the probability density of the boundary activation energy. While these models are necessarily idealized, a connection will be made with experimental data. We next highlight two prototypical microstructural models that constitute a collection of interconnected, fast diffusive pathways contained in a bulk region. For these models we obtain approximate analytical expressions for the effective diffusivity. In the Results section, we determine $D_{eff}(T)$ for the two prototypical microstructures using the aforementioned kinetic models to describe the distribution of activation energies.

3.4.1 Variability of Activation Energies

As noted above, in most treatments of GB diffusion in polycrystals one makes the simplifying assumption that all boundaries have the same diffusivity and, hence, identical activation energies for diffusion [8, 9], While this assumption makes subsequent analyses tractable, in reality there is a distribution of GB character, and therefore a spectrum of diffusivities and associated activation energies, $Q_{GB}^{i}\,(i = 1, 2, \ldots N_0)$, for the N_0 grain boundaries comprising a given microstructure. Thus, it is useful to regard the activation

energy for diffusion, Q, as a continuous random variable with a corresponding density of states, $N\ (Q)$, and an associated probability density function, $p\ (Q)$.

3.4.1.1 Discrete Model

A discrete model of microstructural kinetics having n GB activation energies and a Lattice (L) activation energy, Q_L, would take the form

$$p\ (Q) = f_L \delta(Q - Q_L) + \sum_i^n f_i\, \delta\left(Q - Q_{GB}^i\right) \qquad (3\text{-}3)$$

where f_i is the volume fraction of GB sites, f_L is the volume fraction of lattice and $\delta(Q)$ is the Dirac delta function. These volume fraction variables obey the constraint $f_L + \sum_i^n f_i = 1$. This simplified kinetic model will be considered in some detail below.

3.4.1.2 Continuous Model

A more realistic, continuous model for GB diffusion must account for the microstructural complexity of a polycrystal. Consider the distribution of GB energy, for a ferritic steel, as obtained by Beladi and Rohrer [56], shown in Fig. 3-3. In the following development we will neglect, to a first approximation, the temperature dependence of γ.

One can approximate the logarithmic dependence of boundary population on γ shown in the figure by defining a GB population, $N(\gamma)$, such that the associated population density

$$\bar{p}(\gamma) = \frac{\bar{N}(\gamma)}{\int_{\gamma_{min}}^{\gamma_{max}} d\gamma \bar{N}(\gamma)} = b.exp(-\alpha\gamma) \qquad (3\text{-}4)$$

where α is the (temperature-dependent) slope of the plot, b is a constant and $\gamma_{min}(\gamma_{max})$ is the minimum (maximum) GB energy in the range considered. Proper normalization of this density leads to

$$\bar{p}(\gamma) = \frac{\bar{N}(\gamma)}{N_0} = \left[\frac{1}{\exp(-\alpha\gamma_{min}) - \exp(-\alpha\gamma_{max})}\right] exp(-\alpha\gamma) \qquad (3\text{-}5)$$

where the total number of $N_0 = \int_{\gamma_{min}}^{\gamma_{max}} d\gamma \bar{N}(\gamma)$.

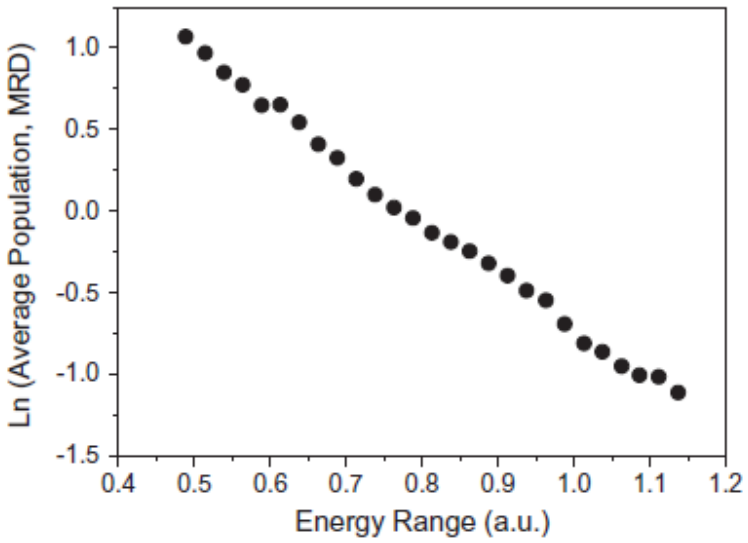

3-3 The logarithm of the number of grain boundaries as a function of GB energy, , for a ferritic steel, as obtained by Beladi and Rohrer [56].

The distribution of GB energies can be related to the distribution of GB activation energies for diffusion by employing an empirical relation due to Borisov that relates γ to Q_{GB} at a temperature T[57-60]. This relation can be written conveniently as,

$$\gamma = \left(\frac{1}{2a^2}\right)\left[k_B T \ln\left(\frac{D_{0GB}}{D_{0L}}\right) + (Q_L - Q_{GB})\right] \qquad (3\text{-}6)$$

where a is the average atomic distance and $D_{0GB}(D_{0L})$ is the diffusional prefactor for a GB (the lattice). Given the Borisov relation, one can now perform a transformation of variables to obtain from Eq. (3-5) the expression

$$p\,(Q) = \left[\frac{kf}{\exp(kQ_{GB}^{max}) - \exp(kQ_{GB}^{min})}\right] exp(kQ)\Theta\left(\mathrm{Q} - Q_{GB}^{min}\right)\Theta(Q_{GB}^{max} - \mathrm{Q}) f_B \delta(Q - Q_L) \qquad (3\text{-}7)$$

Where f is the GB volume fraction, $k = \alpha/2a^2$, $\Theta(\mathrm{Q_{GB}})$ is a step function and

$$\begin{aligned} Q_{GB}^{max} &= -2a^2\gamma_{min} + k_B T \ln\left(\frac{D_{0GB}}{D_{0L}}\right) + Q_L \\ Q_{GB}^{min} &= -2a^2\gamma_{max} + k_B T \ln\left(\frac{D_{0GB}}{D_{0L}}\right) + Q_L \end{aligned} \qquad (3\text{-}8)$$

In section 3.6.3, we will calculate an effective diffusivity based on this relation as a function of $\Delta Q = Q_{GB}^{max} - Q_{GB}^{min}$.

3.4.2 Grain Boundary Network Connectivity

Given the probability density for Q, $p\,(Q)$, one can determine an approximate expression for the effective diffusivity, $D_{eff}(T)$, for a particular microstructure. As noted above, we will consider two cases here, namely a parallel arrangement of boundaries and a CVT microstructure constructed from a collection of distributed generators. These prototypical microstructures are shown in Fig.'s 3-2a and 3-2b, respectively.

3.4.2.1 Independent, Parallel Grain Boundaries

To a good approximation the diffusion kinetics associated with the microstructure in Fig.3-2a is describable in terms of parallel transport processes. This approximation is valid to the extent that the different boundary regions are kinetically independent and, hence, when the boundary diffusivities are much greater than the lattice diffusivity. Thus, for a common prefactor, D_0, one may write that [61,62]

$$D_{eff}(T) = \frac{D_0}{N_0}\int_0^\infty dQ\; N(Q)\exp\left(-\frac{Q}{k_B T}\right) \qquad (3\text{-}9)$$

And identify corresponding effective activation energy

$$Q_{eff}(T) = \frac{\int_0^\infty dQ\; QN(Q)\exp\left(-\frac{Q}{k_B T}\right)}{\int_0^\infty dQ\; N(Q)\exp\left(-\frac{Q}{k_B T}\right)} \qquad (3\text{-}10)$$

In this regard $D_{eff}(T)$ is analogous to the classical partition function in statistical mechanics [63], an analogy that will be exploited further below.

3.4.2.2 Centroidal Voronoi Microstructure

For the case of the centroidal Voronoi microstructure shown in Fig. 2b, it is useful to obtain analytically an approximate value for D_{eff} . For this purpose, one can regard this system as a composite medium comprising elements having different kinetic properties. As such, there are several approaches that can be taken to determine D_{eff} , including the establishment of rigorous bounds [64,65] and the use of a Maxwell-Garnett effective-medium artifice [66, 67]. Following the Maxwell-Garnett approach as applied to mass transport [68], an approximation for D_{eff} can be obtained as follows. For a system with a single GB diffusivity D_{GB}, one can approximate the medium as a collection of lattice (grain interior) regions embedded in a GB matrix (see Fig. 3-4).

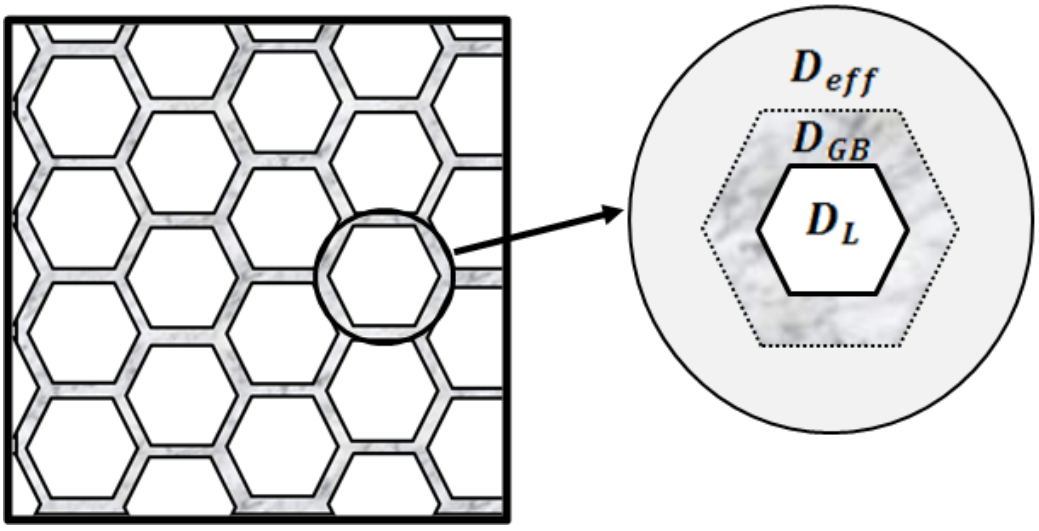

3-4 A schematic of an idealized microstructure showing the geometry associated with the Maxwell-Garnett calculation of D_{eff} .

This assignment of regions is necessary to create a series of spatially compact domains surrounded by a common matrix. By solving for the steady-state concentration

fields in the lattice, grain boundary and embedded medium, one obtains, in two dimensions,

$$D_{eff} = D_{GB}\left[1 + \frac{2(1-f)(D_L - D_{GB})}{D_L + D_{GB} - (1-f)(D_L - D_{GB})}\right] \qquad (3\text{-}11)$$

For systems having more than one GB diffusivity, one can take the same approach described above, except that one must define D_{GB} to reflect the spectrum of GB diffusivities. Two prescriptions were employed here. The first prescription assumes that there is a mixture of GB diffusivities outside the percolation regime. Following Kirkpatrick [67], one finds, for a square lattice, that

$$\int dD'_{GB} \frac{D'_{GB} - D_{GB}}{D'_{GB} + D_{GB}} p(D'_{GB}) = 0 \qquad (3\text{-}12)$$

where $p(D'_{GB})$ is the probability density function for the GB diffusivity. The second prescription, also known as Hart approach [65], assumes that the GB diffusivities can be combined independently . Thus, for two GB diffusivities,

$$D_{GB}(T) = \left[f_1 D_{0GB}^{(1)} \exp\left(-\frac{Q_{GB}^{(1)}}{k_B T}\right) + f_2 D_{0GB}^{2} \exp\left(-\frac{Q_{GB}^{(2)}}{k_B T}\right)\right] \qquad (3\text{-}13)$$

where D_{0GB}^{1} and D_{0GB}^{2} are the diffusional prefactors for the two boundaries. Both prescriptions will be used to interpret our results, as described below.

3.5 Analytical Results: Parallel Boundaries

We first examine the case of diffusion in a system comprising parallel grain boundaries, as shown in Fig. 3-2a. As noted above, in the limit that the GB diffusivities are much larger than the lattice diffusivity, the boundaries constitute nearly independent, fast diffusive pathways. Thus, in this limit, we can calculate D_{eff} directly from Eq.(3-9) without appealing to numerical methods.

3.5.1 Two Boundary Types – Discrete Model

For this case, consider two distinct GB boundary types, with corresponding activation energies $Q_{GB}^{(1)}$ and $Q_{GB}^{(2)}$ and volume fractions f_1 and f_2. The effective diffusivity, found using Eq. (3-3), is

$$D_{eff}(T) = D_0 \left[f_L \exp\left(-\frac{Q_L}{k_B T}\right) + f_1 \exp\left(-\frac{Q_{GB}^{(1)}}{k_B T}\right) + f_2 \exp\left(-\frac{Q_{GB}^{(2)}}{k_B T}\right) \right] \quad (3\text{-}14)$$

Figure 3-5a shows the dependence of the logarithm of $D_{eff}(T)$ on $1/T$ for the case of two distinct boundaries with coefficients given by $f_L = 0.5$, $f_1 = 0.05$ and $f_2 = 0.45$ and corresponding activation energies $Q_L = 1.0$, $Q_{GB}^{(1)} = 0.1$ and $Q_{GB}^{(2)} = 0.35$ (in units of eV). For this parameter set, there are broadly two diffusive regimes, as determined by the relative activation energies and the relative volume fraction of sites. This behavior is characteristic of kinetic quantities in systems having different activation energies, such as the electrical conductivity of an extrinsic semiconductor [69]. The effective activation energy is displayed in Fig. 3-5b. It is evident that there are two

regimes characterized by different activation energies. In Fig. 3-5c the temperature derivative $C = dQ_{eff}/dT$ is shown as a function of T. This quantity plays a role analogous to the heat capacity in statistical physics, and exhibits a "Schottky" peak that is characteristic of multi-level systems. Indeed, from the location of this peak one can define a transition temperature separating the two kinetic regimes. More generally, the shape of this peak embodies information about the spectrum of activation energies that characterizes this system.

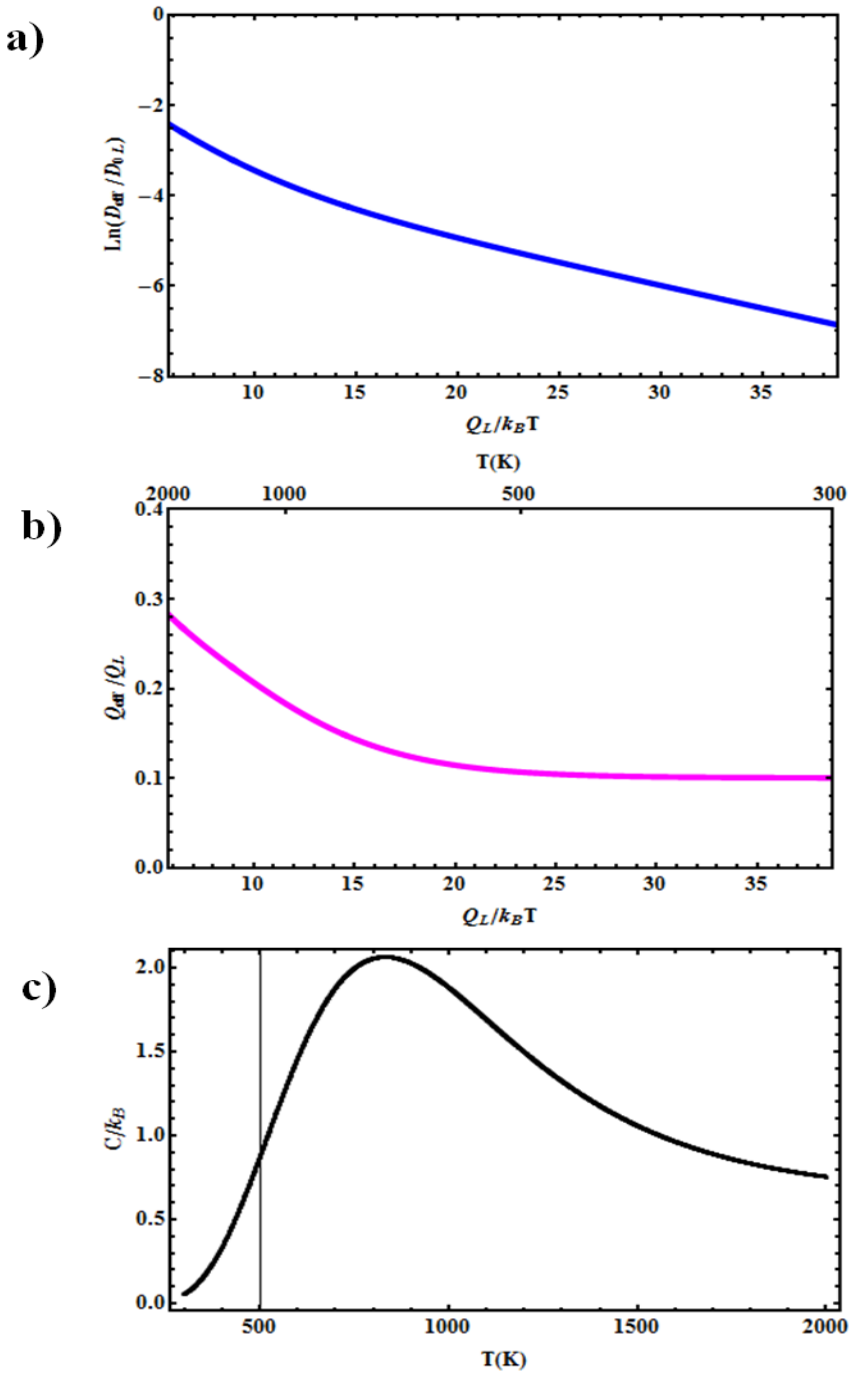

Figure 3-5 a.) The logarithm of $D_{eff}\ (T)\ /D_{0L}$ on inverse temperature, $\Delta Q/k_BT$, for the case of two distinct boundaries with volume fractions given by $f_L = 0.5$, $f_1 = 0.05$ and $f_2 = 0.45$ and corresponding activation energies $Q_L = 1.0$, $Q_{GB}^{(1)} = 0.1$ and $Q_{GB}^{(2)} = 0.35$ (in units of eV). b.) The effective activation energy, Q_{eff}/Q_L, versus inverse temperature, Q_L/k_BT, for this case. c.) The quantity $C = dQ_{eff}/dT$ versus temperature, T. Note the peak that is characteristic of multi-state systems.

3.5.1 Continuous Distribution of Activation Energies

More generally, for the continuous distribution of activation energies given in Eq. (3-7), one can calculate D_{eff} using Eq. (3-9). Upon substituting Eq. (3-7) into Eq. (3-9) one obtains

$$D_{eff}(T) = D_0 \left[\left(\frac{f\gamma}{\gamma-\epsilon}\right)\left[\frac{\exp(\gamma-\epsilon)-1}{\exp(\gamma)-1}\right]\exp(-\epsilon\bar{Q}_{GB}) + f_L\exp\left(-\epsilon\bar{Q}_{GB}\right)\right] \quad (3\text{-}15)$$

where the dimensionless parameters $\sigma = k\Delta Q$, $\epsilon = \Delta Q/k_BT$, $\bar{Q}_{GB} = Q_{GB}^{min}/\Delta Q$ and $\bar{Q}_L = Q_L/\Delta Q$. Nicholas found a similar expression for an effective reaction rate when considering the problem of parallel activated processes involving multiple catalytic sites [26]. Before examining the corresponding $Q_{eff}(T)$, it is useful to obtain first the normalized, relative activation energy, calculated using Eq. (3-15), in the somewhat artificial, boundary-dominated limit $f_L/f_1 \rightarrow 0$. One finds that

$$\bar{Q}_{eff} = \frac{Q_{eff}-Q_{eff}^{min}}{\Delta Q} \rightarrow \frac{1}{\epsilon-\gamma} + \frac{1}{1-\exp(\epsilon-\gamma)} \quad (3\text{-}16)$$

In the zero-temperature limit ($\epsilon \rightarrow \infty$) $\bar{Q}_{eff} \rightarrow 0$ for γ finite, while in the high-temperature limit ($\epsilon \rightarrow 0$) $\bar{Q}_{eff} \rightarrow \frac{1}{2}$ as $\gamma \rightarrow 0$ and $\bar{Q}_{eff} \rightarrow 1$ as $\gamma \rightarrow \infty$. Thus, if there is little variability in the distribution of GB activation energies over a range of width ΔQ, Q_{eff} increases by an amount approximately equal to the average of Q_{GB}^{max} and Q_{GB}^{min} at high temperatures. If, however, there is substantial variability in the distribution of activation energies, then Q_{eff} varies over the full range from Q_{GB}^{min} to Q_{GB}^{max} as the temperature increases.

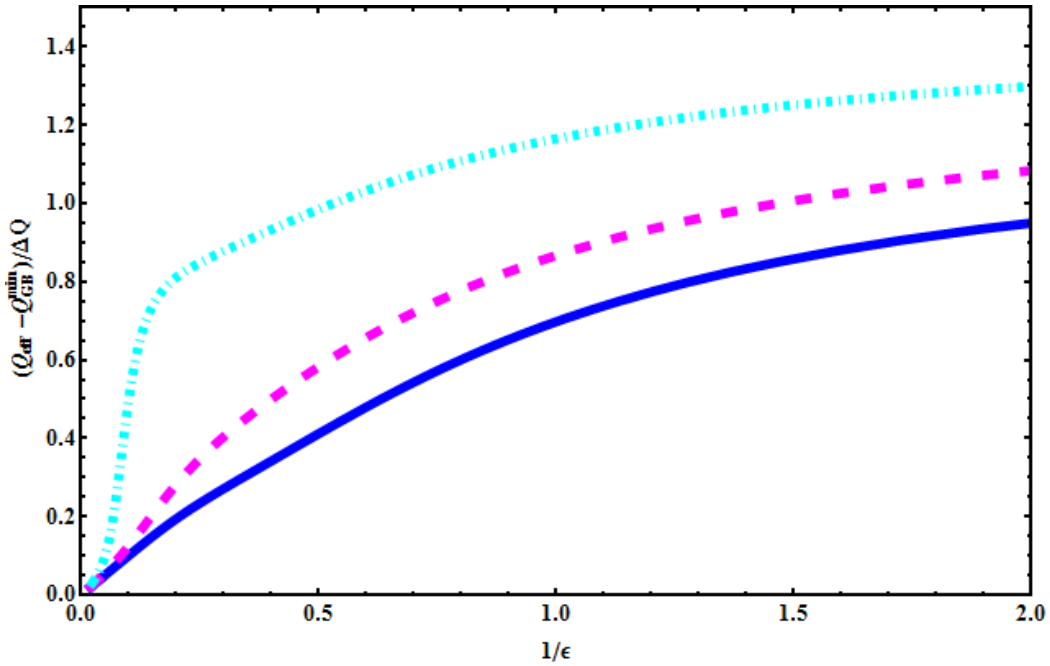

Figure 3-6 The dependence of the normalized, effective activation energy $\bar{Q}_{eff} = (Q_{eff} - Q_{GB}^{min})/\Delta Q$ on $\epsilon = \Delta Q/k_B T$ for $\gamma = 0.01$ (solid line), 2.0 (dashed line) and 10.0 (dot-dashed line). The ratio of lattice to GB volume fractions is $f_L/f_1 = 1$, and the normalized lattice activation energy $\bar{Q}_L = 3.0$.

In most cases, the behavior outlined above is masked by lattice diffusion due to the high volume fraction of lattice sites. At nanocrystalline length scales, however, where the volume fraction of grain boundaries can be 50% [70], one expects a competition between GB and lattice diffusion. Figure 3-6 shows the dependence of $\bar{Q}_{eff}$ on ϵ (temperature) for three different values of γ for the case that $f_L/f_1 = 1$ and a normalized lattice activation energy $\bar{Q}_L = 3.0$. As expected, at high temperatures $\bar{Q}_{eff}$ saturates at a value somewhat above that in the boundary-limited case since lattice diffusion is operative at these temperatures.

3.6 Simulation results: CVT microstructure

For the case of a CVT, as shown in Fig. 3-2b, we obtain D_{eff} by numerical solution of the steady state diffusion equation, as described above. For this microstructure, we investigate the transport behavior for three different scenarios, namely: 1.) two types of boundaries (i.e., boundaries having different activation energies and prefactors), 2.) a system undergoing a complexion transition in which a fraction of the boundaries transforms at a temperature T_t, and 3.) Boundaries having a spectrum of activation energies distributed according to Eq. (3-7). Rather than explore a wide range of parameter space, we focus here on a few illustrative cases that exhibit different diffusive regimes.

3.6.1 Two Boundary Types – Discrete Model

In this scenario two *distinct* grain boundary types, with diffusivities described by different activation energies and prefactors, comprise the microstructure. The goal here is to investigate the role of boundary type in determining the effective diffusivity. We consider two parameter sets, as summarized in Table 3-1. The first set corresponds to a typical situation in which grain boundaries constitute high-diffusivity paths (with relatively low associated activation energies) relative to the lattice owing to their relatively open structure. By contrast, the second set corresponds to a scenario in which the GB activation energies exceed that of the lattice. While this situation may be somewhat counterintuitive as it does not occur in metals, larger activation energies for GB diffusion have been reported for some ceramic systems [71]. For this latter case, the

effective diffusivity is dominated by grain boundaries at high temperatures while, for low temperatures, lattice diffusion is dominant.

Table 1. A summary of the kinetic parameters for the two cases comprising Scenario 1. The total volume fraction of boundary sites is 0.105 with approximately 40% of the boundaries being type 1.

	Case I	**Case II**
$\boldsymbol{Q_{GB}^{(1)}/Q_L}$	0.3	1.5
$\boldsymbol{Q_{GB}^{(2)}/Q_L}$	0.7	1.25
$\boldsymbol{D_{0GB}^{(1)}/D_{0GB}^{(2)}}$	0.0001	100

For the first case, Fig. 7a shows the dependence of $D_{eff}(T)$ on inverse temperature as obtained from numerical solution of the steady-state diffusion equation and from two implementations of effective medium theory. Figure 7b shows the dependence of the associated effective activation energy, $\bar{Q}_{eff}(T)$, on temperature, T. More specifically, D_{GB} is calculated in two different ways, using either the Kirkpatrick (see Eq. 3-12) or the Hart (see Eq. 3-13) approach. D_{eff} is then obtained for each case by substituting D_{GB} into Eq. (3-11). As is evident from Fig. 3-7a, at high temperatures both implementations reproduce the numerical data well while, at low temperatures, the use of Eq. (3-13) in the effective medium approximation is superior. Moreover, the temperature dependence of $\bar{Q}_{eff}(T)$ highlights two diffusive regimes with a kinetic transition temperature at $T_t = 600K$. The low-temperature regime is dominated, as expected, by the grain boundaries.

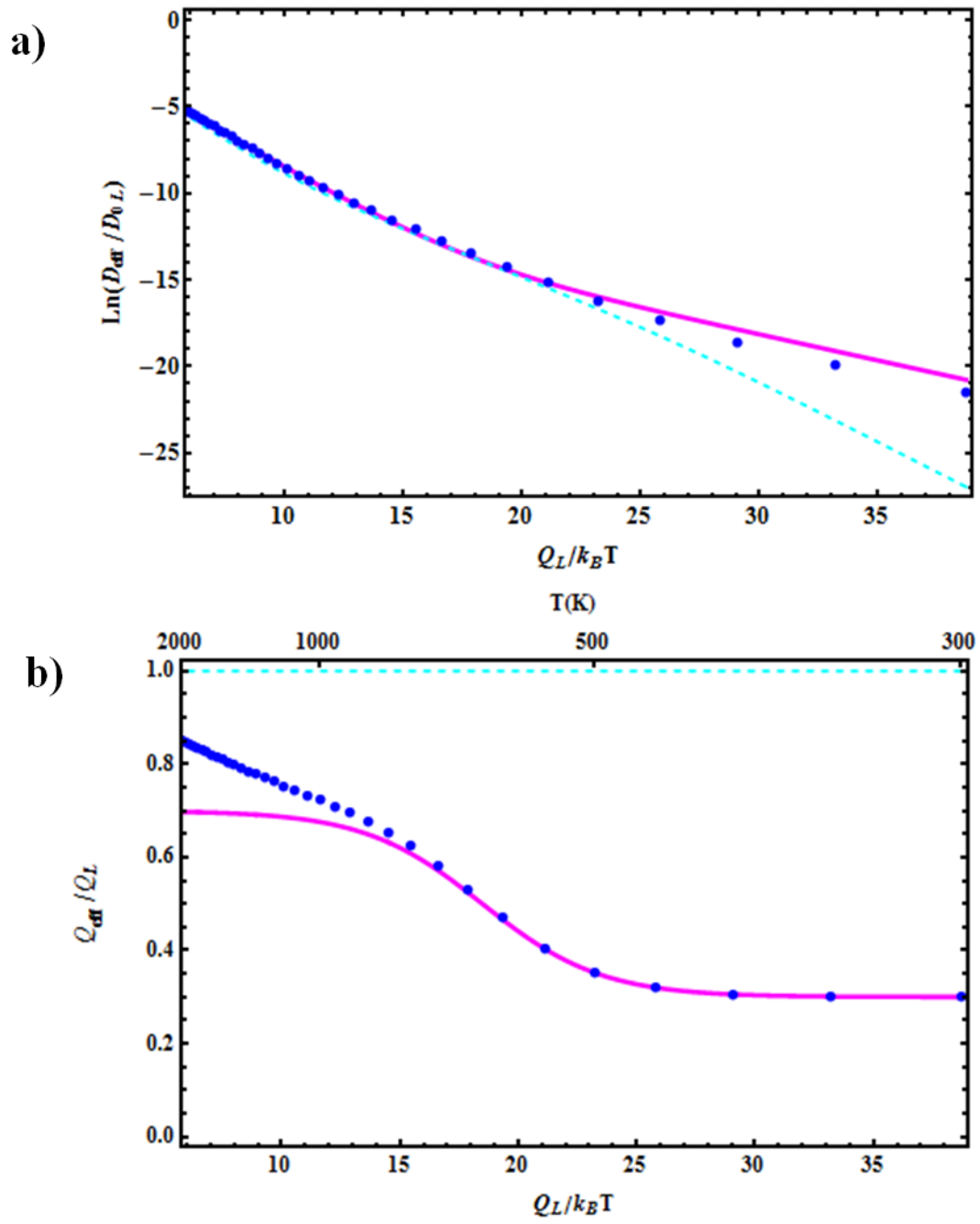

Figure 3-7 a.) The dependence of the logarithm of the effective diffusivity, $D_{eff}(T)/D_{0L}$, on inverse temperature, Q_L/k_BT, for Case I (Scenario 1) as determined by the solution of the steady-state diffusion equation (circles) and from the Kirkpatrick (dashed line) and Hart (solid line) effective medium theories. b.) The associated effective activation energy Q_{eff}/Q_L as a function of temperature, T (circles). Also shown is the GB contribution to Q_{eff}, calculated using the Hart approach (solid line), and the lattice contribution to Q_{eff} (dotted line). Note that there are, broadly speaking, two distinct diffusive regimes.

Case II corresponds to a scenario in which the GB activation energies exceed that of the lattice. While this situation may be somewhat counterintuitive as it does not occur in metals, larger activation energies for GB diffusion have been reported for some ceramic systems [71]. For this case, Fig. 3-8a shows the dependence of $D_{eff}(T)$ on inverse temperature as obtained from numerical solution of the steady-state diffusion equation, by the Maxwell-Garnett effective medium theory (with the Hart approach) and by a hybrid approach described below. The use of the standard Maxwell-Garnett effective medium theory is not wholly adequate here, as indicated in the figure. The reason for this inadequacy is that the large volume fraction of lattice sites employed here and the higher lattice diffusivity implies that the lattice phase, rather than the grain boundaries, should be considered as the matrix phase at low temperature. Thus, one can apply the Maxwell-Garnett approach as before in the high-temperature regime while, in the low-temperature regime, one should interchange the roles of GB and lattice. The resulting, hybrid effective medium theory is seen to reproduce the data well over the wide range of temperatures considered here. Figure 3-8b shows the dependence of the associated effective activation energy, $\bar{Q}_{eff}(T)$, on temperature. It should be noted that, by contrast with the previous case, the low-temperature regime is dominated by lattice kinetics while the high-temperature regime reflects grain-boundary kinetics.

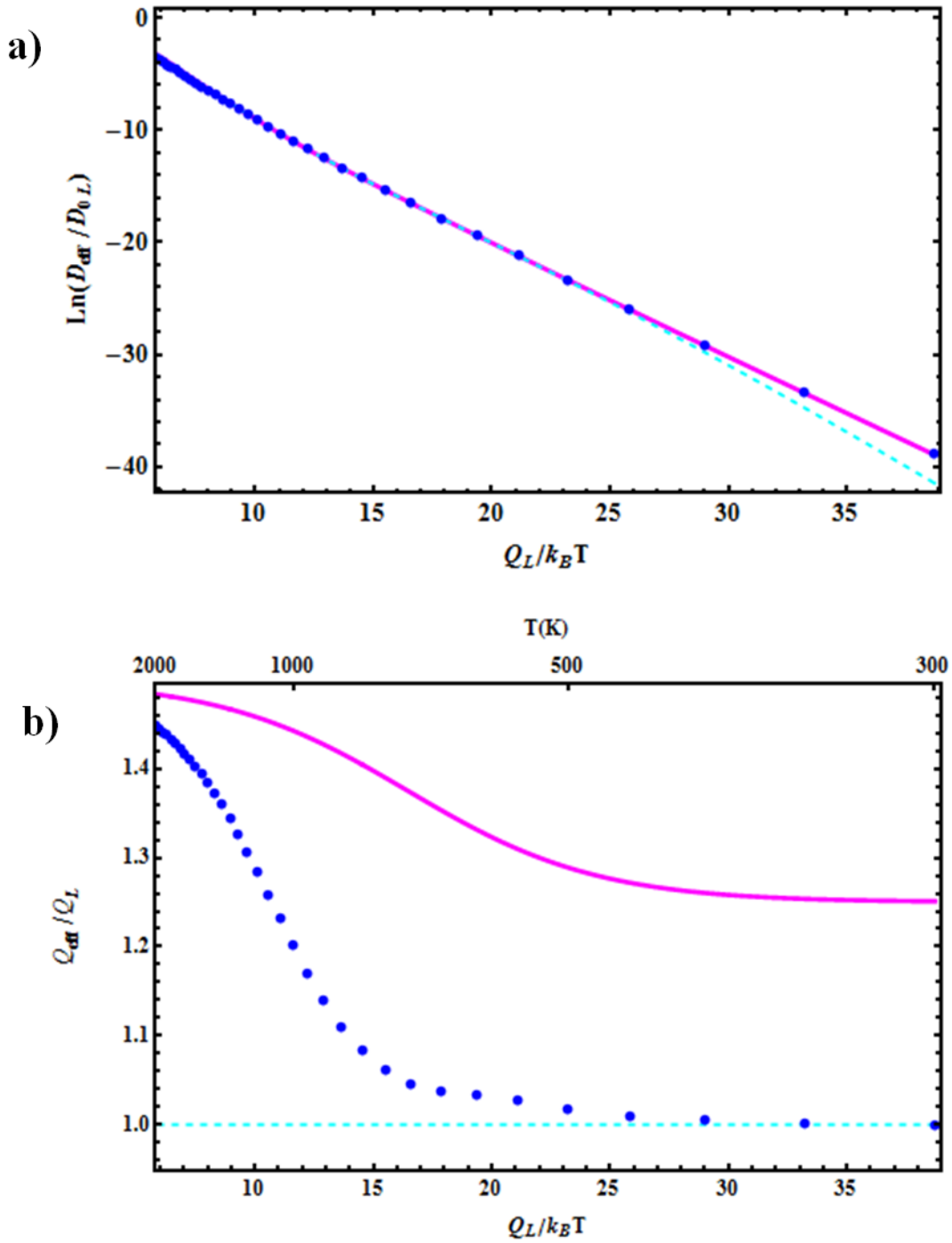

Figure 3-8 a.) The dependence of the logarithm of the effective diffusivity, $D_{eff}(T)/D_{0L}$,, on inverse temperature, Q_L/k_BT, for Case II (Scenario 1) as determined by the solution of the steady-state diffusion equation (circles). Also shown are the results of the hybrid effective medium theory (solid line) and the conventional Maxwell-Garnett approach (dashed line). b.) The associated effective activation energy Q_{eff}/Q_L as a function of temperature, T (circles). Also shown is the GB contribution to Q_{eff}, calculated using the Hart approach (solid line), and the lattice contribution to Q_{eff} (dotted line).

3.6.2 Complexion Transition – Discrete Model

In this scenario a fraction of the boundaries undergo a complexion transition as a function of temperature. As discussed above, such complexion transitions involve structural and chemical changes at a boundary, and therefore have implications for boundary kinetics [46]. Previous studies have led to the identification of a series of complexion types and the realization that property changes, such as changes in GB mobility or embrittlement [72], are associated with complexion transitions [73]. In this case, it is assumed that changes in GB diffusion attend these structural and chemical changes at interfaces. For simplicity, we again consider two distinct GB types having the parameter set summarized in Table 3-2. For temperatures below T_t this set corresponds to that for Case I of Scenario 1. To model a complexion transition, it is assumed that a transition occurs at a temperature $T_t = 700K$, and that there is an associated change in the diffusional prefactor corresponding to one of the grain boundaries.

Table 2 A summary of the kinetic parameters for Scenario 2. The total volume fraction of boundary sites is 0.105 with approximately 40% of the boundaries being type 1. The complexion transition temperature is $T_t = 700K$

	GB1	**GB2**
$\boldsymbol{Q_{GB}/Q_L}$	0.3	0.7
$\boldsymbol{D_{0GB}/D_{0L}}$	0.0005	$5.0(T < T_t)$ $50.0(T \geq T_t)$

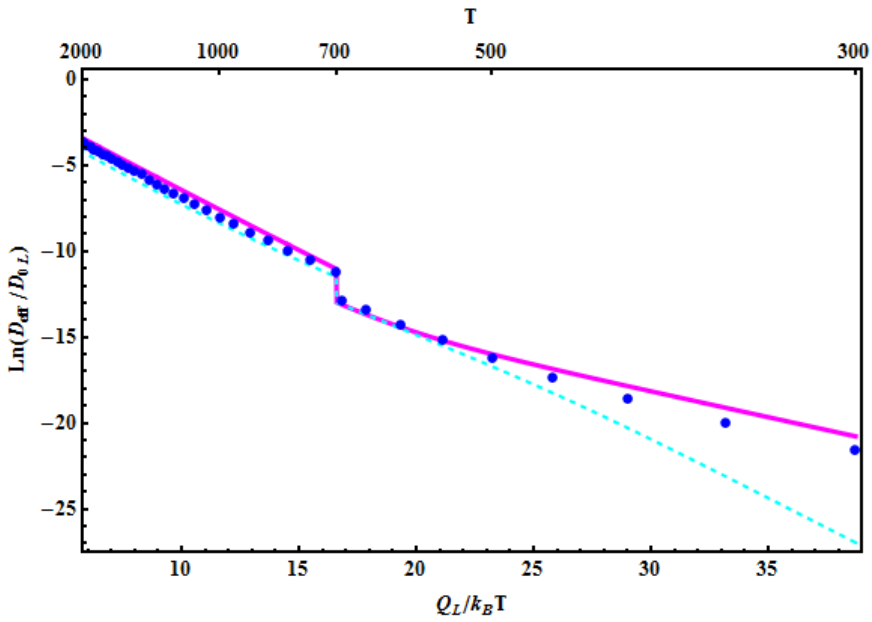

Figure 3-9 The dependence of the logarithm of the effective diffusivity, $D_{eff}(T)/D_{0L}$, on inverse temperature, Q_L/k_BT, for Scenario 2; Complexion transition as determined by the solution of the steady-state diffusion equation (circles) and from the Kirkpatrick (dashed line) and Hart (solid line) effective medium theories.

Figure 3-9 displays the dependence of $D_{eff}(T)$ on inverse temperature as obtained from numerical solution of the steady-state diffusion equation and, in addition, as calculated using both the Kirkpatrick and the Hart effective medium theories. As is evident from the figure, the Hart approach again captures the diffusive response over a wide range of temperatures. Moreover, there is a jump in the value of D_{eff} due to a change in a GB diffusional prefactor at T_t. This jump in the effective diffusivity translates into an increase in Q_{eff} at the same temperature. Thus, one must be careful in the interpretation of such plots to determine whether a change in Q_{eff} is due to a change in activation barriers or, as in this scenario, a change in attempt frequencies (i.e., prefactors). More generally, one would expect that different boundary types would have

one or more different complexion transition temperatures, and so the sharp jump evident in Fig. 3-9 would be replaced by a smoother transition.

3.6.3 Continuous Distribution of Activation Energies

In this scenario the activation energy for a given boundary is drawn from the distribution of activation energies given in Eq. (3-7). To draw from this distribution, one generates a uniform deviate and, from the logarithm of this deviate, obtains the desired exponentially distributed random variable [70]. The diffusivities obtained in this manner are then randomly assigned to the grain boundaries in the system. For this distribution of activation energies, we performed several simulations for different values of ΔQ at a fixed value of $k = 3.0\, eV^{-1}$. This value of k was determined from the slope of the plot in Fig. 3-3, assuming that a typical value for the maximum γ is about $1.0\, J/m^2$.

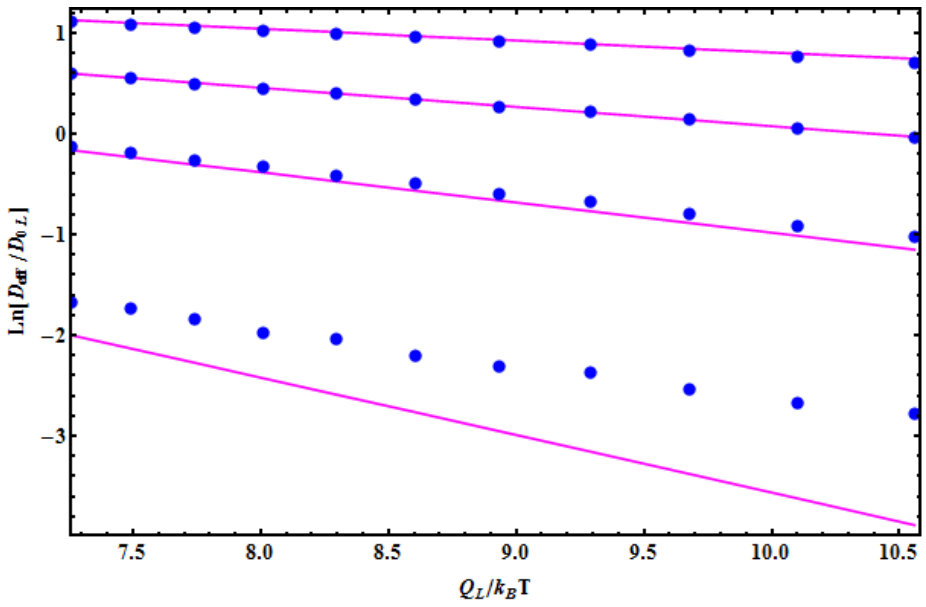

3-10 The logarithm of $D_{eff}\,(T)\,/D_{0L}$ as a function of $\Delta Q/k_BT$ for various values of σ for a continuous distribution of GB activation energies. The solid lines represent the simulation results and the dashed lines are calculated using effective medium theory. The values of γ from top to bottom are $\sigma = 0.1, 0.5, 1.0\ and\ 2.0$

The results from the aforementioned simulations are displayed in Fig. 3-10, which shows $ln\,(D_{eff}/D_{0L})$ as a function of Q_L/k_BT for several different values of $\sigma = k\Delta Q$. Also shown are the predictions of effective medium theory, obtained by using Eq. (3-12) to calculate D_{GB} for use in Eq. (3-11). As can be seen from the figure, effective medium theory reproduces much of the simulation data, especially at small ΔQ. This agreement for small is intuitively reasonable since the effective medium approximation should work best for single activation energy or, in general, for a very narrow range of activation energies.

3.7 Conclusion

In this work we employed both analytical and numerical methods to examine the impact of GB variability (i.e., a spectrum of boundary activation energies) on diffusion in a polycrystal [74]. In particular, we calculated an effective diffusivity, D_{eff}, and associated activation energy, Q_{eff} , as a function of temperature for different microstructures using simplified, multi-state models and models based on experimentally obtained GB energy distributions. The main conclusions of this study are as follows.

1. The variability in polycrystalline GB character leads, via the Borisov relation, to a probability density for GB activation energies and an associated effective diffusivity that can be characterized by a few parameters.

2. From the effective diffusivity one can obtain temperature dependent effective activation energy. From this activation energy, one can identify different diffusive regimes and transition temperatures.

3. Effective medium theory can be generalized to incorporate both lattice and multiple GB diffusivities. This theory describes the effective diffusivity in some polycrystalline systems over a wide range of temperatures.

4. Complexion transitions affect the spectrum of GB activation energies, and one can assess their impact on GB diffusion using the numerical procedure described above.

4.

HYBRID ATOMISTIC SIMULATION OF FLUID UPTAKE IN A DEFORMABLE SOLID

4.1 Introduction

The behavior of a matrix under fluid infiltration is of significance for designing new materials in various applications ranging from analytical separations to drug delivery. For a compliant matrix, the distortion that attends fluid uptake can lead, for example, to swelling in polymeric systems and concomitant non-Fickian diffusive behavior [24-26]. For the particular case in which the fluid permeates a porous solid and generates stresses that couple with the fluid concentration field, the resulting poroelastic response can alter the kinetic and structural response of the system [76,77]. While the

conceptual framework for poroelasticity was developed in the early work of Biot [78], the field remains active given the technological relevance of this phenomenon.

Several approaches exist for modeling fluid imbibition in a system. For example, Gelb and Hopkins [34] used molecular dynamics simulation to study the dynamics of fluid flow into empty cylindrical pores in which the pore-wall atoms were immobile. Ahadian *et al.* subsequently simulated imbibition of a simple fluid into a nanochannel using atomistic simulation to investigate the wall-fluid interaction [35]. More recently, Joly [36] employed molecular dynamics (MD) simulation to examine water uptake by a carbon nanotube, and Stukan *et al.* [37] also used MD to investigate the role of nanopore roughness on fluid imbibition. As in the work of Gelb and Hopkins [34], the atoms comprising the pore walls were static. At longer length scales, a phase-field model was developed to investigate fluid infiltration in a weakly anisotropic, poroelastic solid. It was found that imbibition depended on the strength of the anisotropy and the relative orientation of the propagating fluid front [79,80].

4.2 Objectives

Given the inherent computational demands of simulating fluid imbibition at the atomic scale, most such simulations of this process take the matrix atoms to be immobile. This assumption is often justified, especially for fluid atoms having small radii, in situations where elastic energy considerations are relatively unimportant. The modeling of elastic deformation that attends fluid uptakes necessitates, however, the incorporation of matrix stresses via the inclusion of matrix-atom coordinates. As an illustration of a simple system that exhibits coupling between diffusional and elastic fields, we explore in this study the impact of elastic deformation, as described by a compositional strain, on fluid uptake in a face-centered cubic solid that is in contact with a reservoir. Our aim is to explore the consequences of this coupling on the elastic response of the solid and the diffusional transport of the permeating fluid. For this purpose, we have tailored a hybrid MonteCarlo–molecular dynamics scheme to model fluid uptake in the solid from a reservoir that is maintained at a constant chemical potential for the fluid species. In particular, a grand-canonical Monte Carlo (GCMC) simulation is employed to maintain a fixed chemical potential in a reservoir of fluid atoms that is in contact with a solid. The trajectories of both fluid and solid atoms in the solid are obtained using MD simulation. By monitoring the fluid uptake, as well as the instantaneous structure factor and lattice parameter for the solid, we develop a description of fluid permeation in a deformable medium.

4.3 Background

In the background section, we are going to review the concept of fluid uptake and compositional strain which have been both frequently addressed in this work. These two concepts play crucial roles in our analysis and brief explanation of them can help to follow the proposed analytical approach easier.

4.3.1 Fluid Uptake

Our analysis of fluid uptake, $M(t)$, at time t begins with a comparison to ideal, Fickian imbibition, defined here as uptake following the standard diffusion equation with a *constant* diffusion coefficient, D. Consider a spatially uniform, solid slab confined to the region $-\ell \leq z \leq \ell$ having a diffusant concentration, $c\,(z,t)$, that is in contact with a diffusant (fluid) reservoir at its boundaries, $z = \pm\ell$. For the case in which $c\,(z,0) = 0$ in the slab and $c(\pm\ell, t) = c_0$, one finds that [81]

$$\frac{M_F(t)}{M_\infty} = 1 - \sum_{n=0}^{\infty} \frac{8}{(2n+1)^2\pi^2} exp\left(\frac{-D(2n+1)^2\pi^2 t}{4\ell^2}\right) \qquad (4\text{-}1)$$

where M_∞ is the uptake at saturation (i.e., $t = \infty$) and the superscript "*F*" denotes Fickian behavior (i.e., following from the standard diffusion equation).

Thus, systems characterized by the uptake function given by Eq. (4-1) are, by our definition, Fickian in nature, and we are especially interested here in characterizing any deviations from this behavior observed in our simulations. Such deviations may occur for

various reasons, including, for example, stress generation in the matrix and time-dependent structural changes (e.g., in polymers) [82,23]. In the context of this work, it is expected that the permeation of relatively large diffusant atoms in an elastic solid will generate stresses that will impede further diffusion. A link between the spatiotemporal evolution of $c\ (z,t\ )$ and generated self-stresses is described below.

4.3.2 Compositional strain

The diffusion of fluid atoms through the void space in a crystalline solid leads to self-stress, and therefore local strains, that depend on $c\ (z,t\ )$. If the reference state of the system is associated with a uniform concentration $\bar{c}$, then, in a cubic system, one can specify the components of the compositional strain tensor as $\epsilon_{ij}^{c} = \eta(c-\bar{c})\delta_{ij}$ [83] where η is the compositional strain parameter and δ_{ij} is the Kronecker delta. For small strain, the corresponding stress is proportional to the elastic strain and so, in the absence of an external stress,

$$\sigma_{ij} = C_{ijkl}(\epsilon_{kl} - \epsilon_{kl}^{c}) \qquad (4\text{-}2)$$

where σ_{ij} are the components of the stress tensor and C_{ijkl} are the components of the elastic constant tensor. Extended tensor for equation (4-2) can be written as

$$\begin{bmatrix}\sigma_{11}\\ \sigma_{22}\\ \sigma_{33}\\ \sigma_{23}\\ \sigma_{13}\\ \sigma_{12}\end{bmatrix} = \begin{bmatrix} 1-\nu & \nu & \nu & 0 & 0 & 0\\ \nu & 1-\nu & \nu & 0 & 0 & 0\\ \nu & \nu & 1-\nu & 0 & 0 & 0\\ 0 & 0 & 0 & \frac{(1-2\nu)}{2} & 0 & 0\\ 0 & 0 & 0 & 0 & \frac{(1-2\nu)}{2} & 0\\ 0 & 0 & 0 & 0 & 0 & \frac{(1-2\nu)}{2} \end{bmatrix} \frac{E}{(1+\nu)(1-2\nu)} \begin{bmatrix}\epsilon_{11}\\ \epsilon_{22}\\ \epsilon_{33}\\ 2\epsilon_{23}\\ 2\epsilon_{13}\\ 2\epsilon_{12}\end{bmatrix} - \frac{E\eta\Delta C}{1-2\nu}\begin{bmatrix}1\\1\\1\\0\\0\\0\end{bmatrix} \quad (4\text{-}3)$$

Here, E and ν are Young's modulus and Poisson's ratio and Δc is the increase in concentration of liquid into the solid. For a cubic solid one can readily obtain the pressure, P, in terms of the compositional strain. Taking the trace of both sides of Eq. (4-2) and noting that $P = -(1/3)\sigma_{ii}$ (with the summation convention), one finds that

$$P = B[3\eta(c - \bar{c}) - \epsilon_{ii}] \qquad (4\text{-}4)$$

where B is the bulk modulus. For cases in which the pressure in the reference state is nonzero, $B = B^0 + \frac{P}{3}$. Equation (4-4) can be used to determine the compositional strain in a simulation from knowledge of the bulk modulus of a material and its dimensional changes resulting from the permeation of a fluid. One aim of this paper is to relate M (t) to η.

4.4 Simulation Methodology

A hybrid Monte Carlo–molecular dynamics scheme was employed here to model the coupling of a fluid reservoir to a deformable solid. From a number of such approaches developed in recent years [84–87], we selected a methodology for this study that is an extension of an earlier scheme that is well suited to the study of fluid uptake [84].

4.4.1 Simulation Setup

Our simulations are based on a layered geometry wherein, initially, a face-centered cubic (fcc) solid slab comprising N_s atoms of radius R_s is in contact with a fluid "reservoir"[1] containing N_f atoms of radius R_f, as shown in Fig. 4-1(a). The system is subject to periodic boundary conditions in each principal direction. The chemical potential of the reservoir, μ_{res}, is held fixed using GCMC (see below), and so the number of fluid atoms in the reservoir fluctuates during the course of a simulation.

The interactions in this binary system are governed by a modified Lennard-Jones potential developed by Broughton and Gilmer [88]. The interatomic potential is given by

$$U^{\alpha\beta}(r) = \begin{cases} 4\varepsilon^{\alpha\beta}\left[\left(\frac{\sigma^{\alpha\beta}}{r}\right)^{12} - \left(\frac{\sigma^{\alpha\beta}}{r}\right)^{6}\right] + C_1, \; r \le 2.3\sigma^{\alpha\beta} \\ C_2\left(\frac{\sigma^{\alpha\beta}}{r}\right)^{12} + C_3\left(\frac{\sigma^{\alpha\beta}}{r}\right)^{6} + C_4\left(\frac{r}{\sigma^{\alpha\beta}}\right)^{2} + C_5, \; 2.3\sigma^{\alpha\beta} < r < 2.5\sigma^{\alpha\beta} \\ 0, \; r \ge 2.5\sigma^{\alpha\beta} \end{cases} \quad (4\text{-}5)$$

[1] In this context, the reservoir has a finite extent. It is connected, via a GCMC scheme, to a particle reservoir that maintains its chemical potential.

where $\varepsilon^{\alpha\beta}$ and $\sigma^{\alpha\beta}$ are the usual energy and length parameters, respectively, and α and β denote atom types (i.e., solid or fluid)[2]. The energy and length parameters were calculated using the Lorentz-Berthelot mixing rules, $\sigma^{\alpha\beta} = 0.5(\sigma^{\alpha\alpha} + \sigma^{\beta\beta})$ and $\varepsilon^{\alpha\beta} = \sqrt{\varepsilon^{\alpha\alpha}\varepsilon^{\beta\beta}}$. To express our results in reduced units, we take $\varepsilon^{ss} = \epsilon = 1$ and $\sigma^{ss} = \sigma = 1$ where s (f) denotes solid (fluid) atoms. The other potential parameters are given, in units of ϵ, by$C_1 = 0.016132$, $C_2 = 3136.6$, $C_3 = -68.069$, $C_4 = -0.083312$ and $C_5 = 0.74689$.

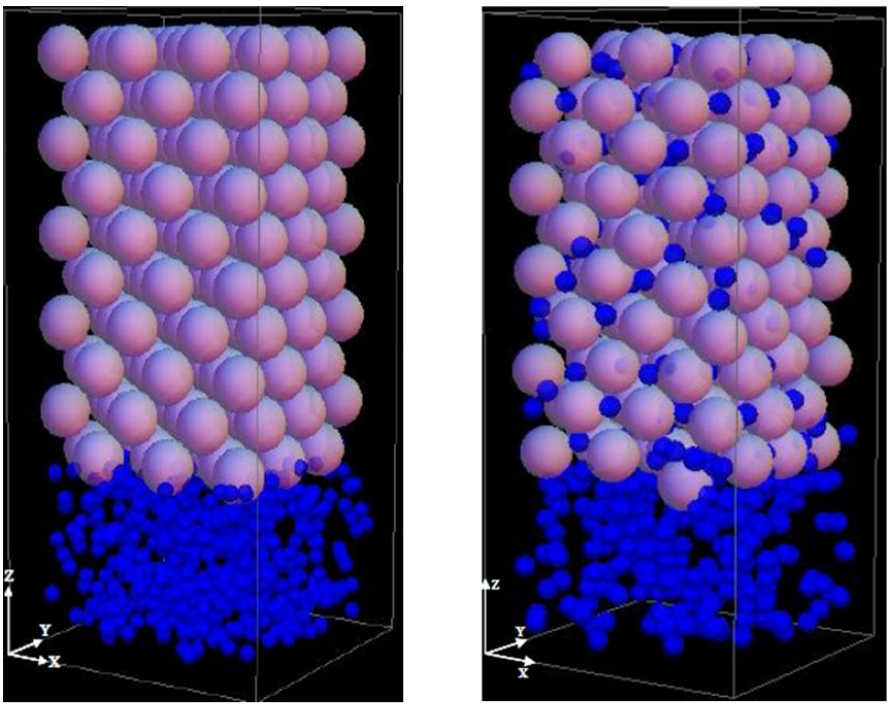

Figure 4-1 (a)A schematic of the simulation cell used to simulate fluid uptake from a reservoir into a deformable solid. (b) A snapshot showing fluid atoms dissolved in the solid.

[2] As is customary, the symbols ε and σ are used here for potential parameters, with superscripts to denote atom types. They should not be confused with the symbols for the components of the strain and stress, which are second-rank tensors.

A simulation begins with $N_s = 180$ solid atoms and $N_f = 170$ or $N_f = 200$ fluid atoms, with masses $m_s = 1$ and $m_f = 0.5$, in a simulation cell of fixed volume with dimensions $l \times l \times L$, where $l = 4.7\sigma$ and $L = 11.0\sigma$, in the x, y, and z directions, respectively. The solid atoms constitute a fcc crystal with a lattice parameter chosen to yield zero pressure for an isolated crystal at the desired temperature, T , using the results of Broughton and Gilmer [88]. These authors performed a series of constant-volume molecular dynamics runs in which the lattice parameter was varied from run to run to obtain zero pressure.

4.4.2 Simulation Procedure

As fluid atoms diffuse into the solid, the solid is strained tetragonally, and therefore the volume of the fluid reservoir decreases correspondingly, consistent with a fixed simulation cell volume. A driving force for diffusion is created by maintaining the chemical potential of the fluid atoms in the reservoir at a fixed value, μ_{res}. For this purpose, we adapted the approach of Heffelfinger and van Swol [84], who combined GCMC simulation with an isothermal molecular dynamics simulation to fix μ_{res} while allowing for diffusional transport on long time scales.

Our procedure, after setting up the simulation system, is as follows. First, fluid atoms in the reservoir are equilibrated with the conventional metropolis Monte Carlo method at fixed N_f. Then the chemical potential of the equilibrated reservoir, μ_{res}., is determined by using Widom's method (Appendix B) [89]. Next, the system is evolved for 50 steps, with each time step being 0.005 (reduced units), using isothermal MD.

Temperature control was achieved via velocity rescaling at every time step. Following this step, the chemical potential of the reservoir is readjusted to μ_{res} by applying GCMC algorithm [84], with approximately 50 attempts for atomic insertion or deletion [39]. An insertion attempt of fluid particle in the reservoir is accepted by:

$$acc\ (N \to N+1) = min\left(1, \frac{V}{\Lambda^3(\mathrm{N}+1)} \exp \frac{-(\mu+\Delta U)}{K_B T}\right) \qquad (4\text{-}6)$$

where V, N and μ are the volume, current number of fluid particles in the reservoir and initial chemical potential, respectively. K_B as a Boltzmann's constant, T as the temperature, ΔU as the energy difference after insertion and Λ as the de Broglie wavelength. Upon the insertion was accepted, its velocities were assigned based on a Maxwell-Boltzmann distribution. Same approach was applied for particle deletion by following probability

$$acc\ (N \to N-1) = min\left(1, \frac{\Lambda^3 \mathrm{N}}{\mathrm{V}} \exp \frac{-(\mu-\Delta U)}{K_B T}\right) \qquad (4\text{-}7)$$

Each course for controlling the chemical potential was included 44 attempts of adjustment which randomly distributed between insertion and deletion. Test result for reservoir chemical potential consistency ($R_f\ /R_s\ =\ 0.414$) is shown in figure 4-2. The average fluctuation is about 3% which indicates GCMC algorithm effectiveness in controlling chemical potential of the reservoir.

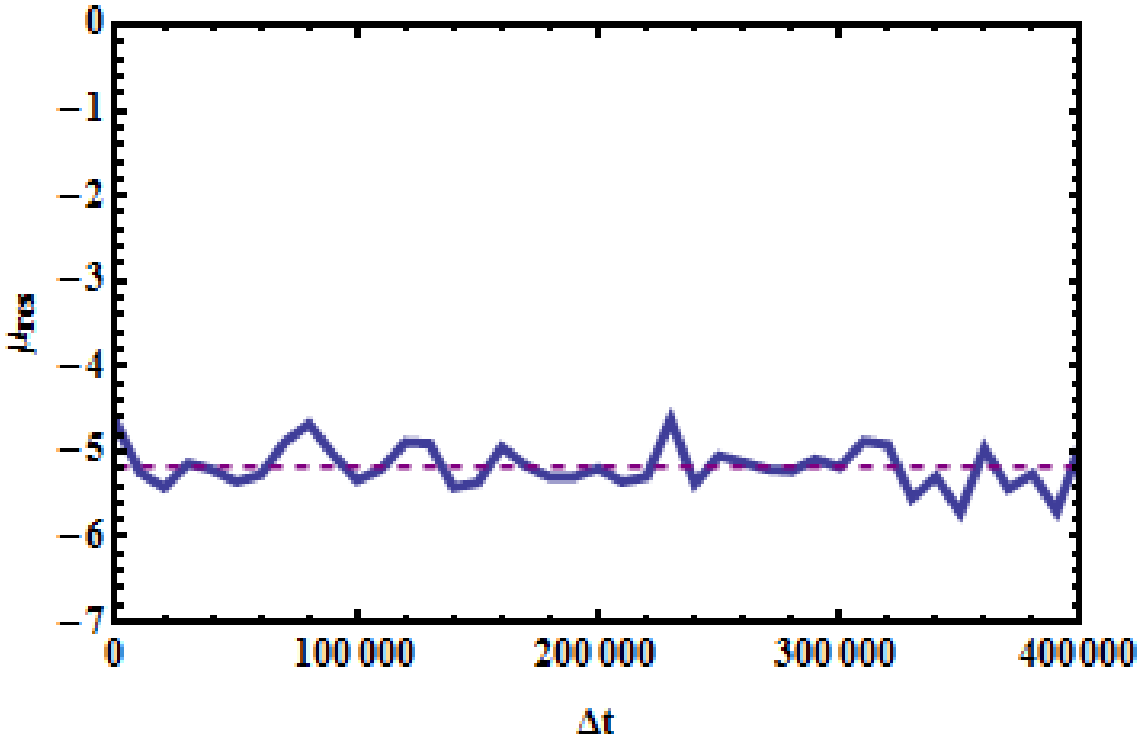

Figure 4-2 Test results for reservoir chemical potential consistency

Widom's method is used periodically to verify that the chemical potential has been set correctly. This sequence of steps is repeated until the solid is saturated with fluid atoms. Depending upon the magnitude of R_f/R_s , typical runs consisted of approximately 2×10^5 to 4×10^6 MDS. Finally, to obtain statistically meaningful data, simulation results were averaged over many realizations of the system (typically 60–80 runs).

4.5 Results

The transport behavior of a fluid in a deformable solid was modeled using two different atomic size ratios, namely $R_f/R_s = 0.30$ and 0.414, to explore the impact of elastic deformation on diffusion. As both ratios are much less than one, it is expected that fluid atoms will dissolve into the interstitial voids in the fcc structure, though preferentially into the larger octahedral voids for the larger fluid atoms. Figure 4-1(b) shows a snapshot of the atomic coordinates after some elapsed time that highlights the dissolution of the fluid atoms.

Consider first a system with $R_f/R_s = 0.30$ at temperature $T = 0.3$. Figure 4-3(a) shows the uptake function, $M(t)/M_\infty$, as a function of square root of simulation time, $\sqrt{t}$, where time is measured in units of Δt. As expected, fluid uptake increases monotonically with time until saturation at late times. To facilitate the interpretation of these data, the uptake curve is replotted in Fig. 4-3(b) as a function of scaled time, $\sqrt{Dt}/\ell$. The diffusion coefficient, D, was determined by fitting the Fickian uptake given in Eq. (4-1) to the data. More specifically, we define a parameter $\mathcal{X}^2 = \sum_i [(M(t_i)/M_\infty) - (M^F(t_i)/M_\infty)]^2$, where the sum is over simulation times and the superscript "*F*" denotes the Fickian result [Eq. (4-1)]. The coefficient D is chosen to minimize $\mathcal{X}^2$. For this system it was found that $D = 0.154\sqrt{\epsilon\sigma 2/m}$. For comparison, the corresponding Fickian uptake function, $M^F(t_i)/M_\infty$, is also displayed in Fig. 4-3(b). As is evident from the figure, the simulation data is well described by a Fickian profile, as might be expected for particles that are able to fit readily into interstices.

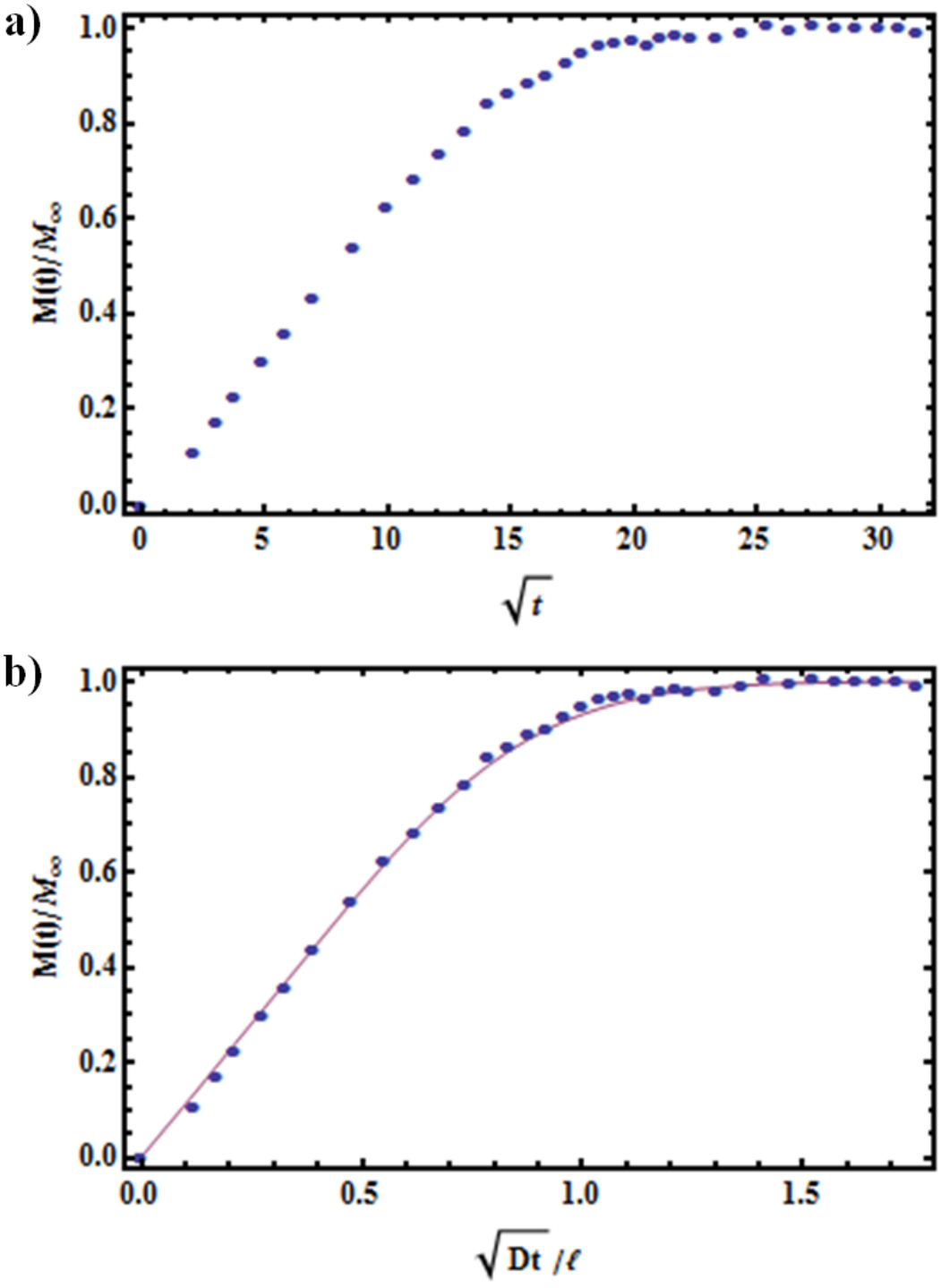

Figure 4-3 (a) The uptake function, $M(t)/M_{\infty}$, as a function of the square root of time, $\sqrt{t}$, for $R_f/R_s = 0.30$. The results were averaged over 60 independent runs with mean fractional error of 0.074 at each recorded time step. (b) The uptake function vs scaled time, $\sqrt{Dt}/\ell$ in comparison with the corresponding Fickian uptake function from Eq. (4-1) (solid line)

While the fluid particles can be accommodated by the voids in the solid, there is, nevertheless, an expansion of the solid due to the compositional strain that attends fluid permeation. To highlight this expansion and also confirm that the solid remains intact, one can calculate the instantaneous structure factor, $S(\vec{k}, t)$, for the solid atoms for a few fcc reciprocal lattice vectors. Figure 4-4(a) shows $S(\vec{k}, t)$ versus time for $k = (4\pi/a)\hat{x}$, $(4\pi/a)\hat{y}$, and $(4\pi/a)\hat{z}$, where a is the lattice parameter. The relatively large values for these quantities indicate that the lattice remains intact, and the tetragonal strain in the z directions splits their degeneracy. In other words, the structure factors in Fig. 4-4 show that the solid lattice, while distorted due to the presence of interstitials, remains crystalline. Moreover, the smaller value of $S(\vec{k} = (4\pi/a)\hat{z}, t)$ at late times indicates that the solid is lengthening in the z direction. Detail explanation about structure factor calculation can be found in appendix (B).

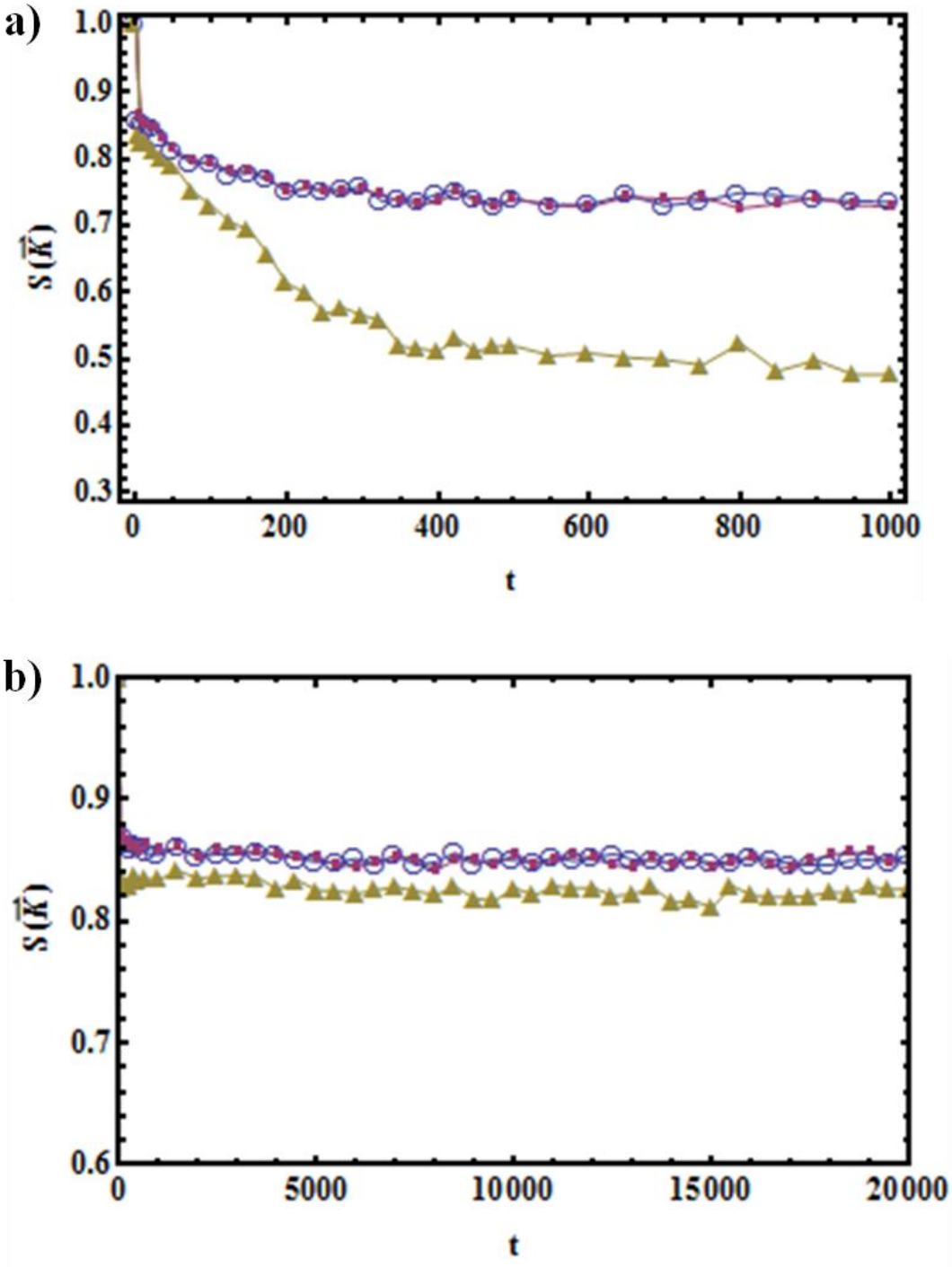

Figure 4-4 (a) The instantaneous structure factor, $S(\vec{k},t)$, vs time for the wave vectors $k = (4\pi/a)\hat{x}$(○), $(4\pi/a)\hat{y}$ (■) and $(4\pi/a)\hat{z}$ (▲), respectively, for $R_f/R_s = 0.30$. (b) The same as in panel (a), except that $R_f/R_s = 0.414$.

A more direct measure of expansion is given in Fig. 4-5(a), which shows the strain component $\epsilon_{zz}(t)$ as a function of time. Clearly, ϵ_{zz} increases with time until saturation as the simulation cell expands to accommodate fluid atoms. The value of the strain at saturation, $\epsilon_{zz} \approx 0.05$, can be used to determine the associated compositional strain parameter η using Eq. (4-4). At this temperature, the bulk modulus $B = 45.8\epsilon/\sigma^3$ and so, given the calculated pressure at saturation, one finds that $\eta = 0.02$.

Consider next a system with $R_f/R_s = 0.414$, again held at temperature $T = 0.3$. Figure 4-6(a) shows the uptake function, $M(t)/M_\infty$, as a function of square root of simulation time, $\sqrt{t}$, and Fig. 4-6(b) shows the uptake function and the corresponding Fickian uptake function versus $\sqrt{Dt}/\ell$. As before, the value for D was determined from a best fit using the $\mathcal{X}^2$ parameter, and the compositional strain parameter $\eta = 0.04$ was determined from ϵ_{zz}at saturation [see Fig.4- 5(b)], as above, by using Eq. (4-4). As is evident from the figure, the uptake function is not accurately described by the Fickian uptake function. The origin of this non-Fickian behavior is discussed below.

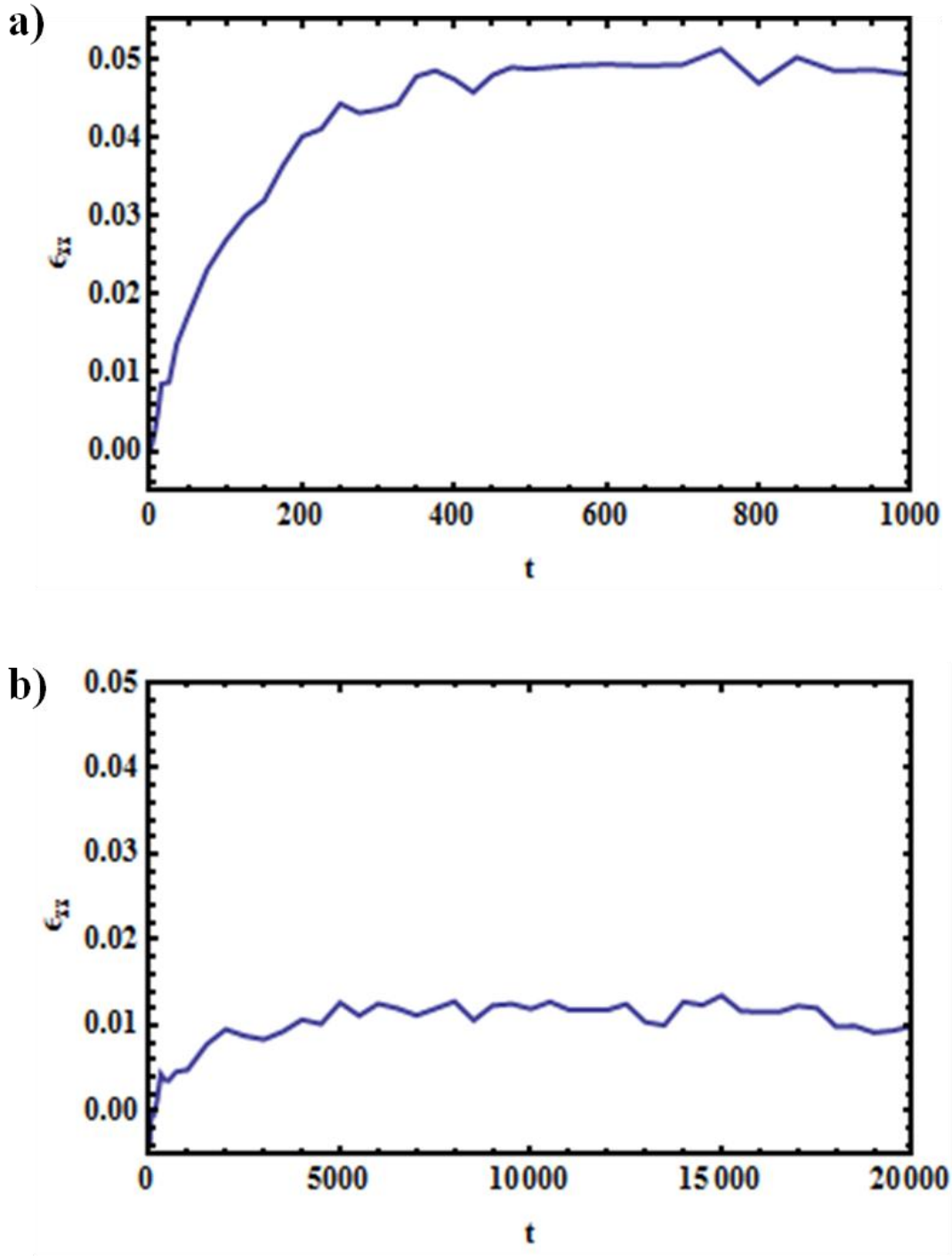

Figure 4-5 The tetragonal strain component, $\epsilon_{zz}(t)$, vs time for a) $R_f/R_s = 0.30$ and b) $R_f/R_s = 0.414$, respectively.

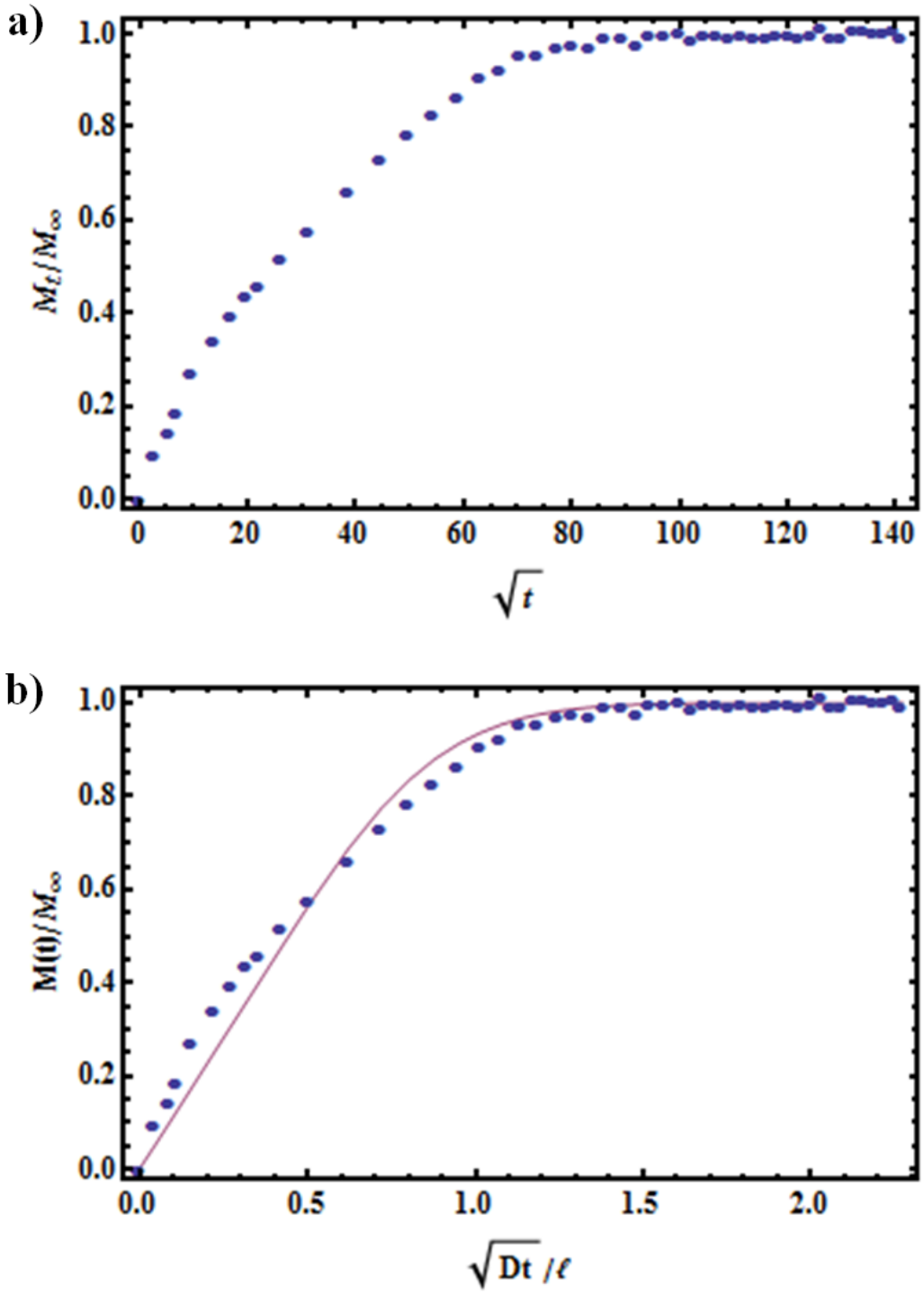

Figure 4-6 (a) The uptake function, $M(t)/M_\infty$, as a function of the square root of time, $\sqrt{t}$, for $R_f/R_s = 0.414$. The results were averaged over 80 independent runs with mean fractional error of 0.074 at each recorded time step. (b) The uptake function vs scaled time, $\sqrt{Dt}/\ell$ in comparison with the corresponding Fickian uptake function from Eq. (4-1) (solid line)

The strain is, of course, associated with diffusant atoms distorting the local atomic environment around structural voids. These local distortions are reflected in $S(\vec{k},t)$, as displayed in Fig. 4-4(b), for the same high-symmetry reciprocal lattice vectors used above. The tetragonal strain induced in the z direction again splits the degeneracy in the structure factor, the relatively large value of $S(\vec{k} = (4\pi/a)\hat{z},t)$, due to the fact that large interstitials constrain the vibrations of lattice atoms.

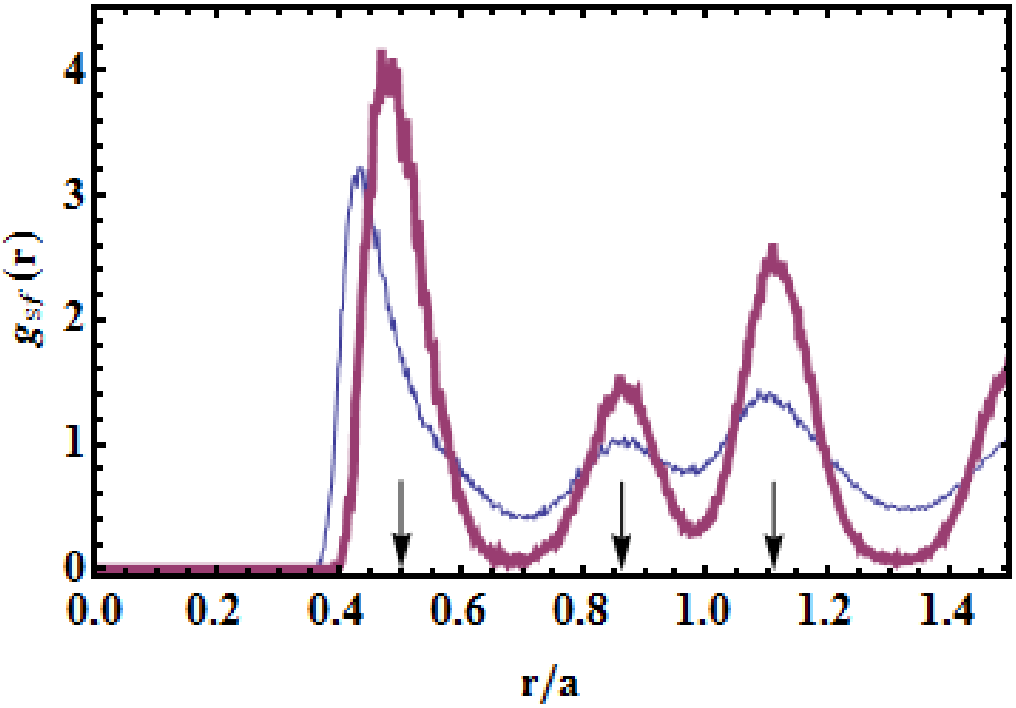

Figure 4-7 The partial radial distribution function, $g_{sf}(r)$, vs distance, r where s and f denote the solid and fluid species, respectively, for $R_f/R_s = 0.30$ (thin curve) and $R_f/R_s = 0.414$ (thick curve). The arrows indicate the location of octahedral interstices. Note that the peaks corresponding to the octahedral locations are more pronounced for $R_f/R_s = 0.414$

The spatial distribution of the fluid atoms in the available interstices is highlighted in Fig. 4-7, which shows the partial radial distribution function, $g_{sf}(r)$, versus distance, r, where s (f) denotes the solid (fluid) atoms, for both $R_f/R_s = 0.30$ and $R_f/R_s =$

0.414. In principle, diffusant atoms can reside in either octahedral or tetrahedral interstices, though larger elastic strains (and therefore larger strain energy) are associated with the tetrahedral voids. However, as noted from the figure, the peaks corresponding to the octahedral voids (indicated by the positions of the arrows) become more pronounced for $R_f / R_s = 0.414$ as these larger voids are required to accommodate larger atoms.

4.6 Discussion

As noted above, the normalized uptake function for a diffusant with $R_f/R_s = 0.414$ is not well described by the corresponding Fickian uptake function given in Eq. (4-1). There are at least two possible reasons for this disagreement. First, in stressed solids, the chemical potential is a function of both concentration and stress (i.e., $\mu = \mu(c, \sigma_{ij})$), and therefore the diffusive flux is, in general, a function of the stress state of the system. For cases in which diffusing atoms are relatively large, the flux will depend on the resulting self-stresses and therefore η. In some cases this stress dependence leads to a flux that depends on the concentration throughout the system, rather than simply on the gradient of the local concentration. In the appendix (C) we discuss in more detail the role of self-stress on diffusion in our problem. It is found that, in our case, the flux depends only on the gradient of the local concentration, and the corresponding diffusion equation is therefore spatially local. Thus, the dependence of the driving force for diffusion on stress does not explain the observed behavior of the uptake function.

Another possible reason for the observed non-Fickian behavior is that the diffusion coefficient is a function of the local concentration, c, as might be expected for interacting diffusant atoms [90]. Such interactions arise from the interatomic potential and from the elastic coupling of centers of dilatation moving in an anisotropic medium. Thus, in our system, one would expect diffusive motion to occur readily for *c* small, but to become slower for larger *c* as stresses generated by the diffusant atoms constrict interstices and migration pathways. To examine this possibility, we consider a simple, two-step parametrization of the diffusion coefficient, namely

$$D(c) = D_1(\eta)\Theta(c) - D_2(\eta)\Theta[c - c_0(\eta)]\,, 0 \le c \le 1 \qquad (4\text{-}8)$$

where D_1, D_2, and c_0 are constants that depend on the compositional strain parameter η and Θ denotes the unit step function. For this parametrization, we solved the associated one dimensional diffusion equation

$$\frac{\partial c}{\partial t} = \frac{\partial}{\partial z}\left[D(c)\frac{\partial c}{\partial z}\right] \qquad (4\text{-}9)$$

numerically using the method of lines [91] for our thin-slab geometry. The corresponding uptake function is displayed in Fig. 4-8, along with the simulation results, for the choices $D_1 = 0.11\sqrt{\epsilon\sigma^2/m}$, $D_2 = 0.01\sqrt{\epsilon\sigma^2/m}$ and $c_0 = 0.2$.

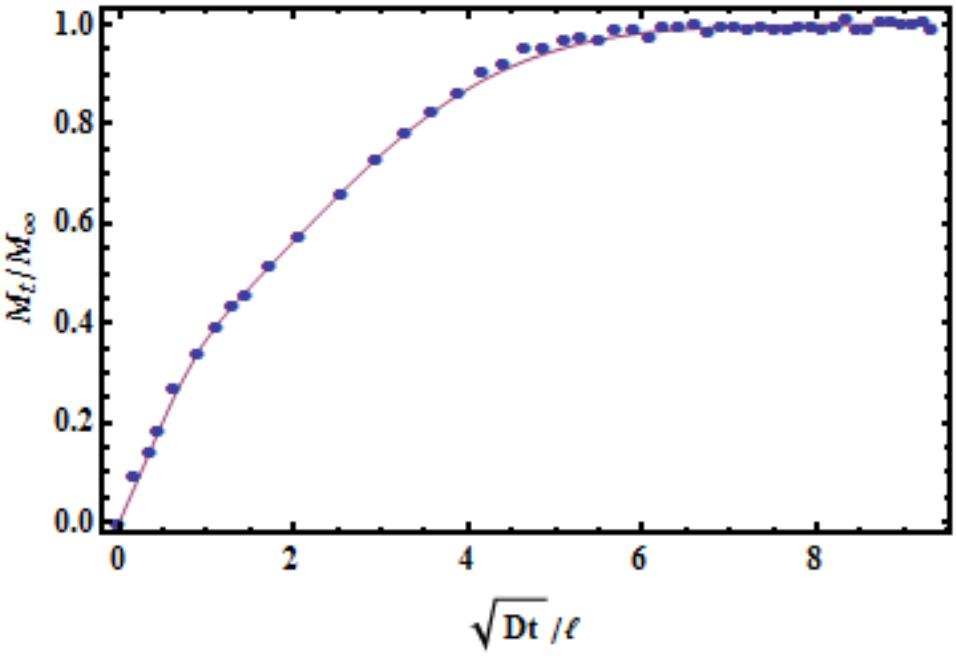

Figure 4-8 The uptake function, $M(t)/M_\infty$, as a function of the square root of the simulation time, $\sqrt{t}$, for $R_f/R_s = 0.414$. Also shown is the uptake as calculated using Eqs. (4-5) and (4-6) (solid line).

This simplified parametrization of $D(c)$ is seen to provide a good description of the simulation results. From these considerations one can infer the behavior of these

parameters as a function of η. For example, one can see that c_0 increases as η decreases, with $c_0 \rightarrow 1$ as $\eta \rightarrow 0$. In addition, it is clear that D_1 is a monotonically decreasing function of η as larger atoms are associated with greater strain along diffusive pathways.

4.7 Conclusion

In this work, a hybrid Monte Carlo–molecular dynamics scheme is employed to model the coupling of a fluid reservoir to a deformable solid, and the resulting permeation of the fluid into the solid was examined to highlight the interplay between diffusional and elastic fields. Both Fickian and non-Fickian regimes are identified and described in terms of the relative size of the fluid and solid atoms. The impact of self-stresses on solid-state diffusion were investigated by monitoring the fluid uptake and evolving partial structure factors and radial distribution functions.

5.

CONCLUSIONS

5.1 Major Achievements

In first project unique methodology is developed to determine the effective diffusivity of the given microstructure based on the information provided by experiment. In this methodology, we have been able to transfer GB energy probability density (obtained by experiment) to a distribution function of GB activation energy and then use that in FD numerical simulation for calculating effective diffusivity and also effective activation energy of entire microstructure.

Second project is also proposing a new framework for investigating elastic behavior of solid under fluid infiltration in atomistic scale. Setting a deformable solid in contact with infinite fluid reservoir can provide more realistic conditions for modeling of fluid diffusion through the solid matrix. This framework can be employed for various applications ranging from membranes and porous materials to grain boundary diffusion.

5.2 Summary of Findings

In first part of this work we employed both analytical and numerical methods to examine the impact of GB variability (i.e., a spectrum of boundary activation energies) on diffusion in a polycrystal. In particular, we calculated an effective diffusivity, , and associated activation energy, Q_{eff} , as a function of temperature for different microstructures using simplified, multi-state models and models based on experimentally obtained GB energy distributions. The main conclusions of this study are as follows.

1. The variability in polycrystalline GB character leads, via the Borisov relation, to a probability density for GB activation energies and an associated effective diffusivity that can be characterized by a few parameters.

2. From the effective diffusivity one can obtain temperature dependent effective activation energy. From this activation energy, one can identify different diffusive regimes and transition temperatures.

3. Effective medium theory can be generalized to incorporate both bulk and multiple GB diffusivities. This theory describes the effective diffusivity in some polycrystalline systems over a wide range of temperatures.

4. Complexion transitions affect the spectrum of GB activation energies, and one can assess their impact on GB diffusion using the numerical procedure described above.

In the second part, a hybrid Monte Carlo–molecular dynamics scheme is employed to model the coupling of a fluid reservoir to a deformable solid, and the resulting permeation of the fluid into the solid was examined to highlight the interplay between diffusional and elastic fields. Both Fickian and non-Fickian regimes are identified and described in terms of the relative size of the fluid and solid atoms. The impact of self-stresses on solid-state diffusion were investigated by monitoring the fluid uptake and evolving partial structure factors and radial distribution functions.

5.3 Future Works

Several extensions of this work are currently underway. For the first project, it is of interest to determine how microstructural descriptors, such as grain size and shape, affect D_{eff}. With regard to grain size, stereological arguments can be used to estimate the fraction of GB sites. For example, for a Poisson Voronoi structure the average GB perimeter per grain is $4/\sqrt{\rho}$, where ρ is the areal grain density [74]. Thus, it is straightforward to estimate the fraction of boundary sites for a fixed number of grains. Second, as indicated above, the assignment of activation energies to boundaries in this work was, for simplicity, taken to be random. In reality, one would expect GB properties to be spatially correlated, and it would therefore be of interest to examine quantitatively how spatial correlations influence D_{eff}. This may be accomplished by introducing a correlation length in the distribution of GB properties that would extend no more than one or two average grain diameters. Finally, in many studies of GB diffusion in polycrystals the grains coarsen during the course of an experiment. The introduction of grain coarsening in our model represents a significant future challenge.

The results obtained in atomistic project suggest that analogous simulation studies of fluid uptake in porous media will be useful in elucidating the roles of pore geometry and stress on diffusion. Given the geometric complexity of a porous medium, it will be of interest to characterize the interconnectivity of the porous network and to calculate the local stresses [92] in different regions of the system. It is expected that the swelling of portions of this network that attend diffusion will alter the corresponding diffusive flux. A simulational study of fluid uptake by a porous medium is the subject of future work.

BIBLIOGRAPHY

1. Mishin, Y. & Herzig, C. Grain boundary diffusion: recent progress and future research. *Materials Science and Engineering: A* **260,** 55–71 (1999).
2. Kaur, I., Mishin, Y. & Gust, W. Fundamentals of Grain and Interphase Boundary Diffusion. (Wiley, 1995).
3. Barnes, R. S. Diffusion of Copper along the Grain Boundaries of Nickel. *Nature* **166,** 1032–1033 (1950).
4. Hoffman, R. E. & Turnbull, D. Lattice and Grain Boundary Self-Diffusion in Silver. *Journal of Applied Physics* **22,** 634–639 (1951).
5. Shewmon, P. *Diffusion in Solids*. (Wiley, 1991).
6. Fisher, J. C. Calculation of Diffusion Penetration Curves for Surface and Grain Boundary Diffusion. *Journal of Applied Physics* **22,** 74–77 (1951).
7. Grjaznovs, D. Simulation of Diffusion in Nanocrystalline Materials: Continuum Approach. (2006).
8. Whipple, R. T. P. CXXXVIII. Concentration contours in grain boundary diffusion. *Philosophical Magazine Series 7* **45,** 1225–1236 (1954).
9. Suzuoka, T. Lattice and grain boundary diffusion in polycrystals. *Trans. Japanese Inst. Met. 2, 25* **33,** (1961).
10. Levine, H. S. & MacCallum, C. J. Grain Boundary and Lattice Diffusion in Polycrystalline Bodies. *Journal of Applied Physics* **31,** 595–599 (1960).
11. Claire, A. D. L. The analysis of grain boundary diffusion measurements. *Br. J. Appl. Phys.* **14,** 351 (1963).

12. Harrison, L. G. Influence of dislocations on diffusion kinetics in solids with particular reference to the alkali halides. *Trans. Faraday Soc.* **57,** 1191–1199 (1961).
13. Marquardt, K. *Grain boundary structure and element transport processes studied at the nm-scale using transmission electron microscopy (TEM) / vorgelegt von Katharina Marquardt (neé Hartmann)*. (2010).
14. Gilmer, G. H. & Farrell, H. H. Grain-boundary diffusion in thin films: I. The isolated grain boundary. *Journal of Applied Physics* **47,** 3792–3798 (1976).
15. Swiler, T. P. & Holm, E. A. *Diffusion in Polycrystalline Microstructures*. (Sandia National Labs., Albuquerque, NM (United States), 1995).
16. Klinger, L. & Rabkin, E. Beyond the Fisher model of grain boundary diffusion: effect of structural inhomogeneity in the bulk. *Acta Materialia* **47,** 725–734 (1999).
17. Gambaryan-Roisman, T., Litovsky, E., Shapiro, M. & Shavit, A. Reaction–diffusion model of surface and grain boundary segregation kinetics. *International Journal of Heat and Mass Transfer* **43,** 4135–4151 (2000).
18. Bedu-Amissah, K., Rickman, J. M., Chan, H. M. & Harmer, M. P. Impact of microstructure on grain-boundary diffusion in polycrystals. *Journal of Applied Physics* **98,** 063511 (2005).
19. Chen, Y. & Schuh, C. A. Diffusion on grain boundary networks: Percolation theory and effective medium approximations. *Acta Materialia* **54,** 4709–4720 (2006).

20. Chen, Y. & Schuh, C. A. Geometric considerations for diffusion in polycrystalline solids. *Journal of Applied Physics* **101,** 063524 (2007).
21. Schuh, C. A., Minich, R. W. & Kumar, M. Connectivity and percolation in simulated grain-boundary networks. *Philosophical Magazine* **83,** 711–726 (2003).
22. Li, J., Dillon, S. J. & Rohrer, G. S. Relative grain boundary area and energy distributions in nickel. *Acta Materialia* **57,** 4304–4311 (2009).
23. De Kee, D., Liu, Q. & Hinestroza, J. Viscoelastic (Non-Fickian) Diffusion. *Can. J. Chem. Eng.* **83,** 913–929 (2005).
24. Edwards, D. A. Non-fickian diffusion in thin polymer films. *J. Polym. Sci. B Polym. Phys.* **34,** 981–997 (1996).
25. Gao, P. & Mackley, M. R. A General Model for the Diffusion and Swelling of Polymers and its Application to Ultra-High Molecular Mass Polyethylene. *Proc. R. Soc. Lond. A* **444,** 267–285 (1994).
26. Hui, C.-Y., Wu, K.-C., Lasky, R. C. & Kramer, E. J. Case-II diffusion in polymers. I. Transient swelling. *Journal of Applied Physics* **61,** 5129–5136 (1987).
27. Hagan, P. Uptake Curves for Fickian Diffusion. *SIAM J. Appl. Math.* **46,** 605–613 (1986).
28. Hartley, G. S. Diffusion and swelling of high polymers. Part III.—anisotropic swelling in oriented polymer film. *Trans. Faraday Soc.* **45,** 820–832 (1949).
29. Aifantis, E. C. On the problem of diffusion in solids. *Acta Mechanica* **37,** 265–296 (1980).

30. Cohen, D. S. Theoretical models for diffusion in glassy polymers. *J. Polym. Sci. Polym. Phys. Ed.* **21,** 2057–2065 (1983).

31. Thomas, N. L. & Windle, A. H. A theory of case II diffusion. *Polymer* **23,** 529–542 (1982).

32. Cox, R. Stress-Assisted Diffusion: A Free Boundary Problem. *SIAM J. Appl. Math.* **51,** 1522–1537 (1991).

33. Leroy, F., Rousseau, B. & Fuchs, A. H. Self-diffusion of n-alkanes in silicalite using molecular dynamics simulation: A comparison between rigid and flexible frameworks. *Phys. Chem. Chem. Phys.* **6,** 775–783 (2004).

34. Gelb, L. D. & Hopkins, A. C. Dynamics of the Capillary Rise in Nanocylinders. *Nano Lett.* **2,** 1281–1285 (2002).

35. Ahadian, S., Mizuseki, H. & Kawazoe, Y. On the kinetics of the capillary imbibition of a simple fluid through a designed nanochannel using the molecular dynamics simulation approach. *Journal of Colloid and Interface Science* **352,** 566–572 (2010).

36. Joly, L. Capillary filling with giant liquid/solid slip: Dynamics of water uptake by carbon nanotubes. *The Journal of Chemical Physics* **135,** 214705 (2011).

37. Stukan, M. R., Ligneul, P., Crawshaw, J. P. & Boek, E. S. Spontaneous Imbibition in Nanopores of Different Roughness and Wettability. *Langmuir* **26,** 13342–13352 (2010).

38. Allen, M. P. & Tildesley, D. J. *Computer Simulation of Liquids*. (Clarendon Press, 1989).

39. Frenkel, D. & Smit, B. *Understanding Molecular Simulation: From Algorithms to Applications*. (Academic Press, 2001).

40. Stan, M. Discovery and design of nuclear fuels. *Materials Today* **12,** 20–28 (2009).

41. Patankar, S. *Numerical Heat Transfer and Fluid Flow*. (CRC Press, 1980).

42. *Numerical Recipes in FORTRAN: The Art of Scientific Computing*. (Cambridge University Press, 1992).

43. Battaile, C. C. The Kinetic Monte Carlo method: Foundation, implementation, and application. *Computer Methods in Applied Mechanics and Engineering* **197,** 3386–3398 (2008).

44. Girifalco, L. A. *Atomic migration in crystals*. (Blaisdell Pub. Co., 1964).

45. Kim, C.-S., Hu, Y., Rohrer, G. S. & Randle, V. Five-parameter grain boundary distribution in grain boundary engineered brass. *Scripta Materialia* **52,** 633–637 (2005).

46. Cantwell, P. R. *et al.* Grain boundary complexions. *Acta Materialia* **62,** 1–48 (2014).

47. Rickman, J. M., Chan, H. M., Harmer, M. P. & Luo, J. Grain-boundary layering transitions in a model bicrystal. *Surface Science* **618,** 88–93 (2013).

48. Kaur, I., Mishin, Y. & Gust, W. *Fundamentals of Grain and Interphase Boundary Diffusion*. (Wiley, 1995).

49. Gilmer, G. H. & Farrell, H. H. Grain-boundary diffusion in thin films. II. Multiple grain boundaries and surface diffusion. *Journal of Applied Physics* **47,** 4373–4380 (1976).

50. Mishin, Y. M. & Herzig, C. Effective diffusion coefficient and correlation effects in periodic grain boundaries. *Philosophical Magazine A* **71,** 641–660 (1995).

51. Levine, H. S. & MacCallum, C. J. Grain Boundary and Lattice Diffusion in Polycrystalline Bodies. *Journal of Applied Physics* **31,** 595–599 (1960).

52. Li, L. & Holland, S. Grain boundary diffusion: non-random topology and effective medium approximation. *Nanomaterials and Energy* **3,** 139–147 (2014).

53. Prager, S. Diffusion in Inhomogeneous Media. *The Journal of Chemical Physics* **33,** 122–127 (1960).

54. Du, Q., Faber, V. & Gunzburger, M. Centroidal Voronoi Tessellations: Applications and Algorithms. *SIAM Rev.* **41,** 637–676 (1999).

55. Espinosa, H. D., Berbenni, S., Panico, M. & Schwarz, K. W. An interpretation of size-scale plasticity in geometrically confined systems. *PNAS* **102,** 16933–16938 (2005).

56. Beladi, H. & Rohrer, G. S. The relative grain boundary area and energy distributions in a ferritic steel determined from three-dimensional electron backscatter diffraction maps. Acta Materialia 61, 1404–1412 (2013).

57. V. T. Borisov, V. M. Golikov and G. V. Scherbedinskiy, Relationship between diffusion coefficients and grain boundary energy.Phys. Met. Metall. 17, 80-84

58. P. Guiraldenq and P. Poiret, Mem. Sci. Rev. Met. 70, 715-723 (1973).

59. Chen, T.-F., Tiwari, G. P., Iijima, Y. & Yamauchi, K. Volume and grain boundary diffusion of chromium in Ni-base Ni-Cr-Fe alloys. (2003
60. Pelleg, J. On the relation between diffusion coefficients and grain boundary energy. *Philosophical Magazine* **14,** 595–601 (1966).
61. Nicholas, J. F. Apparent Activation Energy and Frequency Factor for a Process Involving Competing Mechanisms. *The Journal of Chemical Physics* **31,** 922–925 (1959).
62. Zaman, M. H., Sosnick, T. R. & Berry, R. S. Temperature dependence of reactions with multiple pathways. *Phys. Chem. Chem. Phys.* **5,** 2589–2594 (2003).
63. Pathria, R. K. & Beale, P. D. *Statistical Mechanics*. (Academic Press, 2011).
64. Hashin, Z. & Shtrikman, S. A Variational Approach to the Theory of the Effective Magnetic Permeability of Multiphase Materials. *Journal of Applied Physics* **33,** 3125–3131 (1962).
65. Hart, E. W. On the role of dislocations in bulk diffusion. *Acta Metallurgica* **5,** 597 (1957).
66. Garnett, J. C. M. Colours in Metal Glasses and in Metallic Films. *Phil. Trans. R. Soc. Lond. A* **203,** 385–420 (1904).
67. Kirkpatrick, S. Percolation and Conduction. *Rev. Mod. Phys.* **45,** 574–588 (1973).
68. McLachlan, D. S. An equation for the conductivity of binary mixtures with anisotropic grain structures. *J. Phys. C: Solid State Phys.* **20,** 865 (1987).
69. Sapoval, B., Hermann, C. & Hermann, C. *Physics of Semiconductors*. (Springer Science & Business Media, 2003).

70. Van Vliet, K. J., Tsikata, S. & Suresh, S. Model experiments for direct visualization of grain boundary deformation in nanocrystalline metals. *Applied Physics Letters* **83,** 1441–1443 (2003).
71. Heuer, A. H. Oxygen and aluminum diffusion in α-Al2O3: How much do we really understand? *Journal of the European Ceramic Society* **28,** 1495–1507 (2008).
72. A. Kundu, K. M. Asl, J. Luo and M. P. Harmer, Scripta Mater. 68, 146 (2012).
73. S. J. Dillon and M. P. Harmer, J. Am. Ceram. Soc. 91, 2304-2313 (2008).
74. Okabe, A., Boots, B., Sugihara, K. & Chiu, S. N. *Spatial Tessellations: Concepts and Applications of Voronoi Diagrams*. (John Wiley & Sons, 2009).
75. Transient swelling. *Journal of Applied Physics* **61,** 5129–5136 (1987).
76. Wang, H. *Theory of Linear Poroelasticity with Applications to Geomechanics and Hydrogeology*. (Princeton University Press, 2000).
77. Cowin, S. C. A Recasting of Anisotropic Poroelasticity in Matrices of Tensor Components. *Transport in Porous Media* **50,** 35–56 (2003).
78. Biot, M. A. General Theory of Three-Dimensional Consolidation. *Journal of Applied Physics* **12,** 155–164 (1941).
79. Dubé, M. *et al.* Liquid Conservation and Nonlocal Interface Dynamics in Imbibition. *Phys. Rev. Lett.* **83,** 1628–1631 (1999).
80. Rickman, J. M. The role of elastic anisotropy in poroelastic transport. *Journal of Applied Physics* **106,** 044911 (2009).
81. Crank, J. *The mathematics of diffusion*. (Clarendon Press, 1975).

82. Petropoulos, J. H., Sanopoulou, M. & Papadokostaki, K. G. Physically insightful modeling of non-Fickian kinetic regimes encountered in fundamental studies of isothermal sorption of swelling agents in polymeric media. *European Polymer Journal* **47,** 2053–2062 (2011).
83. Larcht'e, F. C. & Cahn, J. l. The effect of self-stress on diffusion in solids. *Acta Metallurgica* **30,** 1835–1845 (1982).
84. Heffelfinger, G. S. & Swol, F. van. Diffusion in Lennard-Jones fluids using dual control volume grand canonical molecular dynamics simulation (DCV-GCMD). *The Journal of Chemical Physics* **100,** 7548–7552 (1994).
85. Lynch, G. C. & Pettitt, B. M. Grand canonical ensemble molecular dynamics simulations: Reformulation of extended system dynamics approaches. *The Journal of Chemical Physics* **107,** 8594–8610 (1997).
86. Ji, J., Çağin, T. & Pettitt, B. M. Dynamic simulations of water at constant chemical potential. *The Journal of Chemical Physics* **96,** 1333–1342 (1992).
87. Papadopoulou, A., Becker, E. D., Lupkowski, M. & Swol, F. van. Molecular dynamics and Monte Carlo simulations in the grand canonical ensemble: Local versus global control. *The Journal of Chemical Physics* **98,** 4897–4908 (1993).
88. Broughton, J. Q. & Gilmer, G. H. Molecular dynamics investigation of the crystal–fluid interface. I. Bulk properties. *The Journal of Chemical Physics* **79,** 5095–5104 (1983).
89. Widom, B. Some Topics in the Theory of Fluids. The Journal of Chemical Physics 39, 2808–2812 (1963).

90. Kutner, R., Binder, K. & Kehr, K. W. Diffusion in concentrated lattice gases. II. Particles with attractive nearest-neighbor interaction on three-dimensional lattices. Phys. Rev. B 26, 2967–2980 (1982).
91. Schiesser, W. E. The Numerical Method of Lines: Integration of Partial Differential Equations. (Academic Press, 1991).
92. Cormier, J., Rickman, J. M. & Delph, T. J. Stress calculation in atomistic simulations of perfect and imperfect solids. Journal of Applied Physics 89, 99–104 (2001).
93. Hammond, C. *The Basics of Crystallography and Diffraction*. (Oxford University Press, 2009).
94. Larché, F. C. & Cahn, J. W. Overview no. 41 The interactions of composition and stress in crystalline solids. Acta Metallurgica 33, 331–357 (1985).
95. Atanackovic, T. M. & Guran, A. Theory of Elasticity for Scientists and Engineers. (Springer Science & Business Media, 2000).
96. Mura, T. Micromechanics of Defects in Solids. (Springer Science & Business Media, 1987).

APPENDIX

APPENDIX A

In all simulation studies, it is common to verify model by a classic example with already known answer. As mentioned before Whipple analytical solution for isolated grain boundary is precise and exact. In this order we employed that to verify our numerical solution. The schematic of framework setup for Whipple solution can be seen in figure A-1. As it is shown, isolated grain boundary is embedded in bi-crystal system in contact with constant source at the bottom. Diffusants are able to penetrate through the both grains as well as the grain boundary. Since grain boundary diffusivity is much higher than grains (in this case $D_{GB}/D_L = 10^4$), diffusion front advances into the grain boundary faster than the grains. This advancement leads to a severe concentration gradient between grain boundary and grains. Consequently, secondary diffusion accrues as a leakage from the grain boundary through the grains.

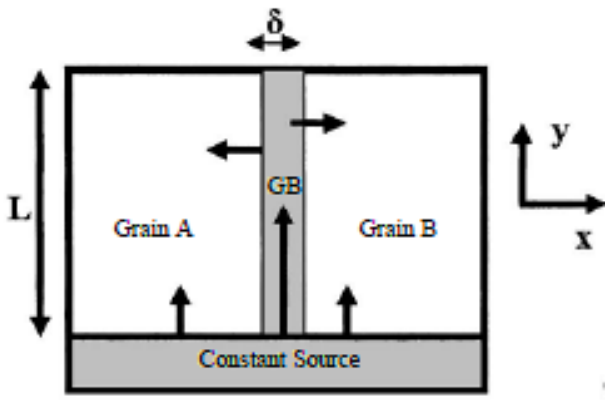

Figure A-1 Schematic of isolated grain boundary for Whipple analytical solution

To model this problem, we solved Fick's second equation (Unsteady-state condition) in the domain by considering zero gradient (Neumann) boundary condition at top and lateral sides and constant concentration at bottom. The prediction of model then compared with Whipple analytical solution [8,2]. Figure A-2 shows the concentration contours obtained by model at certain time.

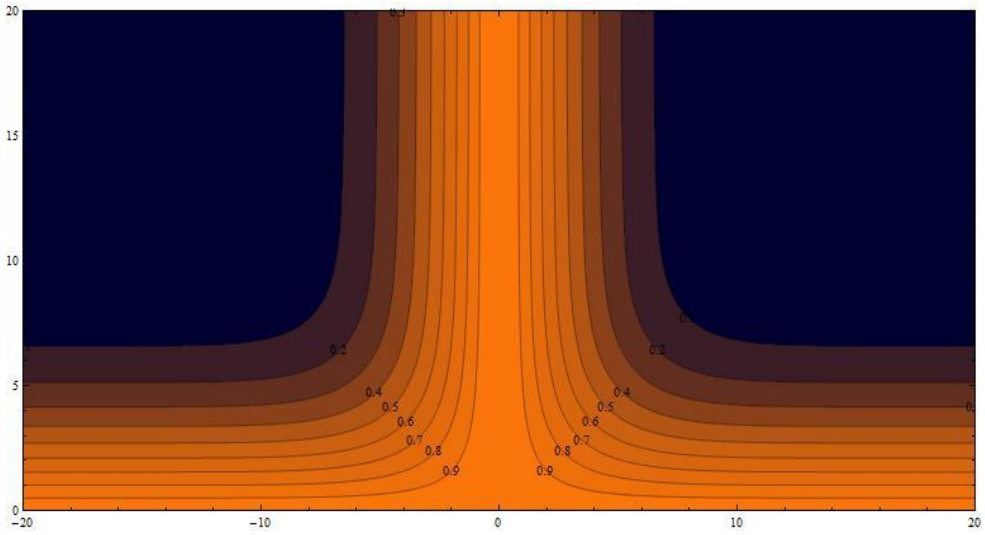

Figure A-2 An example of concentration contours obtained by model

Whipple worked out his solution by using the Fourier-Laplace transformation technique. His solution is valid for narrow grain boundary under certain conditions as follows [2];

- $D_{GB} \gg D_L$
- D_{GB} and D_L are independent of concentration, position and time
- Flux continuity at GB/Lattice interface

Considering all above, diffusant concentration in bulk can be calculated by

$$c_L(\xi,\eta,\beta) = c_0 erfc(\eta/2) + \frac{c_0\eta}{2\pi^{1/2}}\int_1^{\Delta} \frac{\exp(-\eta^2/4\sigma)}{\sigma^{3/2}} \times erfc\left[\frac{1}{2}\left(\frac{\Delta-1}{\Delta-\sigma}\right)^{1/2}(\xi+\frac{\sigma-1}{\beta})\right] d\sigma \quad \text{(A1)}$$

Where ξ, η and β are dimensionless variables corresponding to x, y and t , respectively and Δ is a dimensionless parameter define as;

$$\xi = \frac{x-\delta/2}{(D_L t)^{1/2}} \quad \text{(A2)}$$

$$\eta = y/(D_L t)^{1/2} \quad \text{(A3)}$$

$$\beta = \frac{(\Delta-1)\delta}{2(D_L t)^{1/2}} \quad \text{(A4)}$$

$$\Delta = \frac{D_{GB}}{D_L} \quad \text{(A5)}$$

These dimensionless variables have physical meaning as well. η represents direct volume diffusion from source into the grains. On the other hand, ξ stands for volume diffusion from grain boundary in to the grains. β can be described as a ratio between GB/Bulk diffusion lengths. To have accurate measurement in sectioning experiments β must be greater than 10 to hold essential condition for this analytical solution [2].

Whipple equation has been solved numerically by using Mathematica software dimensionless variables determined for our system. Then we have been able to make comparison between model predictions and Whipple analytical solution.

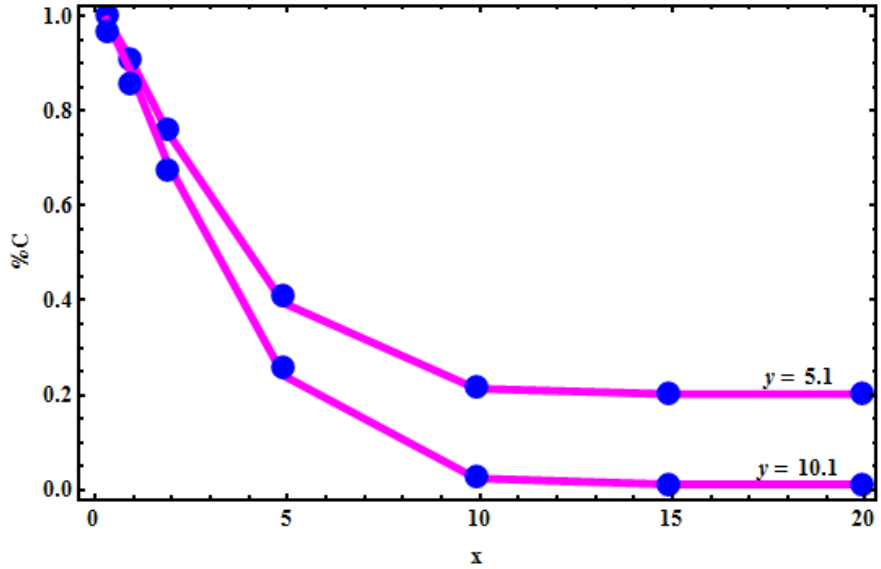

Figure A-3 Plot of concentration change in x direction for $y = 5.1$ and $y = 10.1$, as determined by the unsteady-state diffusion model (circles) and from the Whipple analytical solution (solid line)

As shown in figure A-3, results have been predicted by model are in reasonable consistency with Whipple analytical solution. Only 1% deviation from analytical solution was observed. This small inconsistency was also expected owing to employing finite difference control volume in numerical model which solves diffusion equation in discrete manner rather than continues approach used by Whipple [15, 18]. This level of precision in model prediction assured us about reliability of employed numerical solution.

APPENDIX B

In this appendix, we are going to explain some statistical mechanics approaches for calculating desire thermodynamics and structural properties of the system modeled in atomistic scale.

Widom Method to Determine Chemical Potential

Widom insertion method [89] is a simple and precise way to measure chemical potential in low density fluid. The statistical mechanics behind this method is quit intuitive and comes from original definition of chemical potential μ in thermodynamics.

$$\mu = \left(\frac{\partial F}{\partial N}\right)_{VT} = -T\left(\frac{\partial S}{\partial N}\right)_{VE} \qquad \text{(B1)}$$

Where F and S are the Helmholtz free energy and entropy. In this order, by following the expression of Helmholtz free energy $F(N,V,T) = -k_B T \ln Q$ and Eq.(B1), one can derive chemical potential for a large$N$ as;

$$\mu = -k_B T \ln(Q_{N+1}/Q_N) \qquad \text{(B2)}$$

By using partition function, above equation could be written in statistical mechanics as;

$$\mu = -k_B T \ln\left(\frac{V/\Lambda^d}{N+1}\right) - k_B T \ln\left(\frac{\int dS^{N+1} exp[-\beta U(S^{N+1})]}{N+1 \int dS^N exp[-\beta U(S^N)]}\right) \qquad \text{(B3)}$$

Equation (B3) can be separated an ideal gas contribution μ_{id} and the excess part μ_{ex}as

$$\mu = \mu_{id} + \mu_{ex} \qquad \text{(B4)}$$

Since the ideal gas contribution can be evaluated analytically, we are here interested in μ_{ex}. Considering that $\Delta U = U(S^{N+1}) - U(S^N)$ we can write μ_{ex} as;

$$\mu_{ex} = -k_B T \ln \int dS_{N+1} \langle exp(-\beta \Delta U) \rangle_N \qquad \text{(B5)}$$

Or

$$\mu_{ex} = -k_B T \ln\langle exp(-\beta \Delta U)\rangle_N \qquad \text{(B6)}$$

Where $\langle exp(-\beta \Delta U)\rangle_N$ stands for canonical ensemble average of Boltzmann factor over the configuration of N-particle system. Eq. (B6) can be simply utilized by conventional Metropolis sampling. In practice, the procedure is as follow;

- Conventional Monte-Carlo simulation carried out on the system of N particle
- In predetermined interval, imaginary particle $(N + 1)$ inserts to the random coordination generated into the system to compute $exp(-\beta \Delta U)$ at S_{N+1}.
- Previous step repeats to reach to reasonable average for$\langle exp(-\beta \Delta U)\rangle_N$
- μ_{ex} is determined without imposing any change to the N-particle system.

The important point in Widom method is that although it has many similarities with Metropolis and GCMC algorithms, but during the run we never accept any trial insertions. We just evaluate response of N-particle system to presence of an extra particle and use that to determine chemical potential of N-particle system.[39]

Statistic Structure Factor

In solid state physics and crystallography, the static structure factor is a mathematical function describing the amplitude and phase of a wave diffracted from crystal lattice planes characterized by Miller indices (*h*,*k*,*l*). In that sense, it is able to reveal information about the amount of atom displacements from their original coordination in crystalline structure. The structure factor $S(\vec{k})$ can be expressed as;

$$S(\vec{k}) = \sum_j f_j exp(2\pi i[h.x(j) + k.y(j) + l.z(j)]) \qquad \text{B(7)}$$

where the sum is over all atoms in the unit cell, *x(j),y(j),z(j)* are the positional coordinates of the j[th] atom. Assuming we are going to compute structure factor in (1,1,1) direction. The procedure in simulation would be as take a following summation over all atoms in the system

$$F = \sum_j exp\left(\frac{2\pi i}{a}[1.x(j) + 1.y(j) + 1.z(j)]\right) \quad \text{B(8)}$$

Where a is a lattice constant and then $S(1,1,1)$ could be calculated as;

$$S(1,1,1) = \frac{1}{N \times N}(F.F^*) \quad \text{B(9)}$$

Where F^* is a complex conjugate of F. Ideally this value should be one, but in reality its actual value for crystalline materials is close to one. Higher value for this parameter indicates fewer changes in original crystal structure.[93]

APPENDIX C

In this appendix, we examine the dependence of the diffusive flux on the concentration field. The diffusive flux depends on the gradient of the chemical potential of the diffusing species and, as discussed above for a deformable solid, this potential depends on the stress state of the system. With the assumption that mechanical equilibrium obtains quickly on the time scale of mass diffusion, it can be shown that in some cases the stress is a functional of the concentration field, thereby rendering diffusion spatially nonlocal and therefore non-Fickian. One such case is that of mass transport in an infinite, elastically anisotropic solid having cubic symmetry [94]. Another example is that of diffusion in an elastically isotropic plate in which one side of the plate is in contact with a fluid, with a resulting asymmetric concentration profile [83]. The system considered here is a thin, elastically anisotropic plate having cubic symmetry in contact with a fluid on two faces. We consider below the diffusive flux in this system.

Larch´e and Cahn [94] have shown that the components of the diffusive flux, $\vec{J}$, can be written as

$$J_i = -\mathcal{L}\frac{\partial}{\partial x_i}[\mu_0(c) - (\eta/\rho)\sigma_{kk}(\vec{r})] \qquad \text{(C1)}$$

where $\mathcal{L}$ is a kinetic coefficient, μ_0 is a part of the chemical potential that depends on concentration, and ρ is the density. It has been assumed here that the elastic constants of the system do not depend on c.

Assuming that the elastic fields relax quickly on the time scale of atomic diffusion, σ_{ii}can be expressed in terms of c. This may be accomplished by starting with the equations of compatibility [95]

$$e_{ikr}e_{jls}\frac{\partial^2\epsilon_{ij}}{\partial x_k \partial x_l} = 0 \qquad \text{(C2)}$$

Where e_{ikr} are the components of the Levi-Civita tensor, and rewriting them in terms of the stress.

The components of the strain tensor can be written in terms of those of the stress tensor by inverting Eq. (4-2) to obtain

$$\epsilon_{ij} = S_{ijkl}\sigma_{kl} + \epsilon_{ij}^{c} \qquad \text{(C3)}$$

where the S_{ijkl} are the components of the compliance tensor. For a cubic solid [96],

$$S_{ijkl} = \alpha\delta_{ij}\delta_{kl} + \beta\left(\delta_{ik}\delta_{jl} + \delta_{il}\delta_{jk}\right) + \gamma\delta_{ijkl} \qquad \text{(C4)}$$

where δ_{ij} is the Kronecker δ and $\delta_{ijkl} = 1$ if $i = j = k = l$ and otherwise zero. Also, for this case, $\epsilon_{ij}^{c} = \eta(c - \bar{c})\delta_{ij}$. The coefficients in Eq. (C4) can be written in terms of the elastic constants (in Voigt notation) as

$$\alpha = -\frac{C_{12}}{(C_{11} - C_{12})(C_{11} + 2C_{12})}$$

$$\beta = \frac{1}{4C_{44}} \qquad \text{(B5)}$$

$$\gamma = \frac{\tau}{2(C_{11} - C_{12})C_{44}}$$

where the anisotropy factor $\tau = C11 - C12 - 2C44$ vanishes for an isotropic solid. Upon inserting Eqs. (C3) and (C4) into Eq. (C2) and taking a trace, one finds that

$$\nabla^2\left[\sigma_{kk} + \left(\frac{\eta}{\alpha+\beta+\gamma/2}\right)c\right] + \left(\frac{\gamma}{2\alpha+2\beta+\gamma}\right) \times \left[\frac{\partial^2\sigma_{11}}{\partial x_1^2} + \frac{\partial^2\sigma_{22}}{\partial x_2^2} + \frac{\partial^2\sigma_{33}}{\partial x_3^2}\right] = 0 \qquad \text{(C6)}$$

For an isotropic solid, Eq. (C6) can be simplified to read

$$\nabla^2\left[\sigma_{kk} + \left(\frac{2E\eta}{1-\nu}\right)c\right] = 0 \qquad \text{(C7)}$$

where E and ν are the Young's modulus and Poisson's ratio, respectively.

We first consider the isotropic case. Following Larch´e and Cahn [83], one has that

$$\sigma_{kk} + \left(\frac{2E\eta}{1-\nu}\right) c = SZ + T \qquad \text{(C8)}$$

where S and T are constants. Since the boundary conditions for the thin slab are the same at • $\pm\ell$, $S = 0$, and so $\vec{\nabla}\,\sigma_{kk} = -2E\eta/(1-\nu)\vec{\nabla}c$ and the flux is therefore spatially local[3] [32].

For the case of medium with cubic anisotropy modeled here, the stresses σ_{11} and σ_{22} are independent of x and y as the system is translationally invariant in the xy plane. Moreover, since $\sigma_{31} = \sigma_{32} = 0$=, a solenoidal stress implies that σ_{33} is constant and so Eq. (C6) becomes

$$\nabla^2\left[\sigma_{kk} + \left(\frac{\eta}{\alpha+\beta+\gamma/2}\right) c\right] = 0 \qquad \text{(C9)}$$

Given the discussion above, one again concludes that $\vec{\nabla}\,\sigma_{kk}$ depends only on $\vec{\nabla}c$ and that the flux is spatially local.

[3] We note that Larch´e and Cahn considered the case of a slab in contact with fluid only along one face. For this case, the flux is nonlocal [16].

VITA

Mahyar was born in June 29th 1980, Isfahan, Iran, in a family of four. His parents (Mehdi and Jila) are now both retired. Mehdi used to be a technical interpreter at Isfahan steel mill and Jila finished her career as a high school principle. He also has a sister (Mahsa) who now has her own family.

Mahyar got his B. Sc. in materials engineering in January 2004 from Isfahan University of Technology. Then he moved to Tehran to continue his education in graduate level at Iran University of Science and Technology. He began his professional career (before his Master graduation in 2007), first as a process engineer in steel industry and later as an engineering coordinator. In August 2009 he got married to Shokouh Pourarian and then they moved to US to fulfill their dreams for earning PhD degree. Mahyar pursued his PhD in computational materials science and engineering at Lehigh University and graduated in December 2014. Mahyar's extended CV could be found below:

Mahyar Mohebi-Moghadam

678-882-9207 | mahyar.mm@gmail.com | LinkedIn Profile

Computational Materials Scientist

Self-motivated and research-savvy **computational materials scientist** with 6 years of progressive experience across a broad range of materials and simulation methods. Proven ability to combine mathematical solutions and physical modeling with custom design computer programs to address today's challenges in materials science and engineering. **Area of expertise include:**

- ✓ Molecular Dynamic Simulation
- ✓ Finite Difference Modeling
- ✓ Monte Carlo Simulation
- ✓ Ab-initio Modeling
- ✓ Diffusion & Mass Transfer
- ✓ Thermodynamics & Kinetics
- ✓ Statistical Mechanics
- ✓ Mechanical properties
- ✓ Grain Boundary Properties
- ✓ Microstructure & Phase transition
- ✓ Nano Porous Materials
- ✓ High Temperature Processes

Education

- **Ph. D. in Materials Science & Engineering,** Jan. 2011- Jan. 2015. Lehigh University, Bethlehem, PA, USA.
- **M. Sc. in Materials Science & Engineering,** Sep. 2004-May 2007. University of Science & Technology, Tehran, Iran.
- **B. Sc. in Materials Science & Engineering,** Sep. 1999-Feb. 2004. Isfahan University of Technology, Isfahan, Iran.

Publications

- M. M. Moghadam, J. M. Rickman, H. Chen, M. Harmer, **"The Role of Boundary Variability in Polycrystalline Grain-Boundary Diffusion"**, J. Appl.Phys. submitted.
- M. M. Moghadam, J. M. Rickman, **"Hybrid Atomistic Simulation of Fluid Uptake in a Deformable Solid"**, Phys. Rev. E 89, 012305 (2014).
- M. M. Moghadam, S. S. Seyedein, M. R. Aboutalebi**, "Fluid flow and heat transfer modeling of AC arc in ferrosilicon submerged-arc furnace"**, J. Iron and Steel Research, Int., 17, 14 (2010).

Experience

Academic:

- **Research Assistant:** Computational materials science, Lehigh University, Jan. 2011-Continue.
- **Teacher Assistant:** Modeling & Simulation in Materials Engineering, Fall 2013.
- **Instructor:** Materials science and Engineering Lab, University of Toledo, Fall 2010.

Industry:

- **Barsoo Engineering Co., August 2007- August 2009**
  Process designer and engineering coordinator, Direct reduction & EAF steel making, Tehran, Iran.
- **Isfahan Saman Energy Co., January 2006-March 2007**
  Engineering coordinator, Optimization of energy in steel, aluminum and glass industries, Isfahan, Iran.

Workshop, Conference & Training

- **BerkeleyGW 2014 Workshop;** Ab initio calculations of many-electron effects in excited-state properties of condensed matter. NERSC, Ockland CA, Fall 2014.

- **MS&T14;** "Impact of interface variability on grain boundary diffusion in polycrystalline structures", Oral presentation, Pittsburgh PA, Oct. 2014.

- **HPC 2014;** Workshop in parallel programming and optimization for High-Performance Computing, by Dr. Axel Kohlmeyer, Temple University, Philadelphia PA, Jul. 2014.

- **Online Course in MD, Ab-Initio & DFT;** From Atoms to Materials, Predictive Theory and Simulations by Professor Ale. Strachan, Purdue University, nanoHUBU, Summer 2013.

Awards

- **GSS Travel Grants;** MS&T14 conference, Pittsburgh, USA, 2014.

- **Sherman Fairchild Fellowship;** Sherman Fairchild Center for Solid State Studies, 2013-2014.
- **PC. Rossin Graduate Research Fellowship;** Lehigh University, Materials Science and Engineering graduate scholarships, 2012-2014.

Computer Skills

- Programming language **(Fortran, Python)**
- Parallel programming **(OpenMPI)**
- Programming & Visualization **(Mathematica)**
- Linux shell scripting
- Profiling, debugging and optimization

Memberships

- **TMS -** The Minerals, Metals and Materials Society
- **ASM International -** The Materials Information Society
- **ACerS -** The American Ceramic Society
- **AIST -** Association for Iron & Steel Technology

Hobbies

- Music, Photography, Reading
- Hiking, Fishing, Swimming

References

1. **Jeffrey Rickman, Ph.D.**
   Professor, Department of Materials sci. & Eng.
   Lehigh University, Bethlehem, PA, USA.
   Email: jmr6@lehigh.edu

2. **Martin Harmer, Ph.D.**
   Professor, Department of Materials sci. & Eng.
   Lehigh University, Bethlehem, PA, USA.
   Email: mph2@lehigh.edu

3. **Helen Chen, Ph.D.**
   Professor and Chair, Department of Materials sci. & Eng.
   Lehigh University, Bethlehem, PA, USA.
   Email: hmc0@lehigh.edu

4. **Edmund Webb III, Ph.D.**
   Associate Professor, Department of Mechanical Eng.
   Lehigh University, Bethlehem, PA, USA.
   Email: ebw210@lehigh.edu